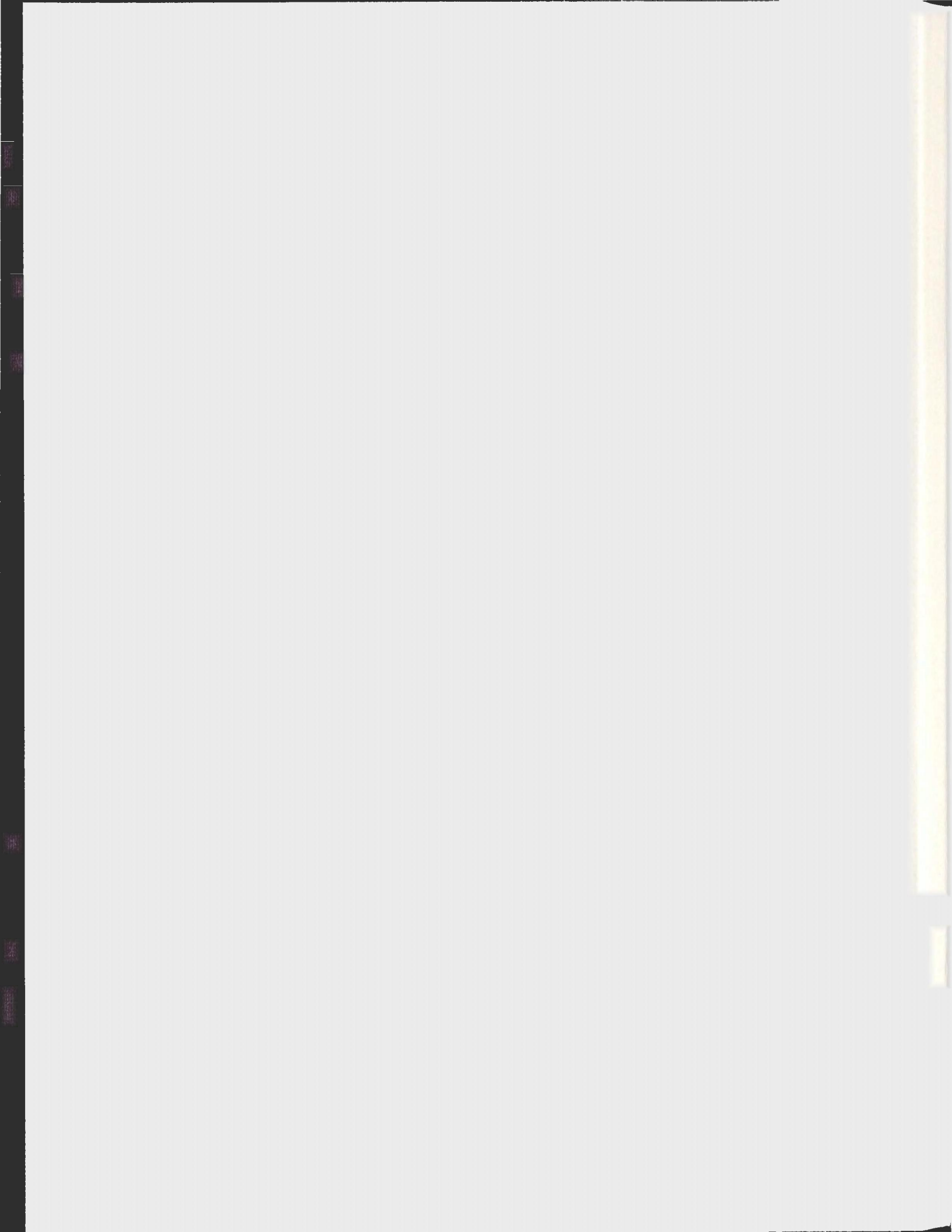


FIBER OPTIC CURRENT SENSOR AND ITS  
WIRELESS SENSING SYSTEM

CHUANTAI SHI







**Fiber Optic Current Sensor and Its Wireless Sensing System**

by

Chuantai Shi

A thesis submitted to the

School of Graduate Studies

in partial fulfillment of the requirements for the degree of

**Master of Science**

Department of Physics and Physical Oceanography

Memorial University of Newfoundland

August 2013

St. John's

Newfoundland

## ABSTRACT

Fiber optic current sensors (FOCSs) based on Faraday magneto-optic effect is able to overcome many shortcomings in traditional measurements of electrical currents, including susceptibility to magnetic saturation, expensive and bulk packages, and low tolerance to hostile environments such as corrosive materials, high temperatures, and high electromagnetic interference. This thesis first investigates the Faraday magneto-optic effect in silica fibers and rare-earth doped fibers, then develops and demonstrates a FOCS operating at telecommunication wavelengths in both basic scheme and reflective scheme. A light beam from a laser source is first launched into a fiber. Next, the light beam in the fiber is polarized to form a polarization state. This polarization state in the fiber is then modified by the electromagnetic field induced by the electrical current when the fiber is coiled around an electrical conductor carrying electrical current. Finally, the modified polarization state causes a variation in the polarization state or intensity of output light, which can be measured by a polarization analyzer or a photodetector. This study first measures the Verdet constants of silica fibers and rare-earth doped fibers at telecommunication wavelengths. An in-depth investigation on the dependence of sensitivity and linearity on experimental parameters has been conducted and concluded in this study. The prototype system achieved low cost and high sensitivity while reducing the dependence on the variations of the birefringence.

A demonstration of wireless sensing system for a FOCS, including sensor node, lower machine controlling unit, multiple data interfaces, and host computer service platform is designed and tested with Zigbee modules. In-situ performance has verified the design, and it demonstrated a good reliability and repeatability in monitoring direct current in real time.

## ACKNOWLEDGEMENTS

I would like to express my gratitude to my supervisor, Dr. Qiying Chen, for giving me this opportunity to study and research at Memorial University of Newfoundland. I acknowledge and thank Dr. Chen for his supervision and encouragement on my course study and research work during my master program. I very appreciate Dr. Chen for his vast knowledge, abundant help, precious suggestions, and assistance in writing. I would like to convey thanks to my current and former group members, Dr. Liqiu Men, Daiying Zhang, Weinan Chen, Dr. Ping Lu, Van Nguyen, and Xiaojian Zhu, for their valuable discussions and helpful suggestions.

I would like to thank my course instructors Dr. Martin Plumer, Dr. John Lewis, and Dr. Siu O'Young for their interesting lectures and patient instructions on my course studies. I also wish to thank Dr. Todd Andrews for the suggestions from annual graduate progress meetings and other members from the Department of Physics and Physical Oceanography for their assistance and support during the past two years. I very appreciate the fellowships from my supervisor, the School of Graduate Studies, and the Department of Physics and Physical Oceanography.

Finally, I would like to thank my father Junru Shi, my mother Xiaoyu Jiang, and my sister Huaqin Shi for their countless support and love.

## Table of Contents

<b>ABSTRACT</b> .....	<b>ii</b>
<b>ACKNOWLEDGEMENTS</b> .....	<b>iii</b>
<b>Table of Contents</b> .....	<b>iv</b>
<b>List of Tables</b> .....	<b>vi</b>
<b>List of Figures</b> .....	<b>vii</b>
<b>List of Abbreviations</b> .....	<b>x</b>
<b>Chapter 1 Introduction</b> .....	<b>1</b>
1.1 An overview of electrical current measurement .....	1
1.2 Fiber optic current sensor.....	9
1.3 A survey of wireless data communication .....	13
1.4 Thesis overview .....	17
<b>Chapter 2 Faraday Magneto-optic Effect in Fibers</b> .....	<b>26</b>
2.1 Fundamentals of Faraday magneto-optic effect in an optical fiber .....	26
2.1.1 Polarization .....	27
2.1.2 The Jones calculus .....	29
2.1.3 Poincare sphere and Stokes parameters .....	32
2.2 Faraday magneto-optic effect in various types of fibers.....	34
2.2.1 Faraday magneto-optic effect .....	34
2.2.2 Verdet constant .....	36
2.2.3 Faraday magneto-optic effect in different fibers .....	39
<b>Chapter 3 Basic Scheme of Fiber Optic Current Sensor</b> .....	<b>45</b>
3.1 Experimental setup of basic scheme .....	45
3.2 Effect of birefringence .....	45
3.2.1 Origins of birefringence .....	45
3.2.2 Effects of birefringence on evolution of the propagating polarization .....	48
3.3 Dependence of sensitivity on parameters: simulation perspective .....	51
3.3.1 Dependence on intrinsic birefringence and the initial orientation of intrinsic birefringence .....	53
3.3.2 Dependence on bend-induced birefringence.....	59
3.3.3 Dependence on twist-induced birefringence.....	61
3.3.4 Dependence on initial input state of polarization .....	64
3.4 Dependence of sensitivity on parameters: experimental perspective .....	70
3.4.1 Dependence on bend-induced birefringence.....	71
3.4.2 Dependence on twist-induced birefringence.....	72
3.4.3 Dependence on initial input state of polarization .....	74
3.5 Basic experimental setup with intensity measurement .....	76
3.5.1 Experimental setup.....	76
3.5.2 Dependence of sensitivity on parameters: simulation perspective .....	77
3.5.3 Dependence of sensitivity on parameters: experimental perspective .....	83
3.6 Summary .....	87

<b>Chapter 4 Reflective Scheme of Fiber Optic Current Sensor.....</b>	<b>89</b>
4.1 Experimental setup of the reflective scheme .....	89
4.2 Dependence of sensitivity on parameters: simulation perspective .....	94
4.2.1 Dependence on deviated amount of retarder .....	94
4.2.2 Dependence on deviated amount of connecting azimuth.....	96
4.3 Dependence of sensitivity on parameters: experimental perspective .....	98
4.3.1 Dependence on deviated amount of retarder .....	98
4.3.2 Dependence on deviated amount of connecting azimuth.....	100
4.4 Dependence of light intensity stability on the length of PM fiber .....	102
4.5 Summary .....	104
<b>Chapter 5 Wireless Sensing System for Fiber Optic Current Sensors .....</b>	<b>105</b>
5.1 Realization of wireless communications in fiber-optic sensing systems.....	105
5.2 Design of hardware .....	108
5.3 Design of software .....	112
5.4 Performance of a wireless FOCS sensing system.....	117
<b>Chapter 6 Conclusions.....</b>	<b>119</b>
6.1 Conclusions.....	119
6.2 Future work.....	120
<b>References .....</b>	<b>123</b>
<b>Appendix A Service program of host computer.....</b>	<b>134</b>
<b>Appendix B Controlling program of low machine unit machine .....</b>	<b>153</b>

## List of Tables

Table 1-1 Sensing systems for fiber optic sensors.....	14
Table 1-2 A comparison of various WPAN.....	17
Table 2-1 List of Jones vectors describing SOP .....	30
Table 2-2 Predictions of Verdet constants of various materials at 1550 nm .....	39
Table 2-3 Record and calculation of the orientations of output SOP with systematic error in single-mode fiber (SMF-28e).....	41
Table 2-4 The experimental comparison of the Verdet constants of various sensing fibers .....	42

## List of Figures

Figure 1-1 An Illustration of a shunt resistance-based current sensor .....	2
Figure 1-2 An illustration diagram of Rogowski coil-based current sensor .....	4
Figure 1-3 An illustration diagram of Hall element-based current sensor.....	5
Figure 1-4 Principle of FOCS: (a) principle of Faraday magneto-optic effect; (b) principle of Ampere circuital theorem; (c) an actual FOCS .....	8
Figure 1-5 Architecture of a fiber optic current sensing system with wireless data communication.....	18
Figure 1-6 Basic scheme of a FOCS.....	18
Figure 1-7 Architecture of a wireless fiber optic current sensing system.....	23
Figure 2-1 Poincare sphere and Stokes parameters .....	32
Figure 2-2 Principle of Faraday effect .....	35
Figure 2-3 Relationships between Verdet constant and wavelength for Ce, Pr, Tb, and Dy ion doped phosphate crystals .....	38
Figure 2-4 Recorded Stokes parameters and Faraday rotation .....	40
Figure 2-5 Relationship between the orientation of output SOP and current $i$ with systematic error in a single-mode fiber (SMF-28e).....	40
Figure 2-6 Transmitted spectrum of Er-doped fiber (F-EDF-5).....	43
Figure 3-1 The basic scheme of a FOCS .....	45
Figure 3-2 Nine types of birefringence mechanisms: (a) noncircular core; (b) internal lateral stress; (c) external lateral stress; (d) external lateral stress; (e) free bending; (f) tension bending; (g) tension & ring bending; (h) electrooptic effect; (i) twist.....	46
Figure 3-3 Definition of birefringence in fibers: (a) a bending fiber for sensing; (b) intrinsic birefringence in fiber; (c) birefringence on Poincare sphere. ....	48
Figure 3-4 Illustration of vector rotation .....	50
Figure 3-5 Ideal relationship between $\phi_{out}$ and electrical current $i$ at $\theta = 0$ , $\phi_{in} = 0$ , $\phi_i = 0$ , $\beta_i$ $= 0$ , $\beta_b = 0$ , $\beta_T = 0$ .....	52
Figure 3-6 Relationship between $\phi_{out}$ and electrical current $i$ at $\beta_b = 0$ , $\beta_T = 0$ , $\phi_i = 0$ , $\theta = 0$ , $\phi_{in} = 0$ .....	54
Figure 3-7 Relationship between $\phi_{out}$ and electrical current $i$ at $\beta_b = -2.26$ , $\beta_T = 0$ , $\phi_i = 0$ , $\theta$ $= 0$ , $\phi_{in} = 0$ .....	55
Figure 3-8 Relationship between $\phi_{out}$ and electrical current $i$ at $\beta_i = 0.0168$ , $\beta_b = 0$ , $\beta_T = 0$ , $\theta = 0$ , $\phi_{in} = 0$ .....	57
Figure 3-9 Relationship between $\phi_{out}$ and electrical current $i$ at $\beta_i = 0.0168$ , $\beta_b = -2.26$ , $\beta_T$ $= 0$ , $\theta = 0$ , $\phi_{in} = 0$ .....	58
Figure 3-10 Bending of the sensing fiber in the experimental setup .....	59
Figure 3-11 Relationship between $\phi_{out}$ and electrical current $i$ at $\beta_i = 0.0168$ , $\beta_T = 0$ , $\phi_i =$ $0$ , $\theta = 0$ , $\phi_{in} = 0$ .....	60
Figure 3-12 Relationship between $\phi_{out}$ and electrical current $i$ at $\beta_i = 0.0168$ , $\beta_b = -2.26$ , $\phi_i$ $= 0$ , $\theta = 0$ , $\phi_{in} = 0$ .....	62
Figure 3-13 Relationship between $\phi_{out}$ and electrical current $i$ at a large current range with $\beta_i = 0.0168$ , $\beta_b = -2.26$ , $\phi_i = 0$ , $\theta = 0$ , $\phi_{in} = 0$ .....	63

Figure 3-14 Relationship between $\phi_{out}$ and electrical current $i$ at different linear input SOPs at $\beta_l = 0.0168$ , $\beta_b = -2.26$ , $\beta_T = 9.17$ , $\phi_i = 0$ , $\phi_{in} = 0$ .....	65
Figure 3-15 Relationship between $\phi_{out}$ and electrical current $i$ at different elliptical input SOPs at $\beta_l = 0.0168$ , $\beta_b = -2.26$ , $\beta_T = 18.35$ , $\phi_i = 0$ , $\theta = 45$ .....	66
Figure 3-16 Relationship between $\phi_{out}$ and electrical current $i$ at circular input SOP at $\beta_l = 0.0168$ , $\beta_b = -2.26$ , $\beta_T = 18.35$ , $\phi_i = 0$ , $\phi_{in} = 90$ .....	67
Figure 3-17 Relationship between $\phi_{out}$ and electrical current $i$ at large current range with $\beta_l = 0.0168$ , $\beta_b = -2.26$ , $\beta_T = 18.35$ , $\phi_i = 0$ , $\theta = 45$ .....	69
Figure 3-18 Evidence of existing birefringence: (a) output elliptical polarization; (b) Faraday rotation orbit is out of equatorial plane .....	70
Figure 3-19 Dependence of sensitivity on bend-induced birefringence .....	72
Figure 3-20 Dependence of sensitivity on twist-induced birefringence at $\beta_l = 0.0168$ , $\beta_b = -2.26$ , $\theta = 45$ , $\phi_i = 0$ , $\phi_{in} = 0$ .....	73
Figure 3-21 Recorded zero drift in FOCS at $\beta_T = 36.69$ rad.....	73
Figure 3-22 Dependence of sensitivity on initial input SOP at $\beta_l = 0.0168$ , $\beta_b = -2.26$ , $\beta_T = 9.17$ , $\phi_i = 0$ .....	75
Figure 3-23 A pre-polarizer is deployed to obtain an ideal initial linear input SOP .....	76
Figure 3-24 Basic scheme of FOCS with intensity measurement .....	77
Figure 3-25 Relationship between $I_{out}$ and current $i$ at various intrinsic birefringence. ....	78
Figure 3-26 Relationship between $I_{out}$ and current $i$ at various bend-induced birefringence. ....	79
Figure 3-27 Relationship between $I_{out}$ and current $i$ at various twist-induced birefringence. ....	80
Figure 3-28 Relationship between $I_{out}$ and current $i$ at various orientations of initial linear input SOP. ....	81
Figure 3-29 Relationship between $I_{out}$ and current $i$ at various orientations of detecting polarizer. ....	82
Figure 3-30 Experimental setup established to detect the output light intensity .....	84
Figure 3-31 Relationship between $\cos^2 x$ and $x$ .....	84
Figure 3-32 Linear output SOP after sensing fiber at $\pi/4$ with $x$ -axis. ....	85
Figure 3-33 Experimental result: relationship between normalized intensity and bend-induced birefringence.....	86
Figure 3-34 Experimental result: relationship between normalized intensity and twist-induced birefringence.....	87
Figure 4-1 Experimental setup of FOCS with a reflective scheme.....	90
Figure 4-2 Ideal relationship between detected phase delay and current in the reflective scheme.....	94
Figure 4-3 Dependence of sensitivity on the deviated amounts of retarder.....	95
Figure 4-4 Cross section of connecting fiber cores between PM fiber and retarder (SS and FF indicates slow axis and fast axis respectively) .....	96
Figure 4-5 Dependence of sensitivity on the connecting azimuths .....	97
Figure 4-6 Length of the PM fiber (PM-15U40A, retarder).....	98
Figure 4-7 Experimental result: dependence of sensitivity on deviation of retarder at perfect connecting azimuth with 90 m PM fiber .....	99

Figure 4-8 Determination of the birefringent axes of PM fiber (PM-15U40A) .....	100
Figure 4-9 The alignment of PM fiber: (a) 45° alignment between the linearly polarized SOP and the PM fiber; (b) 0° alignment between the linearly polarized SOP and the PM fiber. ....	100
Figure 4-10 Experimental result: dependence of sensitivity on deviation of retarder at -4° deviation of retarder with 90 m PM fiber .....	101
Figure 4-11 Experimental result: Dependence of stability of interfered light intensity on length of PM .....	103
Figure 5-1(a) Architecture of wireless network with two Zigbee Xbee series 2 modules; (b) one Zigbee Xbee series 2 module with USB power supply and data communication.....	106
Figure 5-2 Building process of a wireless network with X-CTU software .....	106
Figure 5-3 Successful communication between the coordinator and the router .....	108
Figure 5-4 Architecture of wireless sensing system for FOCS: (a) principle of the FOCS wireless sensing system; (b) experimental layout of the FOCS wireless sensing system .....	109
Figure 5-5 Hardware design of lower machine controlling unit based on Altium Designer 10: (a) schematic design of electronic circuitry; (b) design of printed circuit board; (c) a complete printed circuit board with electronic components.....	110
Figure 5-6 Hardware assembly of a power meter (under the circuit board), lower machine controlling unit, and Zigbee module .....	111
Figure 5-7 Design of host computer service platform on Microsoft Visual Basic 6.0: (a) main interface; (b) setting parameters interface.....	112
Figure 5-8 Program flow chart of host computer service platform.....	114
Figure 5-9 Compiled controlling program was downloaded into the microprocessor: (a) program writing environment; (b) downloading program through ISP communication.....	115
Figure 5-10 Program flow chart of lower machine controlling unit .....	116
Figure 5-11 In-situ test of a wireless FOCS sensing system: (a) sensing curve of basic scheme; (b) an application in remote monitoring of electrical current .....	117
Figure 6-1 Wireless fiber-optic current sensor network .....	121

## List of Abbreviations

AC	Alternating current
DC	Direct current
FOCS	Fiber optic current sensor
NIR	Near infrared
CT	Current transducer
YIG	Yttrium Iron Garnet
FOS	Fiber optic sensor
SNR	Signal to noise ratio
WMAN	Wireless Metropolitan Area Network
WLAN	Wireless Local Area Network
WPAN	Wireless Personal Area Network
GSM	Global System for Mobile
FDMA	Frequency-Division Multiple Access
TDMA	Time-Division Multiple Access
GPRS	General Packet Radio System
EDGE	Enhanced Data Rates for GSM Evolution
IEEE	Institute of Electrical and Electronics Engineers
PM	Polarization maintaining
ADC	Analog to Digital Converter
PC	Personal computer
PAN	Personal Area Network
SOP	State of polarization
USART	Universal Synchronous/Asynchronous Receiver/Transmitter
USB	Universal Serial Bus
ISP	In-System Programming
WSN	Wireless Sensor Network

# Chapter 1 Introduction

## 1.1 An overview of electrical current measurement

Measurement of electrical currents plays a significant role in modern power systems and electro-chemical industries. Incorrect measurements may cause very serious accidents. For instance, too low assessments of output currents in nuclear power stations may cause nuclear disasters; inaccurate monitoring of operating currents in electro-chemical industries will probably damage the quality of industrial products. The underlying fundamental physical principles to measure electrical currents in research and industry are generally classified as Ohm's law of resistance, Faraday's law of induction, Hall effect, and Faraday magneto-optic effect [1, 2].

Based on Ohm's law of resistance, shown in Eqn. (1-1) [2], shunt resistance is a common approach to measure electrical currents due to its simplicity. According to Ohm's law of resistance, the voltage drop across the shunt resistor is proportional to flowing current in a conductor, which is usually employed to sense currents [3-5]. Figure 1-1 shows a illustrating diagram of a shunt resistance in which  $L_s$  is the shunt resistance used to measure electrical current.

$$\vec{J} = \sigma \vec{E} \quad (1-1)$$

where  $\vec{J}$  is the current density,  $\sigma$  is the material conductivity, and  $\vec{E}$  is the electrical field.

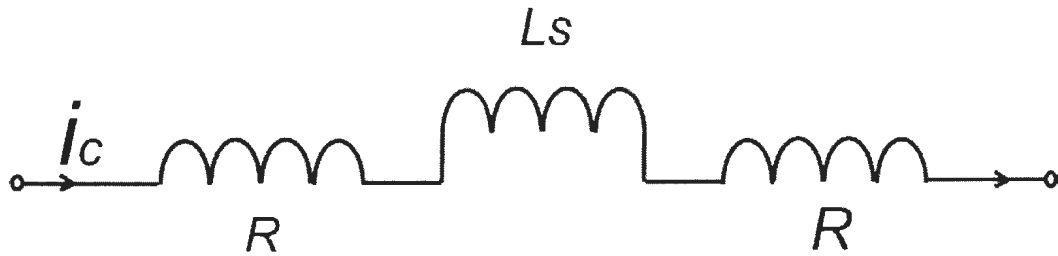


Figure 1-1 An Illustration of a shunt resistance-based current sensor

Shunt resistance can be used to sense both alternating currents (AC) and direct current (DC). These current sensors have been extensively used in power electronics due to their low cost, small size, and relative simplicity, while providing reasonable accuracy [5-7]. However, since shunt resistor is introduced into current conducting path for sensing, it generates a substantial amount of power loss which can be calculated from Ohm's law and increases with the square of the current. This power loss may restrict the use of shunt resistors in high current measurements [8]. Another important issue of using shunt resistor is the parasitic inductance and the series resistance caused by sensing loops and skin effect, which greatly limits the bandwidth and magnitude of measuring AC [2]. Also, shunt resistor induced thermal effect not only affects the measurement accuracy but also has potential risks to give rise to fire in large current measurements. A Rogowski coil based on Faraday's law of induction is a classical example of current sensors in measuring isolated electrical current which provides inherent electrical isolation between the current to be measured and the output signal. The working principle of the Rogowski coil can be explained starting with Ampere's circuital theorem, shown in Eqn. (1-2) [2].

$$\oint_C \vec{B} \cdot d\vec{l} = \mu_0 i_c \quad (1-2)$$

where,

$i_C$  is the current flowing through the area enclosed by curve  $C$ ;

$\mu_0$  is the permeability of free space;

$B$  is the magnetic flux density given by measuring electrical current from Eqn. (1-3) [2];

$$B = \frac{\mu_0 i_C}{2\pi r} \quad (1-3)$$

where,

$r$  is the radius of the Rogowski coil.

Thus, by applying Faraday's law of induction, an induced voltage  $v$  which is proportional to the derivative of the primary measuring current  $i_C$  is derived in Eqn. (1-4) [2].

$$v = -N_r \frac{d\phi}{dt} = -NA \frac{dB}{dt} = -\frac{N_r A \mu_0}{2\pi r} \frac{di_C}{dt} \quad (1-4)$$

where,

$N_r$  is the number of turns of the Rogowski coil;

$A$  is the cross-sectional area of the coil.

Therefore, utilizing an integrator with integrating constant  $k$  (typical several  $\mu s$ ) to integrate induced voltage, Eqn. (1-4) evolves into Eqn. (1-5) with an initial DC bias  $v_0(0)$  [9]. An illustration diagram of the Rogowski coil is shown in Figure 1-2.

$$v_{out} = -\frac{N_r A \mu_0}{2\pi r} k \int_i \frac{di_c}{dt} + v_0(0) = -\frac{N_r A \mu_0}{2\pi r} k i_c + v_0(0) \quad (1-5)$$

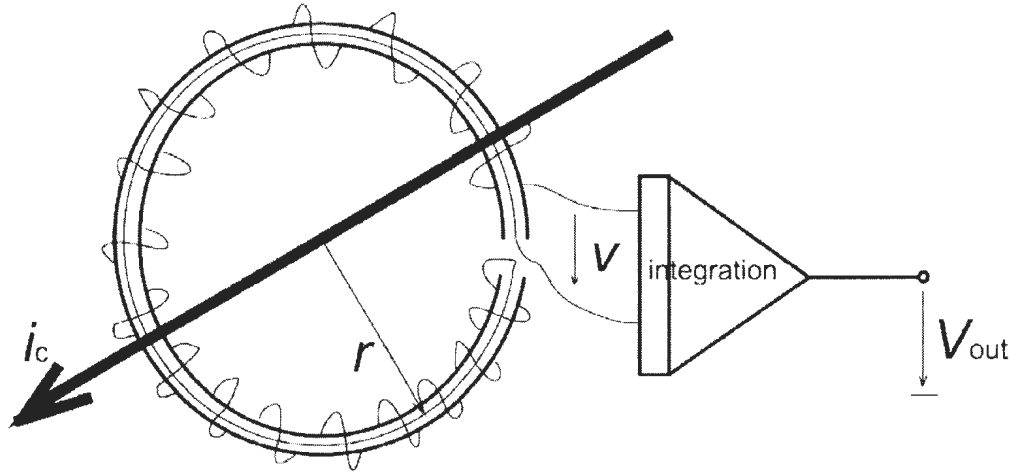


Figure 1-2 An illustration diagram of Rogowski coil-based current sensor

The Rogowski coil is widely employed to measure AC in power distribution systems, short-circuit testing systems, electromagnetic launchers, slip-ring induction motors, and lightning test facilities [10, 11]. The distinct feature of a Rogowski coil is that it does not saturate and shows good linearity in sensing isolated measuring currents. However, the Rogowski coil is not suitable for use in measuring low frequency AC because the response of the integration constant  $k$  of a practical integrator is reduced at low frequency [9-11]. In addition, the measurement errors will increase when the Rogowski coil is not centered or the winding coil is not perfectly symmetry [9]. Finally, the sensitivity of a Rogowski coil is small as the magnetic flux density induced by measuring current is small.

Another important current transducer commonly used in industries is based on Hall Effect [1, 12, 13]. A Hall element has a magnetic core encircling electrical busbars, which are usually placed in workplaces to carry large current. A number of Hall elements are embedded in gaps along the core and detect the magnetic flux intensity induced by electrical currents to be measured, shown in Figure 1-3. In the high performance designs, the signals of the Hall elements are fed to high gain current amplifiers [14-17]. These amplified currents pass through solenoids around the core and generate a magnetic field compensating the field of the original current. The sum of the solenoid currents is proportional to the primary current. However, such Hall effect-based transducers are facing increasing challenges in both instrumental designs and industrial applications today.

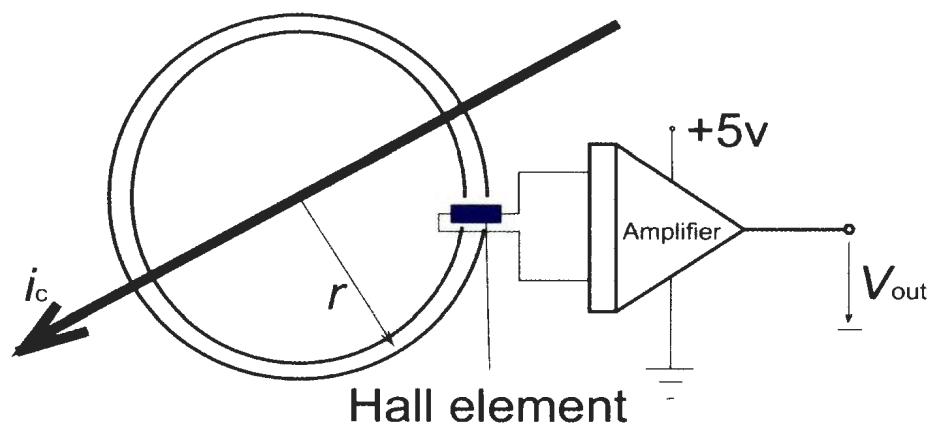


Figure 1-3 An illustration diagram of Hall element-based current sensor

Though Hall effect-based transducers have achieved accurate and reliable measurements, they are rather complex systems, which demand intricate installation and commissioning procedures as well as many other disadvantages [13]. First of all, their

gain materials are easily saturated and the response to high frequency signals is poor, they are unable to respond to transient signals on the line, which greatly limits the measuring range of large current [13]. Secondly, insulation structure is complex, large size, and high cost, which result in inconvenient equipment installation and maintenance [13]. Thirdly, they pose a potential threat to equipment and personal safety, if the secondary load-open circuit produces a high voltage [13, 16]. Also, there is a risk of explosion for oil-bearing transformers [13, 17]. In addition, with the extensive applications of digital technology in the power system, a coupled current transformer is required for the interface between a traditional transformer and a digital device. Besides, special care must be taken to avoid erroneous output due to asymmetric field distributions and to disturbances from neighboring currents or busbar corners [13, 15]. Care must also be taken into consideration in order to minimize potential errors due to asymmetric magnetic fields or cross talk from neighboring currents [13, 17]. As a result, the complexity of these transducers means that time consuming and rigorous installation and commissioning is required.

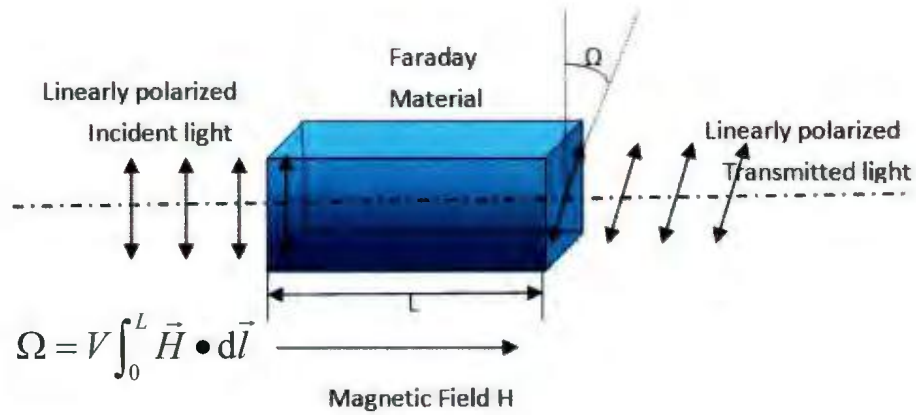
The Faraday magneto-optic effect, also called Faraday effect, combined with Ampere's circuital theorem has been frequently used as an optical method to measure electrical current since 1980s [1]. Shown in Figure 1-4 (a), when polarized light propagates through an optically active material in a direction parallel to the applied magnetic field, such as a piece of glass, its plane of polarization is rotated and this rotation angle is proportional to the intensity of the applied magnetic field, while the intensity of applied field is also proportional to the amount of measuring electrical current

flowing in a wire, show in Figure 1-4 (b). These two relationships are suitable to be deployed to design and integrate a fiber optic current sensor (FOCS) for current measurements, shown in Eqn. (1-6) [1, 13].

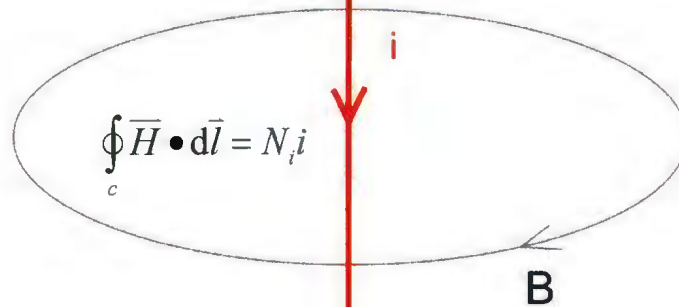
$$\Omega = VN_i N_f i \quad (1-6)$$

where  $V$  is the Verdet constant of a Faraday material (typically  $-4.8$  rad/A for a SMF-28e fiber at  $632$  nm),  $N_i$  is the number of turns of wires carrying measuring current through a sensing fiber coil,  $N_f$  is the number of turns of a sensing fiber coil, and  $i$  is the electrical current to be measured.

Compared with traditional current sensors, the FOCS is advantageous to measure both large AC and large DC with its unique merits: perfect isolation with low cost, producing nonreciprocal circular birefringence, excellent sensitivity and dynamic range, compact and rugged packages, and high tolerance with hostile environments such as high temperatures, corrosive materials, and high electromagnetic interference [1, 18, 19]. The main difficulty for bringing a FOCS into practical application is its integration, because the optical birefringence existing in sensing fibers during FOCS integration will degrade its sensitivity and linearity.



(a)



(b)



(c)

Figure 1-4 Principle of FOCS: (a) principle of Faraday magneto-optic effect; (b) principle of Ampere circuital theorem; (c) an actual FOCS

## 1.2 Fiber optic current sensor

As early as 1973, the British researcher Rogers proposed the idea of measuring current with optical techniques [20]. Since then, much research work has been carried out in this field at visible or near infrared (NIR) wavelengths to measure AC. The optical current sensing techniques reported so far may be classified into four categories [18, 19], which are: (a) all-fiber optical current sensors; (b) bulk-glass optical currents sensors; (c) hybrid current sensors; (d) magnetic field sensors used as current sensors. Almost all of these are based on the Faraday effect except the hybrid sensors which based on traditional current transducers.

For all-fiber optical current sensors, the most promising advantages are their easy integration, wide sensing range, and perfect isolation with low cost. A commercially available 500 kA DC FOCS has been described in Ref. [21]. Few field-test results have been reported to try to solve the problem of linear birefringence inside optical fibers affecting the performance of sensing systems [18, 19]. Although research into all fiber-optic current sensing techniques has been conducted since the 1980s and more than ten methods have been reported to overcome the problems induced by birefringence, none of them can solve the problem satisfactorily, and in fact some of the proposed methods will introduce new problems while attempting to eliminate the problems associated with the birefringence [18, 19].

The bulk glass current sensing technique is a promising choice with less influence from optical birefringence, because they use bulk glass as sensing elements which do not

suffer from the problems associated with the presence of the intrinsic and bend-induced birefringence [18, 19, 20]. Optical glasses with higher Verdet constant could be used as the sensing elements to achieve higher sensitivities. However, the bulk glass current sensor is greatly suffered from the problem of reflection-induced phase difference, in which a phase difference exists between the two orthogonal components of linear polarization when a beam of linearly polarized light is reflected at an incident angle that is larger than the critical angle [20]. Also, the values of Verdet constant in such materials greatly depend on the environmental temperature [22].

For the hybrid current sensors which introduce a conventional electrical or electronic current sensor as the first sensing element [18, 19], the shortcomings of conventional current transducers (CTs) cannot be avoided. For the magnetic-field sensors, the noisy magnetic fields induced by stray currents easily affect the current sensors, causing practical problems preventing the magnetic-field sensors from achieving reliable sensitivity with high accuracy.

Besides the bulk glass sensing elements, some researchers also paid attention to other current sensing systems using other bulk optical materials, such as Yttrium Iron Garnet (YIG) or various types of doped YIG, as the sensing materials. The field test results showed higher sensitivities than the systems employing bulk glass as sensing elements. Compared with the all-fiber optical current sensing systems, the effect of linear birefringence is largely decreased by these two kinds of current sensors utilizing bulk optical materials including bulk glasses [18, 19, 22].

The majority of research efforts made so far have been mainly focused on how to reduce the effects of linear birefringence inside optical fibers in sensing systems. Linear birefringence inside optical fibers can be categorized into two groups: intrinsic linear birefringence which is derived from the asymmetry of the intersections of cores and the strain inside the fibers; extrinsic linear birefringence which is induced by bending or pressing of the fibers. The existence of linear birefringence inside fibers reduces the system sensitivity and causes the system to be more sensitive to surrounding temperature and mechanical vibration. To resolve this problem, much work has been conducted and eight schemes have been proposed, which may be briefly reviewed as follows:

- (1) suppression of the linear birefringence by using a fiber with a large circular birefringence, using either twisted fiber [23] or spun fiber [24];
- (2) removal of the linear birefringence by annealing the sensing fiber [25];
- (3) separation of the Faraday rotation from the linear birefringence by using time multiplexing of two different states of polarization of the input light [26];
- (4) separation of the Faraday rotation from the linear birefringence geometrically by winding a square architecture of sensing element [27];
- (5) complete analysis of the polarization state of the output light by using a polarimeter [28];
- (6) adoption of mode coupling detection by using a highly birefringent fiber [29];
- (7) use of an interferometric detection scheme [30, 31];
- (8) reduction of the effects of the linear birefringence in fiber leads by using an orthoconjugated reflector [32].

These schemes are aimed to reduce the effects of linear birefringence on sensing systems to a certain extent, and provide some possible approaches for the development of all-fiber optic current sensors. However, it was found that some of the schemes mentioned above cannot solve the problem of linear birefringence thoroughly, and some of the proposed approaches even introduce some new problems to the system. As a result, there is still a long way to go to bring all-fiber-optic current sensors to practical applications.

In the 1980s, all-fiber optical current sensors were one of the major research directions in optical current sensing techniques. These research activities were focused on possible solutions to eliminate the effect of linear birefringence inside fibers of the sensing systems. In the 1990s, most of the earlier work was aimed at suppressing, reducing or eliminating the linear birefringence. However, a majority of the later work turned to exploit the difference between the Faraday effect and the effect of linear birefringence which is non-reciprocal (the same direction) and circular birefringence which is reciprocal (the opposite direction) in order to eliminate the effect of birefringence in the systems. Besides these efforts, research into the Faraday effect current sensing system employing low-birefringent fiber made of glass with a low photo-elastic constant was also reported [33]. Ma *et al.* also proposed a novel method of assembling a magneto-optic current transducer, which can eliminate both thermal transient and integration-caused birefringence to a large extent [34]. In 2010, Sun *et al.* reported a new method that used a section of 56-wt%-Terbium-doped silicate fiber [35]. In 2012, El-Khozondar *et al.* conducted a study on the effect of the inhomogeneity of the

magnetic field induced by the current on the sensitivity of the optical sensor [36].

More than twenty patents on fiber optic current sensors for measuring alternating current at visible or near infrared wavelengths, particularly on all-fiber current sensors, have been granted since 1980s. For the bulk-glass current sensor elements, Sato *et al.* applied for three patents in Japan in 1982 and for a European patent in 1983 [37]. Since then, American and Japanese researchers have done much work on bulk-glass current sensors and published some reports about research and the field-test results [38]. In 1990s, Jackson and co-workers performed an in-depth investigation on this area, and proposed triangular-type [39], openable-type [40] and ring-type [41] designs of bulk-glass current-sensing elements.

### **1.3 A survey of wireless data communication**

Fiber optic sensors (FOSs) represent a crucial improvement over the traditional sensors in a wide range of application areas, such as environmental, safety and industrial monitoring. When it comes to the integrations of FOS systems, most of the traditional integrating systems chose optical fibers and other optical devices as a result of their dual functionality, sensing and transmission. In the last decade, many researchers have conducted much research on the integration of various types of sensing systems for FOSs, summarized in Table 1-1. However, these integrated systems are facing many fundamental challenges in extending the sensing length, increasing the number of multiplexed sensors, decreasing the signal to noise ratio (SNR), and reducing the integrating cost [42].

Table 1-1 Sensing systems for fiber optic sensors

Year	Network Topology	Amplification Type	Network Length	Multiplexed Sensors	SNR	Ref.
2012	Bus	Raman+EDFA	150 km	3	1 dB	[43]
2012	Ring/Star	EDFA	50 km	2	25 dB	[44]
2011	Bus	Raman	75 km	2	17 dB	[45]
2011	Bus	No amplification	253 km	1	3 dB	[46]
2011	Bus	Raman	250 km	4	18 dB	[47]
2011	Bus	Raman	200 km	4	22 dB	[47]
2011	Bus	Raman+EDFA+Brillouin	155 km	2	10 dB	[48]
2011	Bus	Raman+Brillouin	100 km	4	30 dB	[49]
2010	Bus	Raman+EDFA	100 km	1	30 dB	[50]
2010	Bus/Star	Raman	50 km	4	46 dB	[51,52]
2009	Bus	Raman	50 km	2	50 dB	[53]
2009	Ring/Star	EDFA	50 km	4	58 dB	[54]
2008	Bus	EDFA	230 km	1	4 dB	[55]
2008	Bus	EDFA+SOA	20 km	3	25 dB	[56]
2007	Bus	No amplification	120 km	1	24 dB	[57]
2006	Bus/Star	Raman+EDFA	50 km	2	60 dB	[58]
2006	Bus	Raman	16.5 km	4	16 dB	[59]
2005	Bus	EDWA+SOA	25 km	3	50 dB	[60]
2005	Bus	Raman	50 km	2	50 dB	[61]
2005	Bus	Raman	50 km	1	50 dB	[62]
2005	Bus	Raman	35 km	8	27 dB	[63]
2005	Bus	Raman	22 km	4	15 dB	[64]
2004	Bus	Raman+EDFA	50 km	1	11 dB	[65]
2004	Bus	Raman	25 km	2	50 dB	[66]
2003	Bus	Raman	50 km	1	15 dB	[67]

Wireless data communication, also regarded as mobile data, provides an alternative approach to integrate sensing systems for FOSs. Firstly, sensor node based on wireless data communication is portable with small size, and it is easy for installation and use. Then, sensing systems deploying the wireless data communication techniques may provide considerable reduction in integration cost and a degree of flexibility not known in

fiber systems, which enables the capability of multiplexing more sensor nodes. Also, the wireless data communication also has advantages of low power consumption with reliable life time. Finally, acquired data with wireless communication is easy to interface with information systems and convenient for further processing. In terms of its coverage area, wireless data communication technique is usually classified as cellular telephony system, Wireless Metropolitan Area Networks (WMAN), Wireless Local Area Networks (WLAN), Wireless Personnel Area Networks (WPAN) [68]. Selecting the right wireless solution for a given sensing system, many complex factors need to be considered, including multiplexing capabilities, communication channel, noise level, security, installing and running cost, power consumption, licensed versus unlicensed operation channel, compatibility with hazardous environments, fault-tolerance, commercial availability, and quality of service [68].

The first commercial cellular telephony system was brought into use in 1983, though users often lost their calls [51]. At the same time, Global System for Mobile (GSM) communications which used Frequency-Division Multiple Access (FDMA) and Time-Division Multiple Access (TDMA) was firstly proposed and tested [69, 70]. However, GSM system was not adequate for data transmission because the communication channel was assigned to one single user even if there is no data to send. As an improvement, General Packet Radio System (GPRS), which was a packet switched system, allowed data transmission rates to reach 170 Kbs [68]. The new Enhanced Data Rates for GSM Evolution (EDGE) system recently improved the data capacity to 384 Kbs [68].

WMAN mainly indicates the broadband wireless access based on the IEEE (Institute of Electrical and Electronics Engineers) standard 802.16. WMAN operates at the communication channel from 1.5 MHz to 20 MHz with communication distance up to 50 m and data rate up to 70 Mbps [71]. Hundreds of simultaneous sections per channel are allowed in WMAN while each delivers can have a communication speed more than 1 Mbps. WMAN is designed mainly for voice, video, continuous and burst traffic while supporting point to multipoint and mesh network [72].

The most widely used specification for WLANs is based on the standard IEEE 802.11, including 802.11 a, 802.11 b, 802.11 g, and 802.11 n, which specifies physical and medium access layers by using spread spectrum techniques. IEEE 802.11 is also known as WiFi (Wireless Fidelity), which is compatible between wireless equipment from different manufacturers, and HIPERLAN (High Performance Radio LAN), a European standard [73]. IEEE 802.11 is a free license channel working at 2.4 GHz and 5.2 GHz with communication distance up to 150 m at data rate up to 54Mbps [74]. WMAN supports real time data traffic and intelligent power management which allows a sensor node to have a long life time [74, 75].

WPAN, which mainly based on IEEE 802.15, is intended for short range communication from 10 m to 1 km and has a very wide range of applications including personnel computing, health care as well as industrial and home automation with low installation cost and low power consumption. The typical products in WPAN are Zigbee, Bluetooth, IrDA (Infrared Data Association), and wireless USB (Universal Serial Bus) which operates in free license communication channel 2.4 GHz with data rate 1 Gbps [76,

77]. Zigbee has communication distance from 10 m to 1 km with very low power consumption, and is easy to form bus/ring/cluster/mesh wireless sensor network, which makes Zigbee very suitable for applications in wireless sensing systems at short range communication. Bluetooth communication distance is from 10 m to 100 m with data rate up to 16 Mbps, which limits its coverage range and the number of multiplexing sensor node in industrial applications [68]. IrDA modules work in a range less than one meter with data rate from 9.6 Kpbs to 4 Mbps. Applications of IrDA are limited as a result of its short communication range and special requirement in line of sight and narrow angle [76]. Wireless USB usually works in the bandwidth of 480 Mbps at 3 m communication range and 110 Mbps at 10 m communication range, which only allows for short range communication. A comparison of various WPAN is listed in Table 1-2.

Table 1-2 A comparison of various WPAN

<b>Characteristic</b>	<b>Data rate</b>	<b>Maximum range (m)</b>	<b>Spectrum (GHz)</b>	<b>Power</b>	<b>Security</b>
<b>Zigbee</b>	256 Kbps	1000	2.4	Ultra low	128 bit AES
<b>Bluetooth</b>	1 Mbps	100	2.4	low	LFSR
<b>IrDA</b>	4 Mbps	1	Above 100	low	Line of light
<b>Wireless USB</b>	480 Mbps	10	3.1-10.6	low	128 bit AES

#### **1.4 Thesis overview**

The objective of this thesis is to investigate and design a fiber optic current sensor operating at telecommunication wavelength to measure DC and to achieve a wireless sensing system for the FOCS. The architecture of a FOCS can be divided into a basic scheme measuring DC by monitoring the state of output polarization and a reflective

scheme measuring DC by detecting reflected light intensity. For the integration of FOCS, an wireless sensing system is also designed and demonstrated to achieve wireless FOCS sensing system, as shown in Figure 1-5.

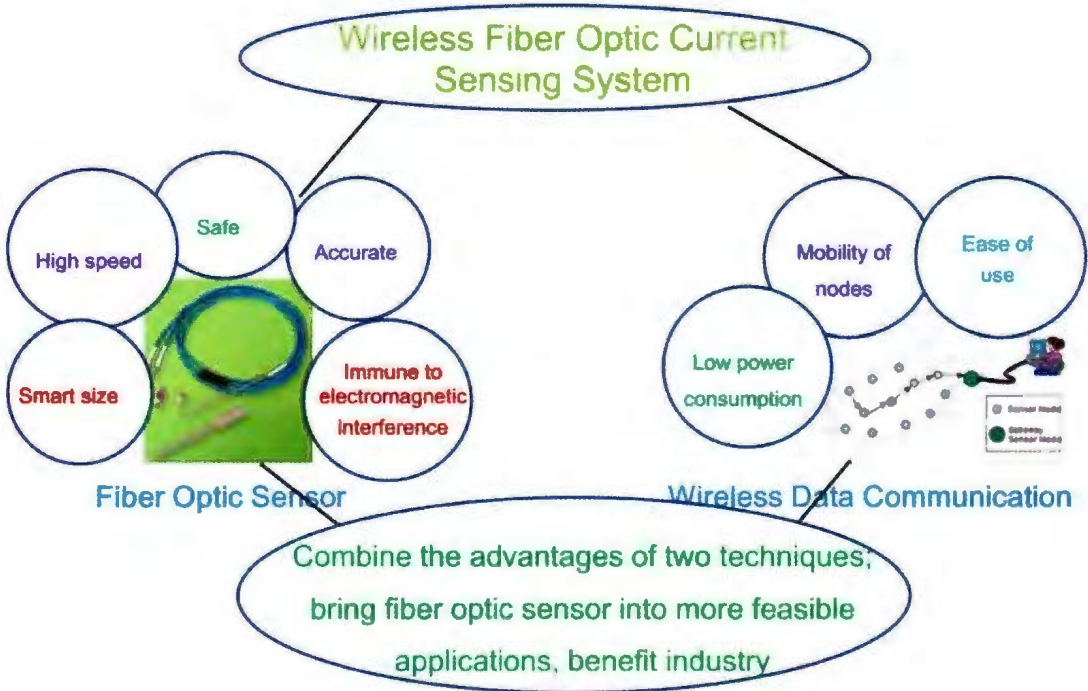


Figure 1-5 Architecture of a fiber optic current sensing system with wireless data communication.

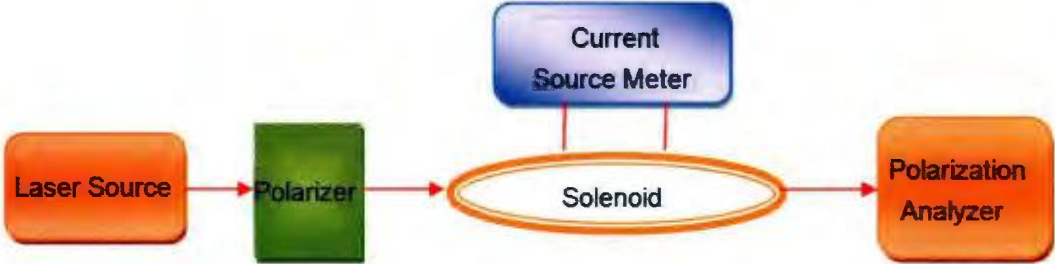


Figure 1-6 Basic scheme of a FOCS

As shown in Figure 1-6, the experimental setup of a FOCS in the basic scheme includes a laser source, an inline polarizer, a polarization analyzer, and a home-made solenoid which is connected to an electrical current power supply (BK Precision 1760A) to produce applied magnetic flux density along the optical path. The detecting device, a polarization analyzer (Agilent 8509C), can also be replaced by a photodetector and an inline polarizer placed before the photodetector to measure the light intensity which encodes the sensing signal.

The operation of FOCS is based on the Faraday magneto-optic effect. A light beam from a laser source is first launched into a fiber. Next, the light beam in the fiber is polarized to form a polarization state. This polarization state in the fiber is then modified by a magnetic field when the fiber is coiled around an electrical conductor carrying a large electrical current. Finally, the modified polarization state causes a variation in the output light intensity or polarization state, which can be measured by a photodetector or a polarization analyzer, respectively.

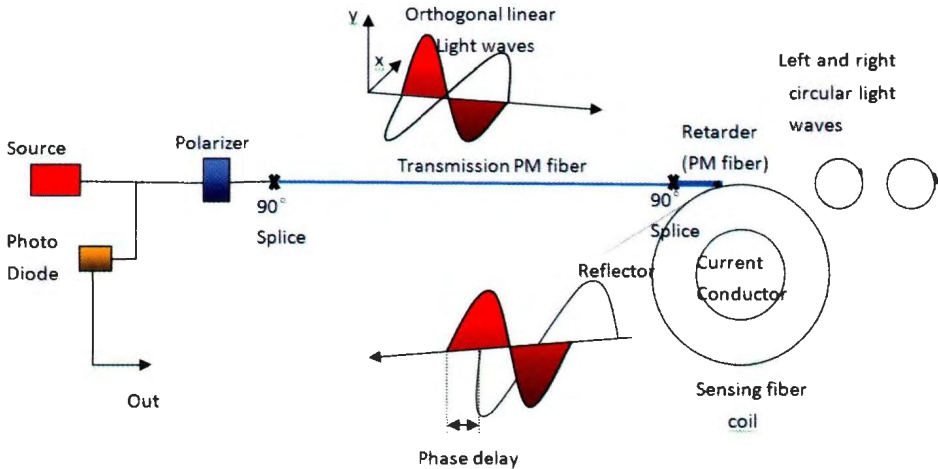


Figure 1-7 Reflective scheme of FOCS

As shown in Figure 1-7, the experimental setup of the FOCS in reflective scheme can be divided into four components: transmitter, optics, sensing head, and receiver. The transmitter injects a source laser pulse through an optical fiber into the inline polarizer after which it is then split into two orthogonal linear light waves by  $90^\circ$  splice. The orthogonal linear light waves are maintained by the polarization maintaining (PM) fiber until arriving at quarter-wave retarder where the waves form the combination beams of left and right circular light before injecting into the sensing fiber. After propagating through the sensing fiber, a phase delay of the two waves is induced. Then the two waves go back through the retarder, the PM fiber and the polarizer to the receiver. The receiver utilizes a photodiode to detect the interference due to the phase delay, and then the digital signal is processed and displayed by the signal processor unit.

The transmitter plays an important role in generating two orthogonal linearly polarized light waves for the FOCS. It consists of a laser source operating at 1550 nm wavelength, an inline polarizer, and a  $90^\circ$  splice of the linear polarization state which splits one beam of linearly polarized light into a pair of orthogonal linear state. The stability of the laser is very important since any change in the value of the amplitude or frequency of the light pulse will be viewed as a change in the current being measured. For this consideration, a highly stable laser source with internal thermal compensation and resistance of temperature fluctuations is required. Normally, the laser source comes out from a pigtailed single-mode optical fiber terminated with an angled connector, which results in a high coupling efficiency from the laser to the fiber. Before the linearly polarized wave is injected into the PM fiber, it is necessary to make the orientations of the

two linearly polarized waves orthogonal to each other. For this purpose, the orientation of the inline polarizer is set to the azimuth of  $45^\circ$  connected with the fast and slow axes of the PM fiber to split one beam of linearly polarized wave into a pair of orthogonal waves.

There are two important segments of optical fibers utilized in FOCS, which are a PM fiber and a sensing fiber. PM fiber plays a crucial role in maintaining the polarization states of the transmitted light while the sensing fiber is the core fiber to acquire sensing phase delay and discard noise and interference. The polarization state of the light traveling in a medium can be significantly influenced by stress within the material and this can induce problems with ordinary single mode fiber. When a normal fiber is bent or twisted, strain will occur in the fiber and the strain will change the polarization state of light traveling through the fiber. Furthermore, if the fiber is subjected to an external perturbation such as temperature fluctuation, then the final output polarization will be unpredictable with time. This is true for even short lengths of fiber and is undesirable in many applications.

The sensing head, a sensing fiber coil, is the key component of the FOCS. Since the polarized light experiences Faraday magneto-optic effect during propagation, its plane of polarization will be rotated. The sensing fiber requires a very low linear birefringence for this rotation to take place because a high linearly birefringent fiber may disturb the magnetically induced circular birefringence of the Faraday effect. When fibers are carefully made, they can have low linear birefringence. However, as the fiber is bent or cornered under transverse pressure, the birefringence will increase. Since the linear birefringence interferes with the Faraday effect-induced rotation, even a small change in

linear birefringence will make the Faraday rotation nearly immeasurable, which can catastrophically reduce the electrical current sensitivity. Some approaches have been adopted by researchers for reducing the problems caused by linear birefringence in the fiber [18, 19]. The most well-known approach is to create a high circular birefringence into the fiber or use a fiber with high intrinsic circular birefringence. Circular birefringence causes a rotation of the plane of polarization that adds little to that induced by the Faraday effect. When the circular birefringence is sufficiently larger than the linear birefringence caused by bending, other effects will have little effect on the final polarization.

Receiver design is another crucial part of the FOCS. It combines a photodiode to detect the intensity of the interference of the two waves and a receiver circuit that is used to process and display the digital signals. The function of the photodiode is to receive intensity of the light signals from interference of two output waves and converts them to the voltage signals which can be processed by the receiver circuits afterwards. On the selection of suitable receiver, PowerMeter 2832C from Newport is one of the best devices for FOCS because it is a fast and accurate photodiode with a built-in operational amplifier. Since it is an integrated combination of photodiode and operational amplifier, many inconsistencies and additional noise factors which are introduced by a standalone amplifier are eliminated. Intensity modulated optical signals from the sensor are converted to voltage signals and amplified by the photodiode.

Different from the traditional fiber sensing system, wireless data communication technology is employed in the fiber optic current sensing system, as shown in Figure 1-5.

This sensing system is easy to adopt portable fiber optic sensors while reducing integrating expense. This system is also easy to form various sensing network consisting of increased number of multiplexing sensors with low installation cost and low power consumption.

In the sensor node, the voltage signal is firstly fed to an Analog to Digital Converter (ADC), embedded in a microprocessor, through a differential amplifier. The differential amplifier brings the voltage signal to satisfy the ADC's input range of analog signal and also to increase the sensitivity of the FOCS. The output digital signal is then sent to the microprocessor that is designed to extract and process the useful information. After that, the information is sent to the wireless modules which will send the data via wireless communication to a personal computer (PC) to display, process, and store.

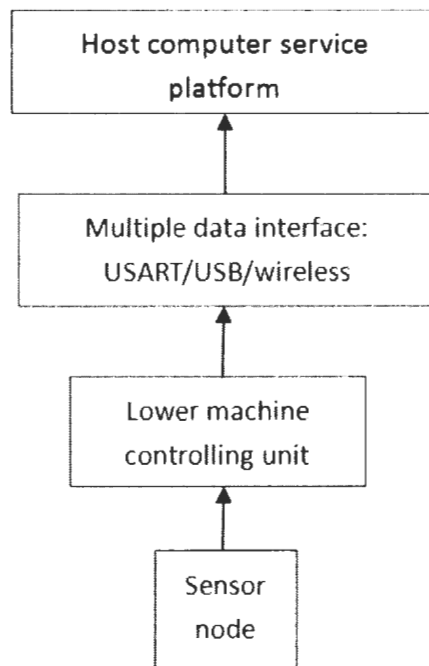


Figure 1-7 Architecture of a wireless fiber optic current sensing system

The wireless data communication can be achieved by a variety of unlicensed wireless networks or commercial networks operating at a wide radio frequency range, such as Zigbee, Bluetooth, TransferJet, Cellular networks, and GPRS. Zigbee network is the one deployed to achieve wireless sensing network for FOCS in this study. A Zigbee coordinator, interfaced with a PC as the host service platform, is firstly setup to establish a Personal Area Network (PAN) by scanning and defining the network name and communication channel of the PAN. Secondly, a Zigbee router or a Zigbee end device can be added to the built PAN to form a type of PAN, such as bus, ring, star, and mesh network. Finally, a Zigbee end device, sometimes a Zigbee router, is connected to a sensor to allow data interface between the PAN and signal processing units.

The host service platform is a written program that can be designed and developed on different programming language operating on a PC to interface and serve for the PAN. The service software in this thesis was developed on Microsoft Visual Basic 6.0. through which the host service platform can interface with the PAN via a Mscomm module. The designed and test host service platform can acquire, process, display, and store the sensing data in real-time.

There are many advantages of the work in this thesis. Firstly, the achievement of FOCS at telecommunication wavelength is possible to reduce the integration cost of FOCS in practical applications, such as, circuit breakers or bushings, control, and protection in high voltage substations as a result of its exponentially reduced size and weight. Secondly, the ability of FOCS to measure DC is promising to broaden the applications of FOCS, such as in metering, electro-chemistry, and railway system, leading

to reductions in space and installation cost. Finally, incorporation of wireless communication technology in a FOS can overcome many difficulties in traditional sensing systems, achieving significant improvement in performance, such as extending sensing distance, promoting types of FOSs other than FBGs, increasing the number of multiplexed sensors, and reducing the cost of remote sensing.

For the organization of this thesis, following Chapter 1 with an introduction, Chapter 2 describes and discusses background knowledge on the optical parameters important for current measurement, including polarization, Jones calculus, Poincare sphere, and Faraday magneto-optic effect. Chapter 3 investigates the design of FOCS in basic scheme and reveals the dependence of sensitivity on parameters, including various types of birefringence and input state of polarization from both simulation and experimental perspectives. Chapter 4 further discusses the design of FOCS in reflective scheme and theoretically and experimentally examines the dependence of sensitivity on parameters, including deviation of retarder, connection azimuths between connecting fibers, and length of PM fiber. Chapter 5 discusses the design and performance of wireless sensing system for FOCS, including system design, hardware layout, software design, and in-situ performance. Chapter 6 summarizes the work and conclusions in this thesis and proposes future work.

## **Chapter 2 Faraday Magneto-optic Effect in Fibers**

### **2.1 Fundamentals of Faraday magneto-optic effect in an optical fiber**

Since a FOCS achieves current sensing by monitoring the change in the polarization state of a beam of light, it is essential to introduce and discuss some fundamental concepts and terminologies before further elaboration on FOCS. These fundamental concepts include polarization, Jones calculus, Poincare sphere and Stokes parameters, and Faraday magneto-optic effect.

Polarization is the state of a beam of light transmitting in a fiber. The polarization of a beam of light is employed to encode sensing information in a FOCS system, though the polarization evolution of the light in a fiber usually suffers from different influences. Jones calculus is a mathematical method used to describe the polarization state of a propagating light wave and the operation on the polarization state of each optical component along the optical path, in which the polarization state is viewed as a vector and the optical components are regarded as matrices. Poincare sphere, together with Stokes parameters, is a visual tool to describe all the complex polarization states in both qualitative and quantitative description. Faraday magneto-optic effect is a phenomenon, in which the orientation of linearly polarized light propagating along the direction of applied magnetic field in a Faraday material, such as a SMF-28e fiber, will rotate. As the magnetic field can be produced by electrical current according to Ampere's circular law, Faraday magneto-optic effect can be used to sense electrical current.

### 2.1.1 Polarization

The polarization of light was first discovered by a Danish professor Erasmus Bartholinus and described in a publication in 1669 [78]. This description reveals the refraction seen in a crystal called Iceland spar, now called calcite. After extensive studies of this phenomenon by Huygens, Malus, Brewster, Young and the others [79], the theory of polarization is now generally considered as well developed. Normally the orientations of the electric field components of light are randomly distributed and this kind of light is called unpolarized light. A polarized beam of light is one in which the electric field components of all the waves have similar orientation.

The orientation characteristics of the electric field representing a polarized light determine the state of polarization (SOP) of the wave. If a travelling wave is seen from the point of view of a receiver, the travelled trace of the plane of the electric field is a measure of the polarization. The angular orientation of this trace is known as the orientation of the wave. If the trace is a straight line, the wave is said to be linearly polarized. It is called circularly polarized light if the trace is a circle. The circularly polarized light is further divided into right and left circularly polarized light depending upon the direction of the circular helix. If it is clockwise then it is known as right circularly polarized light and if counter-clockwise then left circularly polarized light.

Any vector representing a polarized light beam can be divided into a pair of mutually orthogonal components of the electric field travelling along the direction of propagation of light. In other words, the electric field vector of the polarized light is a vectorial sum of

these two orthogonal components. Therefore the intensity, the orientation and the type of polarized light depend upon these orthogonal components. These components lie along the  $x$  and  $y$  axes.

If the  $x$  and  $y$  components are in phase then the resultant wave is linearly polarized. The orientation of this linearly polarized light depends upon the relative amplitudes of the two components, and if their amplitudes are equal then the orientation is at  $45^\circ$ . The orientation of polarized light is measured traditionally with respect to the  $x$ -axis. If  $A_x$  and  $A_y$  are the amplitudes of the  $x$  and  $y$  orthogonal components respectively, then the orientation of resultant linearly polarized light can be described by  $\tan^{-1}(A_y/A_x)$ .

When the two orthogonal components are equal in amplitude and are  $90^\circ$  out of phase then the resultant wave is said to be circularly polarized. Circularly polarized states are distinguished by the rotation of the vector. When the resultant vector rotates clockwise if viewed from the point of view of a receiver, it is called right circularly polarized light. When the resultant vector rotates counter-clockwise viewed from the point of view of a receiver, it is called left circularly polarized light. Circularly polarized light does not have any orientation as such and it is described by its amplitude and direction of rotation only.

For other situations when the two components have different amplitudes and have a phase delay, or have equal amplitudes but a phase difference other than  $90^\circ$ , the result is elliptically polarized light. Generally, all the polarized light can be termed as elliptically polarized with linear and circular polarization as its special cases.

### 2.1.2 The Jones calculus

In optics, Jones calculus is used to describe polarized light [79, 80]. In 1941, R.C. Jones determined that polarized light could be represented by a  $2 \times 1$  column vector which is known as the Jones vector [80]. Each element of the Jones vector describes one component of the electric vibration at the given location. Generally, the upper element indicates the amplitude and phase of the  $x$ -component and the lower element describes for the  $y$ -component. Jones calculus is only applicable to light that is already fully polarized in which all wavelengths of the light beam are polarized.

Suppose there is a beam of polarized light propagating along the direction of  $z$ -axis which can be considered as a plane wave with the speed of light  $c$  and frequency  $\omega$ . Its electric field vector  $\mathbf{E}$  can be specified by way of two orthogonal components  $E_x$  and  $E_y$ , with amplitude  $A_x$ , and  $A_y$ , and initial phase angles  $\phi_x$  and  $\phi_y$  respectively, thus [80]

$$E_x = A_x \cos\left[\omega\left(t - \frac{z}{c}\right) + \phi_x\right] = \text{Re}\{A_x \exp i[\omega\left(t - \frac{z}{c}\right) + \phi_x]\} \quad (2-1)$$

and

$$E_y = A_y \cos\left[\omega\left(t - \frac{z}{c}\right) + \phi_y\right] = \text{Re}\{A_y \exp i[\omega\left(t - \frac{z}{c}\right) + \phi_y]\} \quad (2-2)$$

When  $A_x = A_y$  and  $|\phi_x - \phi_y| = 90^\circ$ ,  $\mathbf{E}$  is circularly polarized;

When  $|\phi_x - \phi_y| = 0$ ,  $\mathbf{E}$  is linearly polarized.

In the general case,  $\mathbf{E}$  is elliptically polarized. The above equations can be rewritten in a different form as follows [80]

$$\begin{pmatrix} E_x \\ E_y \end{pmatrix} = \begin{pmatrix} A_x e^{i\phi_x} \\ A_y e^{i\phi_y} \end{pmatrix} e^{i[\omega(t-z/c)]} \quad (2-3)$$

For simplified expression by ignoring the propagating component,  $E$  can be represented as a column vector which is called the Jones vector [80]

$$\begin{pmatrix} E_x \\ E_y \end{pmatrix} = \begin{pmatrix} A_x e^{i\phi_x} \\ A_y e^{i\phi_y} \end{pmatrix} \quad (2-4)$$

Table 2-1 List of Jones vectors describing SOP

Description of SOP	Jones vector
Linearly polarized light with the orientation of the $x$ -axis	$\begin{pmatrix} 1 \\ 0 \end{pmatrix}$
Linearly polarized light with the orientation of the $y$ -axis	$\begin{pmatrix} 0 \\ 1 \end{pmatrix}$
Linearly polarized light which is $45^\circ$ oriented with both with $x$ -axis and $y$ -axis	$\frac{1}{\sqrt{2}} \begin{pmatrix} 1 \\ 1 \end{pmatrix}$
Linearly polarized light which is $45^\circ$ oriented with both with $x$ -axis and negative $y$ -axis	$\frac{1}{\sqrt{2}} \begin{pmatrix} 1 \\ -1 \end{pmatrix}$
A beam of right-circular polarized light	$\frac{1}{\sqrt{2}} \begin{pmatrix} 1 \\ i \end{pmatrix}$
The left-circular polarized light	$\frac{1}{\sqrt{2}} \begin{pmatrix} 1 \\ -i \end{pmatrix}$

The Jones vector descriptions of some typical SOPs have been summarized in Table 2-1.

Jones also found that a polarization device can be represented as a  $2 \times 2$  matrix which is known as the Jones matrix [80]. When the polarized light propagates through the polarization device, the output light can be described by another column vector which is the product of the Jones matrix of the device and the Jones vector of the input light as shown below [80]:

$$\begin{pmatrix} E_{2x} \\ E_{2y} \end{pmatrix} = \begin{pmatrix} J_{11} & J_{12} \\ J_{21} & J_{22} \end{pmatrix} \begin{pmatrix} E_{1x} \\ E_{1y} \end{pmatrix} \quad (2-5)$$

In general, the four elements of the Jones matrix,  $J_{11}$ ,  $J_{12}$ ,  $J_{21}$ , and  $J_{22}$ , are complicated and dependent on the device. For instance, a quarter-wave plate which is an important optical component can provide a  $90^\circ$  phase delay between the two orthogonal components of the polarized light. If the orientation angle of the quarter-wave plate is  $45^\circ$ , then its Jones matrix is

$$J = \frac{1}{\sqrt{2}} \begin{pmatrix} 1 & i \\ -i & 1 \end{pmatrix} \quad (2-6)$$

If the Jones vector for the input light is  $E_{in} = \begin{pmatrix} 0 \\ 1 \end{pmatrix}$ , the output light which can be calculated as a product of these matrices

$$E_{out} = \frac{1}{\sqrt{2}} \begin{pmatrix} 1 & i \\ -i & 1 \end{pmatrix} \begin{pmatrix} 0 \\ 1 \end{pmatrix} = \frac{1}{\sqrt{2}} \begin{pmatrix} 1 \\ i \end{pmatrix} \quad (2-7)$$

This is a beam of right circular polarized light.

The Jones matrix for any material which rotates the polarized light by an angle  $\theta$  is given by [80]

$$R = \begin{pmatrix} \cos \theta & \sin \theta \\ -\sin \theta & \cos \theta \end{pmatrix} \quad (2-8)$$

### 2.1.3 Poincare sphere and Stokes parameters

Poincare sphere and Stokes parameters, which are usually used by polarization analyzer, for instance Agilent 8509C, are powerful tools to record and express the SOP as shown in Figure 2-1 [78]. All SOPs can be displayed on the surface of the Poincare sphere. The three axes of the Poincare sphere coordinates  $S_1$ ,  $S_2$ , and  $S_3$  as well as an additional parameter of light intensity  $S_0$  are called Stokes parameters.

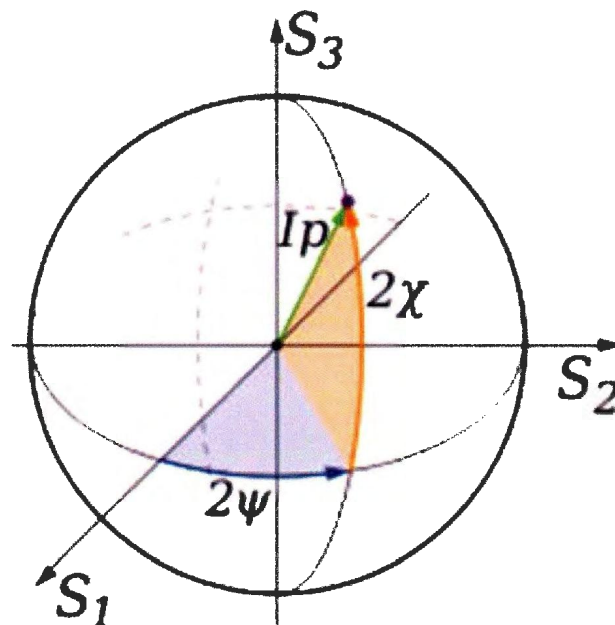


Figure 2-1 Poincare sphere and Stokes parameters

The relationship between Stokes parameters, degree of polarization, beam intensity and polarization ellipse parameters can be defined through the following equations [81, 82]

$$S_0 = I \quad (2-9a)$$

$$S_1 = pI \cos 2\psi \cos 2\chi \quad (2-9b)$$

$$S_2 = pI \sin 2\psi \cos 2\chi \quad (2-9c)$$

$$S_3 = pI \sin 2\chi \quad (2-9d)$$

where  $S_0, S_1, S_2,$  and  $S_3$  are the four stokes parameters;  $p$  is the degree of polarization;  $I$  is the total intensity of the light beam;  $\psi$  is the angle between the polarization orientation and the  $x$ -axis; and  $2\chi$  is the angle between the major-axis of the elliptical polarization and the  $x$ -axis, as shown in Figure 2-1.

Sometimes, normalized  $s1, s2$  and  $s3$  are used to replace  $S_1, S_2,$  and  $S_3$  respectively [81, 82].

$$s1 = S_1 / S_0 \quad (2-10a)$$

$$s2 = S_2 / S_0 \quad (2-10b)$$

$$s3 = S_3 / S_0 \quad (2-10c)$$

The polarization analyzer, Agilent 8509C, utilizes Stokes parameters  $S_0, s1, s2$  and  $s3$  to record SOP. If stokes parameters are given, Poincare sphere coordinates can be solved by the following equations: [82]

$$I = S_0 \quad (2-11a)$$

$$p = \frac{\sqrt{S_1^2 + S_2^2 + S_3^2}}{S_0} \quad (2-11b)$$

$$2\psi = \arctan \frac{S_2}{S_1} = \arctan \frac{s_2}{s_1} \quad (2-11c)$$

$$2\chi = \arctan \frac{S_3}{\sqrt{S_1^2 + S_2^2}} = \arctan \frac{s_3}{\sqrt{s_1^2 + s_2^2}} \quad (2-11d)$$

## 2.2 Faraday magneto-optic effect in various types of fibers

### 2.2.1 Faraday magneto-optic effect

Faraday magneto-optic effect, also called Faraday effect and discovered by Michael Faraday in 1845, is the theoretical basis of the FOCS [1, 13]. Faraday found that when polarized light propagates through an optically active material in a direction parallel to the applied magnetic field, such as a piece of glass, its plane of polarization rotates and this rotation angle is proportional to the magnitude of the applied magnetic field. The process of Faraday effect is shown in Figure 2-2 with the angle of rotation is expressed as [13].

$$\Omega = V \int_0^L \vec{H} \cdot \vec{dl} \quad (2-12)$$

where  $\Omega$  is the angle of rotation,  $V$  is the Verdet constant of Faraday material (rad/ampere),  $\vec{H}$  is the magnetic field intensity, and  $L$  is the length of the optical path.

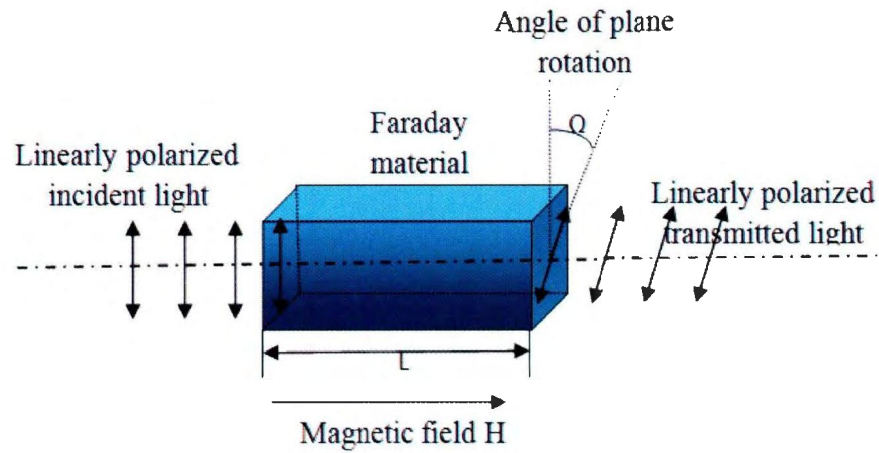


Figure 2-2 Principle of Faraday effect

When the magnetic field is uniform and the optical path lies in the same direction as the magnetic field, the above equation can be simplified as [13]:

$$\Omega = VHL \quad (2-13)$$

When the propagation direction differs from the magnetic field direction by an angle  $\theta$ , the rotation is given by:

$$\Omega = VHL \cos \theta \quad (2-14)$$

When the polarized light propagates through a Faraday material (such as optical fiber) near a current carrying conductor, then, according to Ampere's circuital law [2]:

$$\int_0^L \vec{H} \cdot d\vec{l} = N_i i \quad (2-15)$$

The rotation angle  $\Omega$  can be given in Eqn. (1-6).

Linear light can also be represented by a pair of co-propagating left and right circularly polarized light waves [1, 12]. In an applied magnetic field, the two circular waves travel with different speeds and thus accumulate a phase difference after propagation through the Faraday material, which causes the rotation by an angle  $\phi_F$  of the resultant linear wave. In a FOCS, the light travels along a closed path surrounding the conductor. In a reflective scheme the phase difference is given by [19]:

$$\phi_F = 4\Omega = 4V \int_0^L \overline{H} \bullet \overline{dl} = 4VN_f N_i i \quad (2-16)$$

As a result of the closed path, the signal depends only on the current and the number of fiber loops, and not on dimensional parameters such as the diameter or the shape of the fiber.

### 2.2.2 Verdet constant

The Verdet constant is mostly explained in microscopic theory. The dependence of the Verdet constant on the wavelength and the refractive index is given by [79]

$$V = \gamma \frac{e_0}{m_0} \cdot \frac{\lambda}{2c} \cdot \frac{dn}{d\lambda} \quad (2-17)$$

where  $\gamma$  is the magneto-optical constant,  $e_0/m_0$  is the specific charge of the electrons,  $c$  is the velocity of light,  $\lambda$  is the wavelength,  $n$  is the refractive index of the material at a wavelength of  $\lambda$ , and  $dn/d\lambda$  is the dispersion.

As shown in Eqn. (2-17), Faraday effect is a dispersion effect which can be interpreted in terms of the space anisotropy introduced by the magnetic field [83]. Since

the effect of the magnetic field on the right and left circularly polarized states is different, the refractive indices and the propagation constants are also different for each state of polarization, which results the rotated polarization plane for a linearly polarized light wave. The Verdet constant is also temperature, wavelength, and sometimes field-dependent parameter, and it is different for different materials.

Although a Verdet constant is usually less dependent on temperature [22], the value of the Verdet constant depends strongly on wavelength. Since reports of Verdet constants at telecommunication wavelength are very scarce, we calculated the Verdet constants of various Faraday materials, such as Ce, Pr, Tb, and Dy ion doped crystals, with large Verdet constants, and found Verdet constants' dependence on their wavelengths shown in Figure 2-3, following the relationship between Verdet constants and wavelength revealed in Ref [22]:

$$V = K(\lambda^2 - \lambda_0^2)^{-1} \quad (2-18)$$

where  $K$  is a parameter independent of incident wavelength  $\lambda$ , but a function of  $\lambda_0$ ;  $\lambda_0$  is the observing wavelength.

Thus, the expression of fitting equations of the curves in Figure 2-3 can be listed in Table 2-2.

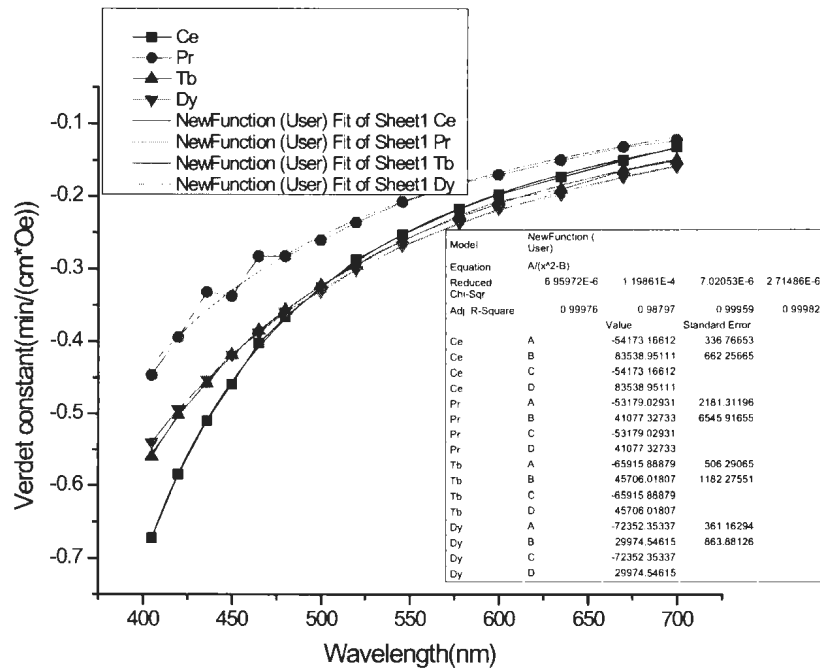


Figure 2-3 Relationships between Verdet constant and wavelength for Ce, Pr, Tb, and Dy ion doped phosphate crystals

For practical applications, the Verdet constants of different materials at each wavelength are not always available. Thus, it is essential to employ these fitting equations to predict the Verdet constant of various Faraday material at a specific wavelength, such as at 1550 nm. The theoretical prediction and experimental test of the Verdet constant of a single-mode fiber from 478 nm to 1523 nm in Ref. [84] have verified this prediction method with reasonable agreement. Therefore, we utilized these fitting equations here to predict the Verdet constants of various materials at 1550 nm to guild the selection of suitable sensing fibers, shown in Table 2-2.

Table 2-2 Predictions of Verdet constants of various materials at 1550 nm

Element	Fitting equation	Verdet constant at 1550 nm( rad/Tm)
Ce	$V = -54173.16(\lambda^2 - 83538.95)^{-1}$	-6.783
Pr	$V = -53179.03(\lambda^2 - 41077.32)^{-1}$	-6.539
Tb	$V = -65915.89(\lambda^2 - 45706.02)^{-1}$	-8.121
Dy	$V = -72352.35(\lambda^2 - 29974.55)^{-1}$	-8.856

These calculations indicate that the Tb and Dy ions possess larger Verdet constants, thus it is reasonable to predict that Tb and Dy ions as the dopants in rare-earth doped fibers could possess high Verdet constants as well.

### 2.2.3 Faraday magneto-optic effect in different fibers

Besides the theoretical predication, the Verdet constants of different kinds of sensing fibers can be experimentally determined in basic scheme, shown in Figure 2-4. By observing the recorded Stokes parameters and Faraday rotation from a polarization analyzer (Agilent 8509C), the orientations of the output SOP are determined by [82]:

$$\phi_{out} = \frac{1}{2} \arctan \frac{s_2}{s_1} \quad (2-19)$$

where  $s_1$  and  $s_2$  are the two of the four Stokes parameters.

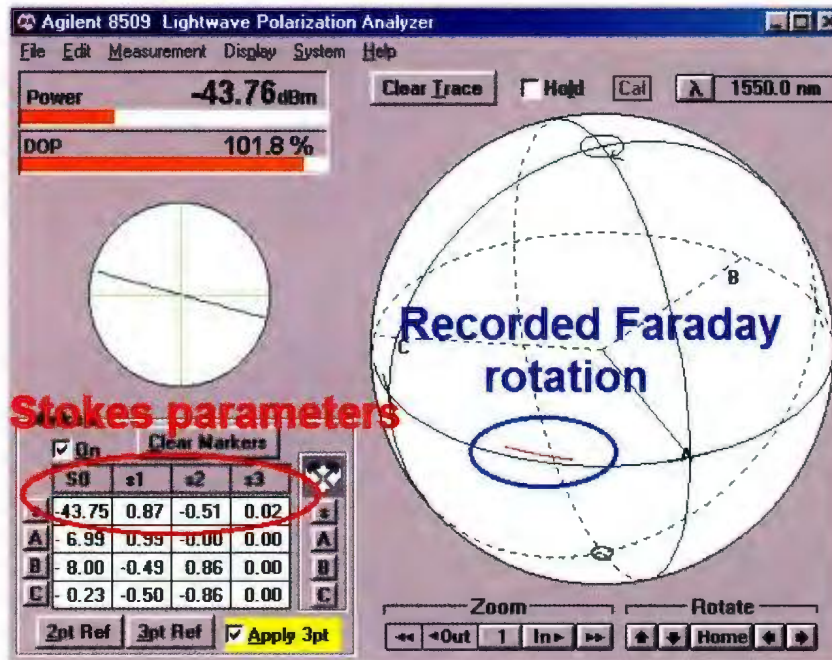


Figure 2-4 Recorded Stokes parameters and Faraday rotation

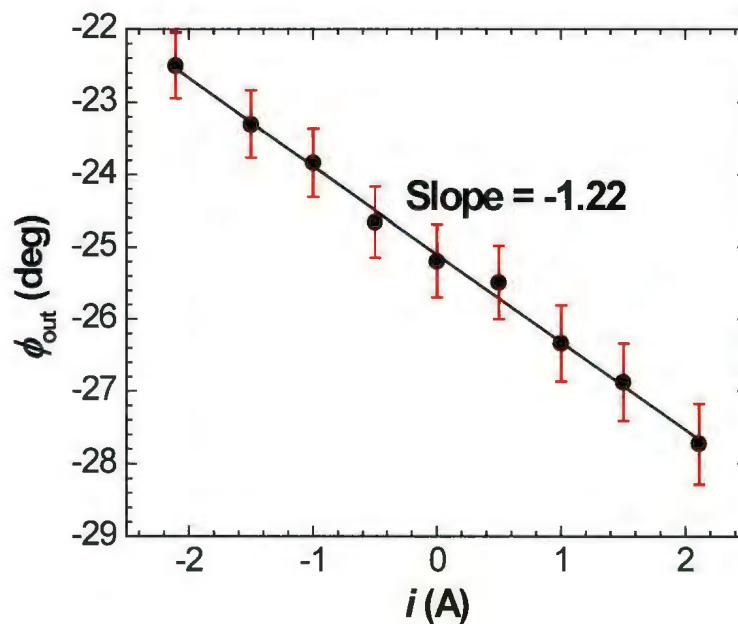


Figure 2-5 Relationship between the orientation of output SOP and current  $i$  with systematic error in a single-mode fiber (SMF-28e)

As

$$\phi_{out} = \phi_0 + \phi_F = VN_f N_i i + \phi_0 \quad (2-20)$$

where  $\phi_0$  is the initial orientation of input light;  $\phi_F$  is the Faraday rotation angle.

thus

$$Slope = VN_f N_i \quad (2-21)$$

Verdet constant can be determined by

$$V = \frac{Slope}{N_f N_i} \quad (2-22)$$

The slope can be measured shown in Figure 2-5 with the data in Table 2-3.

Table 2-3 Record and calculation of the orientations of output SOP with systematic error in single-mode fiber (SMF-28e)

Current $i$ (A)	S0	s1	s2	s3	$\phi_{out}$ (deg)
-2.108	-17.62	0.53	-0.53	-0.59	-22.5017
-1.500	-17.61	0.52	-0.55	-0.59	-23.3047
-1.000	-17.59	0.51	-0.56	-0.59	-23.8394
-0.500	-17.59	0.49	-0.57	-0.6	-24.6598
0.000	-17.58	0.48	-0.58	-0.6	-25.1965
0.500	-17.56	0.47	-0.58	-0.6	-25.4922
1.000	-17.57	0.45	-0.59	-0.6	-26.3353
1.500	-17.55	0.44	-0.6	-0.6	-26.8751
2.108	-17.53	0.42	-0.61	-0.6	-27.7279

Table 2-4 The experimental comparison of the Verdet constants of various sensing fibers

Sensing fibers	Source	Measured Verdet constant with systematic error		Measured Verdet constant without systematic error <sup>1</sup>		Reported value of Verdet constant (rad/A)
		(rad/A)	Error	(rad/A)	Error	
Single-mode (SMF-28e)	Corning Inc.	0.4±0.03	33%	0.63±0.05	5%	0.6 [85]
Er-doped <sup>2</sup> (F-EDF)	Newport Inc.	0.14±0.03	-	0.22±0.01	-	NA
Er-doped <sup>2</sup> (F-EDF-2)	Newport Inc.	0.13±0.02	-	0.36±0.02	-	NA
Er-doped <sup>2</sup> (F-EDF-5)	Newport Inc.	0.12±0.003	-	0.46±0.003	-	NA
Multi-mode (INFINICOR600)	Corning Inc.	Unstable <sup>3</sup>	-	Unstable <sup>3</sup>	-	-
PM fiber (PM 15-U40A)	Corning Inc.	0	-	0	-	-
Tb-doped fiber <sup>4</sup>	Advanced Photonics Inc.	10.4±0.1	-	10.9±0.1	-	NA

<sup>1</sup> Systematic error results from the intrinsic and bend-induced birefringence of the fibers which quenches the slope of fitting curves. Systematic error can be eliminated by applying twist-induced birefringence 0.917 rad/m and it improves the value of Verdet constant to be a real value, which is studied in Chapter 3;

<sup>2</sup> The Er-doped fibers are tested at 1592 nm to avoid the influence of absorption peak around 1531 nm of Erbium dopant, shown in Figure 2-6, while the other types of sensing fibers are tested at 1550 nm;

<sup>3</sup> The recorded output SOP on Poincare sphere is not stable due to multiple transmitted light modes, which indicates that the Verdet constant of multi-mode fiber cannot be determined.

<sup>4</sup> The Tb-doped fiber was provided by Advanced Photonics Company, and the specifications of the Tb-doped fiber were not released by the manufacturer.

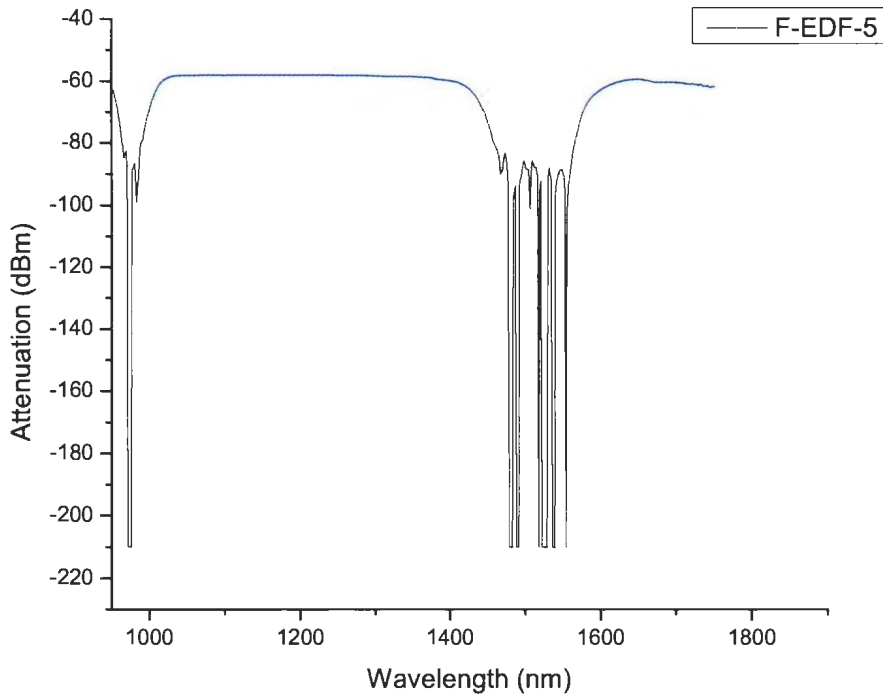


Figure 2-6 Transmitted spectrum of Er-doped fiber (F-EDF-5)

From the experimental result in Table 2-4, a single-mode fiber can reach a moderate value of Verdet constant. Er-doped phosphate fibers have a small Verdet constant while the value of Verdet constant can be improved by increasing the Erbium dopant ratio. Meanwhile, the Verdet constant of Er-doped fibers cannot be determined around 980 nm and 1531nm because of the absorption peaks of the Er ion, shown in Figure 2-6. Multi-mode and PM fibers are not suitable to be used as sensing fibers for FOCS because the Verdet constants of the multi-mode and PM fibers cannot be determined. Tb-doped fiber can achieve a very high Verdet constant and it has potential in the industrial applications

of FOCS to achieve high sensitivity. In our series of experiments, the single-mode fiber (SMF-28e) with low cost was chosen to study the properties of the FOCS. Since the Tb-doped fiber was a customized fiber which requires a long period of time to produce, the experimental study on the properties of FOCS using a Tb-doped fiber has not been included in this thesis.

## Chapter 3 Basic Scheme of Fiber Optic Current Sensor

### 3.1 Experimental setup of basic scheme

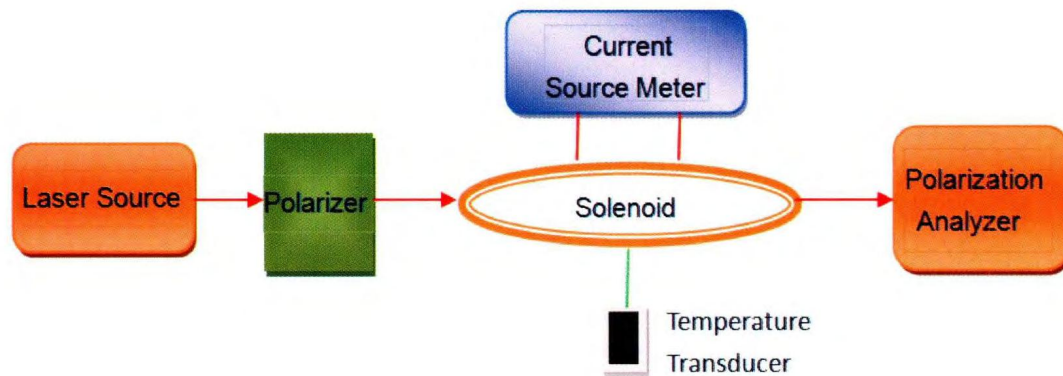


Figure 3-1 The basic scheme of a FOCS

In the basic scheme of FOCS (Figure 3-1), the Faraday rotation angle is measured by the polarization analyzer in order to derive the Faraday rotation angle as following [1, 13]:

$$\Delta\phi = \phi_F = VN_f N_f i \quad (3-1)$$

### 3.2 Effect of birefringence

#### 3.2.1 Origins of birefringence

In practice, several types of birefringence could be introduced in single-mode optical fiber due to either internal deformation or external action which usually produces an anisotropic refractive-index distribution in the core region.

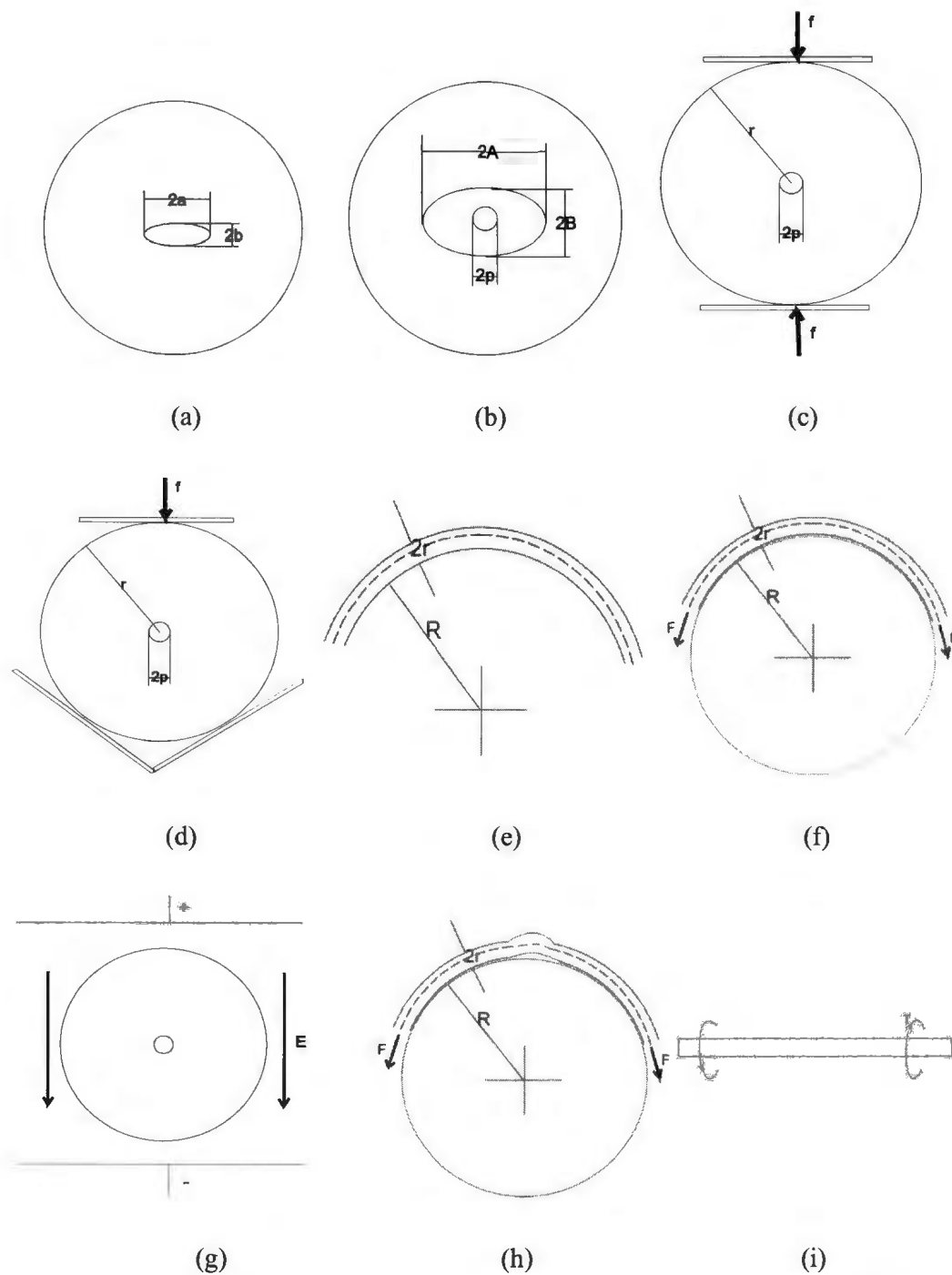


Figure 3-2 Nine types of birefringence mechanisms: (a) noncircular core; (b) internal lateral stress; (c) external lateral stress; (d) external lateral stress; (e) free bending; (f) tension bending; (g) tension & ring bending; (h) electrooptic effect; (i) twist

The origin of the birefringence is typically classified as the above nine mechanisms according to the study of Scott C. Rashleigh in 1983, as shown in Figure 3-2 [86]. In our experimental setup, there are three types of birefringence to be considered: (a) and (b) intrinsic linear birefringence; (e) bend-induced external linear birefringence; and (i) twist-induced circular birefringence.

The intrinsic linear birefringence, mostly originated from initial noncircular core and internal lateral stress-induced noncircular core, can be approximated by [86]

$$\delta_i \approx 0.2k_0 \left( \frac{a}{b} - 1 \right) (\Delta n)^2 \quad (3-2)$$

where  $k_0 = 2\pi/\lambda$  is the wave number,  $a$  and  $b$  are the major and minor core radii, and  $\Delta n = n_1 - n_2$  is the refractive-index difference between the core and cladding regions [86, 87].

The bend-induced linear birefringence is expressed as [86]

$$\delta_b = 0.25kn^3(p_{11} - p_{12})(1 + \nu_p) \frac{\rho^2}{R^2} \quad (3-3)$$

where  $n = 1.46$  is the refractive index of fiber core,  $\nu_p = 0.17$  is Poisson's ratio,  $p_{11} - p_{12} = -0.15$  the difference of the strain-optical tensor of fiber material,  $k = 2\pi/\lambda_{vac}$  is the wave number with  $\lambda_{vac} = 1550$  nm,  $\rho = 62.5$   $\mu\text{m}$  is the radius of fiber cladding, and  $R$  is the radius of the circular bent ( $R$  is about 2.0 ~ 20.0 cm in our series of experiments) [86].

Twist-induced circular birefringence is expressed by [86]

$$\delta_T = gT = g\phi_T / L \quad (3-4)$$

where twist constant  $g = -0.5 n^2_0 (p_{11} - p_{12}) = 0.146$  for silica fibers [86],  $T = \phi_T/L$  is the twist rate,  $\phi_T$  is the twisted angle of the sensing fiber, and  $L$  is the length of the twisted sensing fiber.

Faraday rotation angle can be viewed as the contribution of circular birefringence under applied magnetic field. Rewrite Eqn. (3-1):

$$\Delta\phi = \phi_F = VN_i N_f i = \frac{1}{2} \delta_H L \quad (3-5)$$

Thus, define

$$\delta_H = 2VN_i N_f i / L \quad (3-6)$$

as a magnetic field induced circular birefringence in our experiments.

### 3.2.2 Effects of birefringence on evolution of the propagating polarization

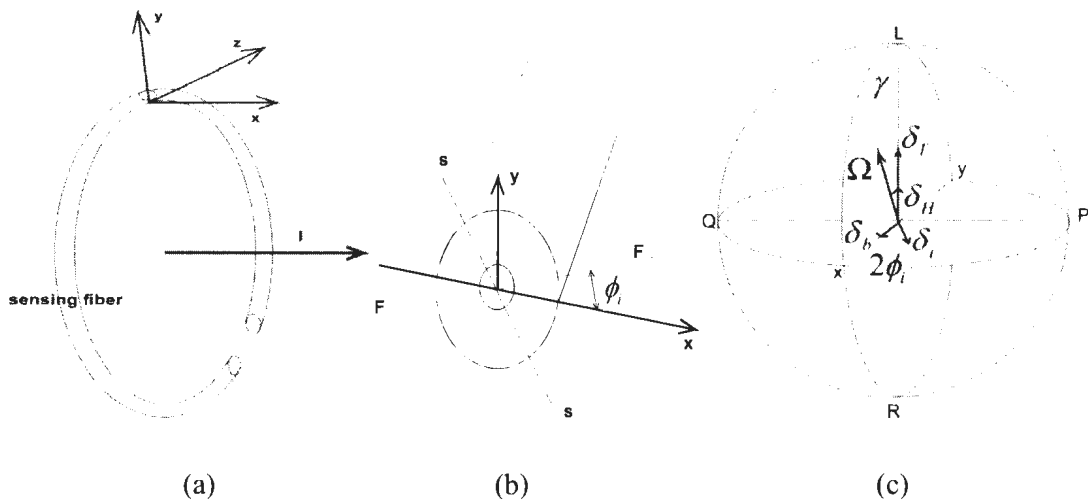


Figure 3-3 Definition of birefringence in fibers: (a) a bending fiber for sensing; (b) intrinsic birefringence in fiber; (c) birefringence on Poincare sphere.

A Poincare sphere is used to describe and analyze the evolution of propagating polarization states in sensing fibers. As shown in Figure 3-3(a), a local coordinator system is adopted to specify the horizontal and vertical polarization in a bent sensing fiber. Under this coordinator system, the intrinsic birefringence is defined in Figure 3-3(b) with the fast axis forming an angle  $\phi_i$  to the  $x$ -axis. The bend-induced and intrinsic birefringences cause all SOPs to rotate with angular velocities  $\delta_b$  and  $\delta_i$  respectively, lying in equatorial plane shown in Figure 3-3(c). The twist-induced and magnetic-induced birefringences cause all SOPs to rotate along vertical and horizontal plane with velocities  $\delta_T$  and  $\delta_H$  respectively shown in Figure 3-3(c). Thus the total effect can be derived as

$$\overline{\Omega}(z) = \overline{\delta}_i + \overline{\delta}_b + \overline{\delta}_T + \overline{\delta}_H \quad (3-7)$$

For an input SOP at  $z$ , the effect of birefringence on SOP is described by

$$d\overline{E}_{z+dz} / dz = \overline{\Omega}(z) \times \overline{E}_z \quad (3-8)$$

Integration along  $L$  with given input SOP, we derive

$$\overline{\Delta E} = \overline{\Omega} \times \overline{E}_m \quad (3-9)$$

where,

$$\overline{\Omega} = \oint_L \overline{\Omega}(z) dz = \oint_L (\overline{\delta}_i + \overline{\delta}_b + \overline{\delta}_T + \overline{\delta}_H) dz = \overline{\beta}_i + \overline{\beta}_b + \overline{\beta}_T + \overline{\beta}_H \quad (3-10)$$

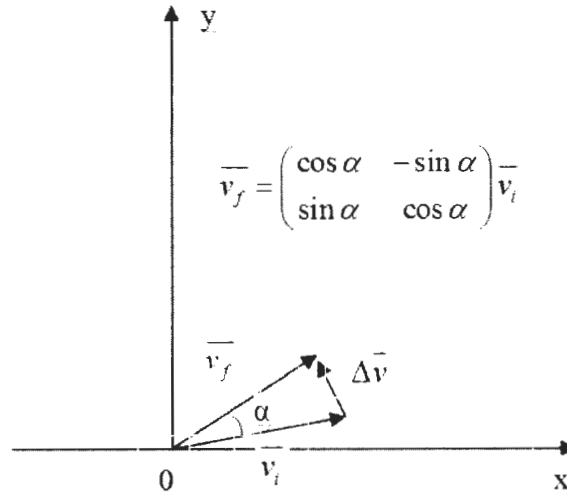


Figure 3-4 Illustration of vector rotation

Following the Eqn. (3-9) from a Jones matrix perspective with the illustration of vector rotation shown in Figure 3-4, it is possible to derive the following expression based on Refs. [89-92].

$$\begin{pmatrix} E_x \\ E_y \end{pmatrix}_{out} = \begin{pmatrix} A & -B \\ B & A^* \end{pmatrix} \times \begin{pmatrix} E_x \\ E_y \end{pmatrix}_{in} \quad (3-11)$$

where,

$$A = \cos(\Omega/2) + i \sin(\Omega/2) \sin \gamma;$$

$$B = \sin(\Omega/2) \cos \gamma;$$

$$\Omega = \{ [\beta_i \cos(2\phi_i + 2TL) + \beta_b]^2 + [\beta_i \sin(2\phi_i + 2TL)]^2 + (\beta_T + \beta_H)^2 \}^{1/2} \cdot \frac{\beta_T + \beta_H}{|\beta_T + \beta_H|};$$

$$\tan \gamma = \{ [\beta_i \cos(2\phi_i + 2TL) + \beta_b]^2 + [\beta_i \sin(2\phi_i + 2TL)]^2 \}^{1/2} / (\beta_T + \beta_H).$$

### 3.3 Dependence of sensitivity on parameters: simulation perspective

A general given input SOP can be expressed as:

$$\begin{pmatrix} E_x \\ E_y \end{pmatrix}_{in} = \begin{pmatrix} e^{i\phi_{in}} \cos \theta \\ \sin \theta \end{pmatrix}_{in} \quad (3-12)$$

where  $\theta$  is the angle of the orientation of the SOP with the  $x$ -axis, and  $\phi_{in}$  is the phase difference between the  $y$  component and the  $x$  component of the SOP.

Rewrite the Eqn. (3-11),

$$\begin{pmatrix} E_x \\ E_y \end{pmatrix}_{out} = \begin{pmatrix} A & -B \\ B & A^* \end{pmatrix} \times \begin{pmatrix} e^{i\phi_{in}} \cos \theta \\ \sin \theta \end{pmatrix}_{in} \quad (3-13)$$

Therefore, after we measured the output SOP by the polarization analyzer, the orientation of the output SOP should be determined by the following expression:

$$\phi_{out} = \tan^{-1} \left( \frac{E_{y-out}}{E_{x-out}} \right) = \tan^{-1} \left( \frac{(0 \ 1) \begin{pmatrix} E_x \\ E_y \end{pmatrix}_{out}}{(1 \ 0) \begin{pmatrix} E_x \\ E_y \end{pmatrix}_{out}} \right) \quad (3-14)$$

Since the orientation of the output SOP is determined by Eqn. (3-14), the relationship between  $\phi_{out}$  and the magnetic field induced circular birefringence  $\beta_H$ , or to say the electrical current  $i$ , can be found from Eqns. (3-11), (3-13) and (3-14) when other parameters of the optical systems have been presented. These parameters include:

$\beta_i$ , the total intrinsic birefringence of the sensing fiber;

$\beta_b$ , the total bend-induced birefringence of the sensing fiber;

$\beta_T$ , the total twist-induced birefringence of the sensing fiber;

$\theta$ , the orientation of the input SOP;

$\phi_i$ , the initial orientation of the intrinsic birefringence with the  $x$ -axis;

$\phi_{in}$ , the phase delay between the  $y$  and  $x$  components of the input SOP.

An ideal measurement requires no birefringences and linear input SOP which means that these six parameters are all zero. The total magnetic field induced circular birefringence in our experiment is

$$\beta_H = \oint \delta_H dl = 2VN_i N_f i = -0.065 \text{ rad} / \text{A} \times i \quad (3-15)$$

where  $V = -0.6 \times 10^{-6}$  rad/A is the Verdet constant of the silica [1, 93],  $N_i$  is the wire turns of the current conductor.  $N_f$  is the wire turns of coiling sensing fiber.

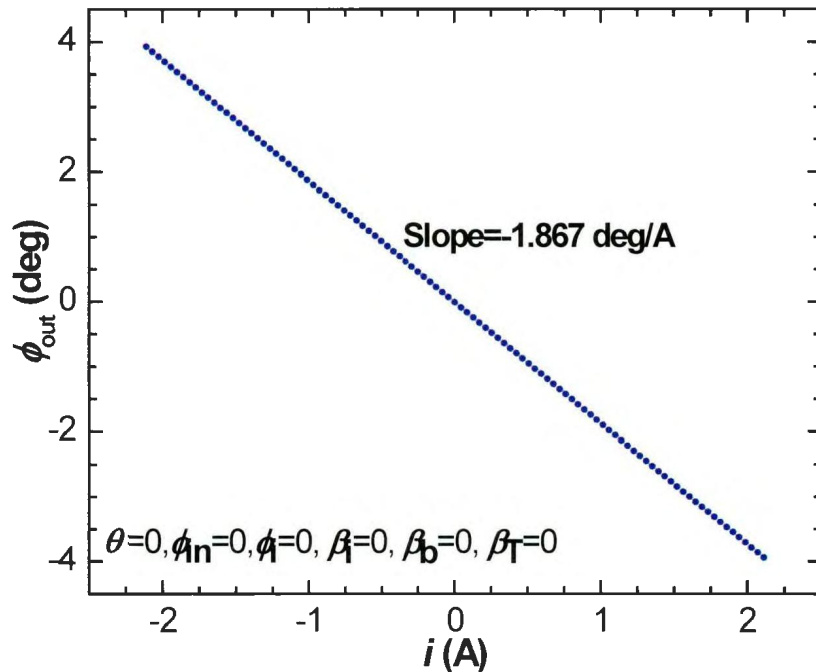


Figure 3-5 Ideal relationship between  $\phi_{out}$  and electrical current  $i$  at  $\theta = 0$ ,  $\phi_{in} = 0$ ,  $\phi_i = 0$ ,  $\beta_i = 0$ ,  $\beta_b = 0$ ,  $\beta_T = 0$

Thus, the relationship between  $\phi_{out}$  and electrical current  $i$  is simply expressed in Eqn. (1-6) at zero  $\beta_i, \beta_b, \beta_T, \theta, \phi_i, \phi_{in}$ . As illustrated in Figure 3-5, the current sensitivity is a constant of -1.862 deg/A at an arbitrary orientation of the input linear SOP. However, the nonzero  $\beta_i, \beta_b, \beta_T, \theta, \phi_i, \phi_{in}$  exist and will influence the measurement sensitivity of the basic scheme of the FOCS in practical applications [86, 87]. We will discuss these effects in the following subsections.

### 3.3.1 Dependence on intrinsic birefringence and the initial orientation of intrinsic birefringence

The sensing fiber deployed in our experiment is a single-mode fiber (SMF28-e). According to the specification of ITU-T G.652.D [94], the diameter of the fiber core should be  $10.4 \pm 0.5 \mu\text{m}$  at 1550 nm. The typical refractive-index difference between the core and cladding regions is  $\Delta n = 0.0036$  [95]. Thus, according to Eqns. (3-2) and (3-10) with fiber length  $L = 10.0 \text{ m}$ , the total maximum intrinsic birefringence of a SMF28-e fiber is

$$\beta_{i-\max} = \int_L \delta_{i-\max} dl = \delta_{i-\max} L \approx 0.2 \times \frac{2\pi}{1.55 \mu\text{m}} \left( \frac{10.9 \mu\text{m}}{9.9 \mu\text{m}} - 1 \right) (0.0036)^2 \times 10.0 \text{ m} = 10.6 \text{ rad}$$

Generally, the cross-sectional shape of a fiber core is not perfectly circular, in fact elliptical, due to manufacture process and uniform internal tension caused by cladding surface. The typical difference of the equatorial radius and polar radius of a single-mode fiber is 0.016%, also  $(a/b-1) \times 100\% = 0.016\%$  [96]. Thus, we derive

$$\beta_{i-\text{typical}} = 0.0168 \text{ rad}$$

After estimation of the total intrinsic birefringence in the sensing fiber, the dependence of the sensitivity on the intrinsic birefringence has been investigated at  $\beta_i = 0$ , 0.0168, 0.785, 1.57, 10.6 rad, as shown in Figure 3-6.

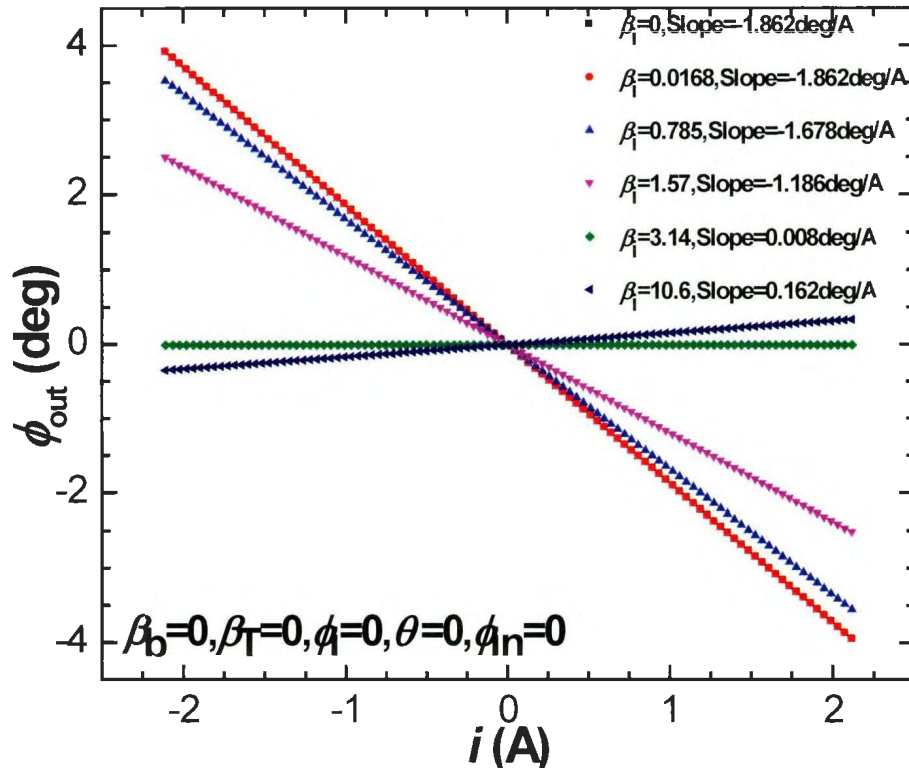


Figure 3-6 Relationship between  $\phi_{out}$  and electrical current  $i$  at  $\beta_b = 0$ ,  $\beta_T = 0$ ,  $\phi_i = 0$ ,  $\theta = 0$ ,  $\phi_{in} = 0$

The relationship between  $\phi_{out}$  and electrical current  $i$  in Figure 3-6 (the curve at  $\beta_i = 0$  has been overshadowed by the curve at  $\beta_i = 0.0168$ ) indicates that the magnitude of sensitivity will significantly decrease when the total intrinsic birefringence of the sensing fiber increases from 0.785 rad to 10.6 rad. However, the sensitivity remains almost the same as the sensitivity at  $\beta_i = 0$  when the existing intrinsic birefringence is small, for

example  $\beta_{i\text{-typical}} = 0.0168$  rad in our experiment. This result indicates that it is feasible to achieve reliable sensitivity while using a short length of sensing fiber with low intrinsic birefringence.

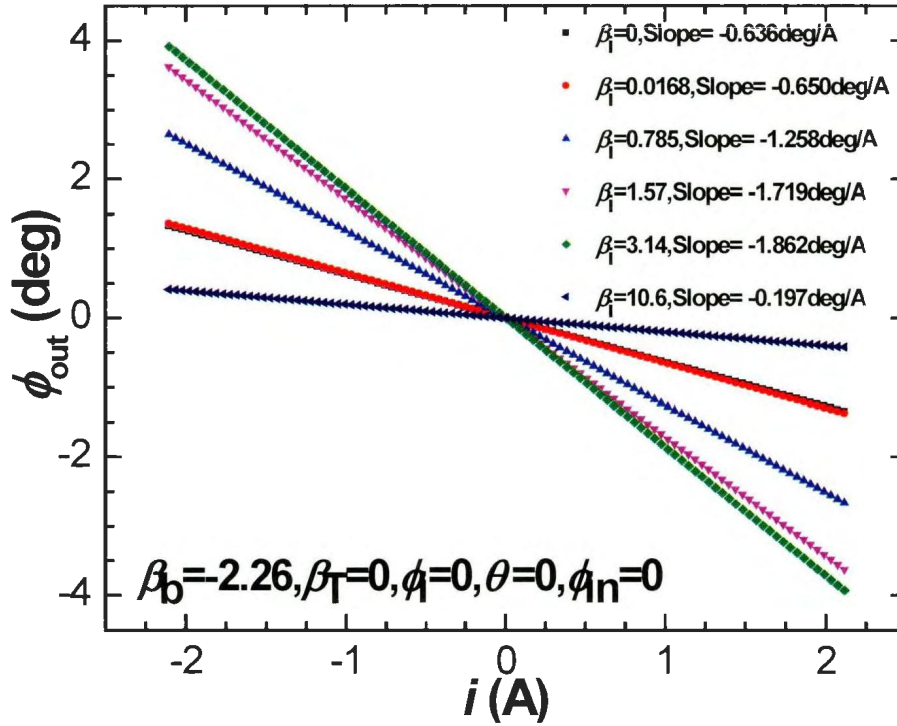


Figure 3-7 Relationship between  $\phi_{\text{out}}$  and electrical current  $i$  at  $\beta_b = -2.26$ ,  $\beta_T = 0$ ,  $\phi_1 = 0$ ,  $\theta = 0$ ,  $\phi_n = 0$

From Figure 3-7, in which the curve at  $\beta_i = 0$  has been overshadowed by the curve at  $\beta_i = 0.0168$ , the intrinsic birefringence might increase the sensitivity in addition to the existing bend-induced birefringence ( $\beta_b = -2.26$  rad is derived at a typical bending radius  $R = 3.0$  m). From Eqn. (3-11), we have

$$\Omega = \{[\beta_i \cos(2\phi_i + 2TL) + \beta_b]^2 + [\beta_i \sin(2\phi_i + 2TL)]^2 + (\beta_T + \beta_H)^2\}^{1/2} \cdot \frac{\beta_T + \beta_H}{|\beta_i + \beta_H|} \quad (3-16)$$

and

$$\tan \gamma = \{[\beta_i \cos(2\phi_i + 2TL) + \beta_b]^2 + [\beta_i \sin(2\phi_i + 2TL)]^2\}^{1/2} / (\beta_T + \beta_H). \quad (3-17)$$

When  $\beta_i \neq 0$ ,  $\beta_b \neq 0$ ,  $\beta_T = 0$ , the maximum magnitude of sensitivity can be achieved at large  $\Omega$  and small  $\gamma$  from Figure 3-3 (c), this requires:

$$[\beta_i \cos(2\phi_i + 2TL) + \beta_b]^2 + [\beta_i \sin(2\phi_i + 2TL)]^2 = 0. \quad (3-18)$$

Thus, considering that  $\beta_i$  and  $\beta_b$  have opposite signs, it requires

$$2\phi_i + 2TL = 2n\pi \quad (3-19a)$$

because when  $\beta_T$  is 0,  $T = 0$ , that is,

$$2\phi_i = 2n\pi \quad (3-19b)$$

where,

$$n = 0, 1, 2, 3, \dots$$

Therefore, from Eqn. (3-18), the maximum magnitude of sensitivity reaches at

$$|\beta_i + \beta_b| = 0. \quad (3-20)$$

When both of the intrinsic birefringence and the bend-induced birefringence exist, the sensitivity will be possible to achieve the maximum value (-1.862 deg/A from our experimental setup) which equals the value of sensitivity at zero  $\beta_i$ ,  $\beta_b$ ,  $\beta_T$ ,  $\theta$ ,  $\phi_i$ ,  $\phi_{in}$ . This result indicates that maximum sensitivity could be possibly achieved by adjusting appropriate amount of intrinsic birefringence and the initial orientation of the intrinsic birefringence to compensate the bend-induced birefringence in some sensing fibers.

However, in practical applications, the amount of bend-induced birefringence is generally one to two orders larger than the amount of intrinsic birefringence. As a result, the approach discussed here will not be applicable in improving the sensitivity degraded by the intrinsic birefringence or bend-induced birefringence.

For a given intrinsic birefringence  $\beta_i$ -typical = 0.0168 rad, the dependence of the sensitivity on the initial orientation of the intrinsic birefringence can be studied at this stage.

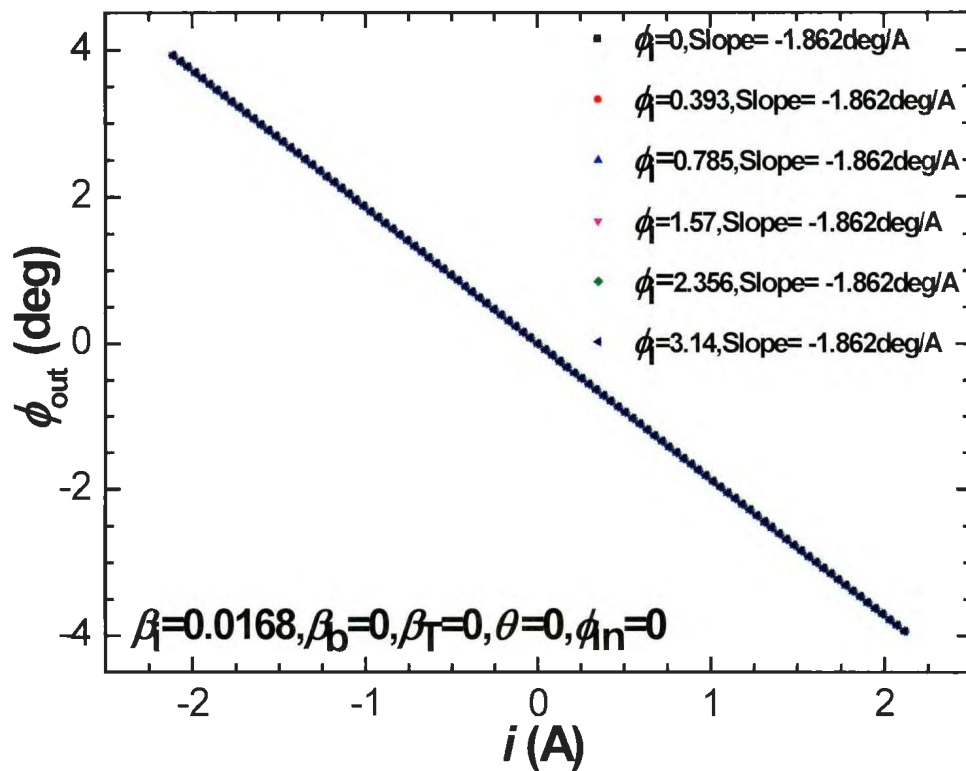


Figure 3-8 Relationship between  $\phi_{out}$  and electrical current  $i$  at  $\beta_i = 0.0168$ ,  $\beta_b = 0$ ,  $\beta_T = 0$ ,  $\theta = 0$ ,  $\phi_{in} = 0$

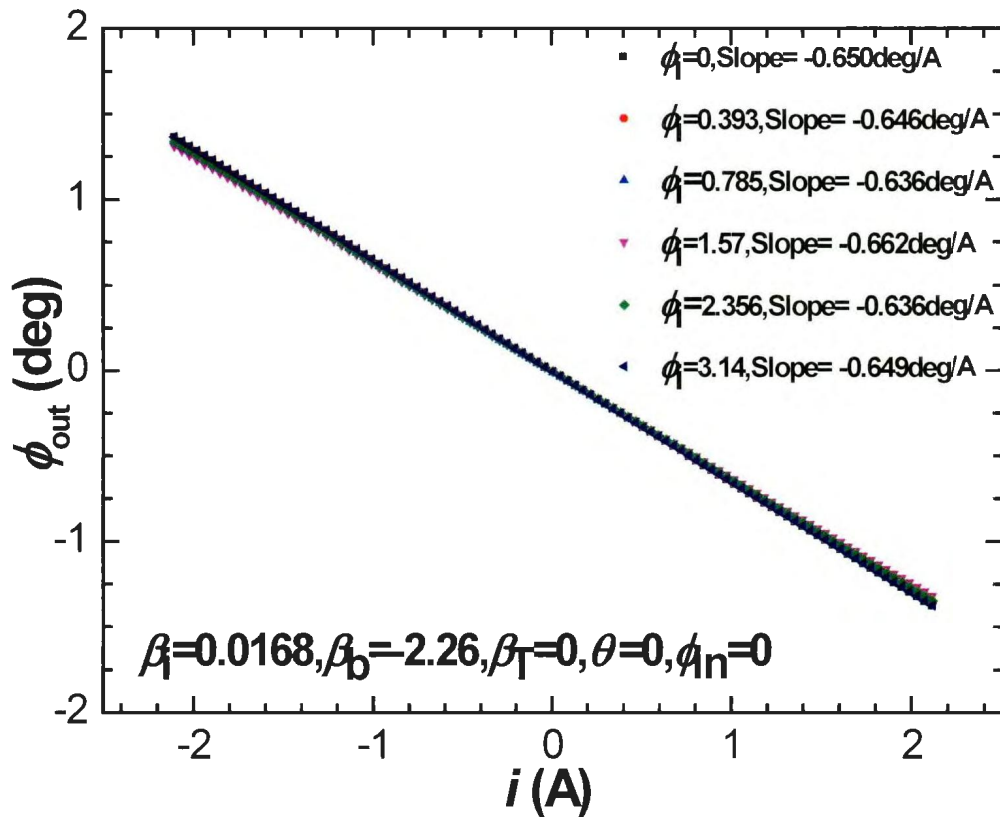


Figure 3-9 Relationship between  $\phi_{out}$  and electrical current  $i$  at  $\beta_1 = 0.0168$ ,  $\beta_b = -2.26$ ,  $\beta_T = 0$ ,  $\theta = 0$ ,  $\phi_{in} = 0$

From Figure 3-8 (the other curves have been overshadowed by the curve at  $\phi_1 = 3.14$ ), the current sensitivity is independent on the initial orientation of the intrinsic birefringence when the intrinsic birefringence is very small. However, the sensitivity slightly changes with the variation of initial orientation of the intrinsic birefringence while the intrinsic birefringence becomes larger. In our experiments, we ignore the effect of the initial orientation of the intrinsic birefringence as the existing intrinsic birefringence is very small.

### 3.3.2 Dependence on bend-induced birefringence

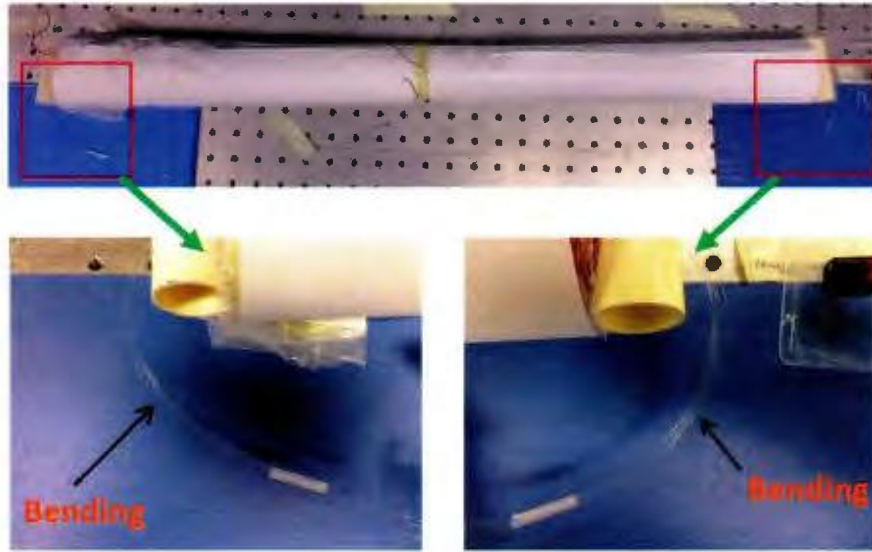


Figure 3-10 Bending of the sensing fiber in the experimental setup

When the sensing fiber coils are circulated around the current conductors, fiber bends will be inevitably introduced, as shown in Figure 3-10. The fiber bends will generate some amount of bend-induced birefringence in the sensing fiber.

According to Eqns. (3-3) and (3-10),

$$\beta_b = \int_L \delta_b dl = \delta_b L_{bend} = 0.25 \times \frac{2\pi}{1.55 \mu m} \times 1.46^3 \times (-0.15)(1+0.17) \frac{(62.5 \mu m)^2}{R^2} \times (10\pi R)$$

$$= -\frac{0.0679 \text{ rad} \cdot m}{R}$$

When  $R = 2.0, 3.0, 4.0, 5.0, 6.0, 10.0$  cm, the resultant  $\beta_b = -3.395, -2.263, -1.698, -1.358, -1.132,$  and  $-0.679$  rad, respectively. After this estimation, the dependence of the sensitivity on the bend-induced birefringence has been studied in the range  $\beta_b = 0 \sim$

-3.395 rad, shown in Figure 3-11 (the curve at  $\beta_b = 0$  has been overshadowed by the curve at  $\beta_b = -0.0168$ ).

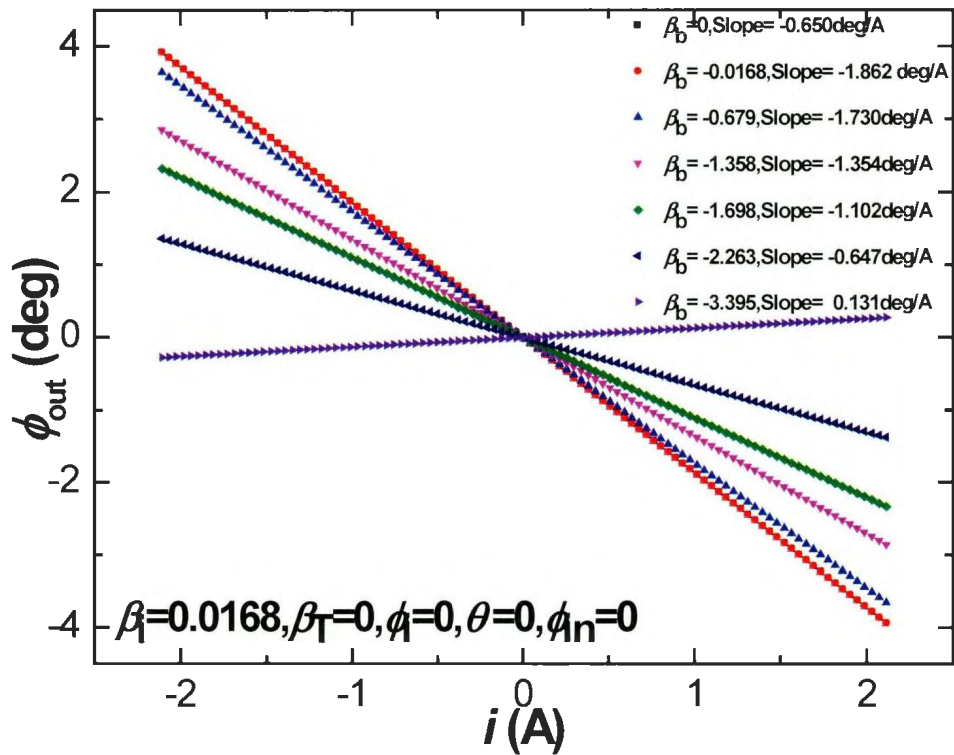


Figure 3-11 Relationship between  $\phi_{out}$  and electrical current  $i$  at  $\beta_i = 0.0168$ ,  $\beta_T = 0$ ,  $\phi_i = 0$ ,  $\theta = 0$ ,  $\phi_{in} = 0$

From Figure 3-11, the relationship between  $\phi_{out}$  and electrical current  $i$  indicates that the magnitude of sensitivity will significantly decrease when the total bend-induced birefringence of the sensing fiber decreases from -0.679 to -3.40 rad. However, the sensitivity remains almost the same as the sensitivity at  $\beta_b = 0$  when the existing bend-induced birefringence is small or the amount of bend-induced birefringence can compensate the intrinsic birefringence of the sensing fiber. Considering the factors that

the total typical intrinsic birefringence of a single-mode fiber is 0.0168 rad, and bending-induced birefringence is hard to achieve a small value close to -0.0168 rad, it seems not feasible to achieve a higher sensitivity by making compensation between the total intrinsic birefringence and the bending-induced birefringence.

### 3.3.3 Dependence on twist-induced birefringence

The effects of the twist-induced birefringence on the sensitivity are further investigated.

From Figure 3-12, the relationship between  $\phi_{out}$  and electrical current  $i$  indicates that the magnitude of sensitivity will significantly increase when the total twist-induced birefringence of the sensing fiber increases from 0 to 36.69 rad which corresponds to 0 to 4 number of twist turns per meter for a sensing fiber. When  $\beta_T$  approaches 18.35 rad, the magnitude of sensitivity reaches 1.833 deg/ A with a “bias” angle in  $\phi_{out}$ , which is very close to the maximum magnitude of current sensitivity 1.862 deg/A in this series of experiments [97]. However, when  $\beta_T$  approaches to combination of  $\beta_i$  and  $\beta_b$ , the linearity of the relationship between  $\phi_{out}$  and electrical current  $i$  is almost lost as shown by the curve at  $\beta_T = 2.29$  in Figure 3-12. There is a 180° phase offset in  $\phi_{out}$  when  $\beta_T$  approaches to 9.17 rad. We will further discuss the nonlinearity that is caused by different amounts of twist-induced birefringence in Figure 3-13 at a larger current range.

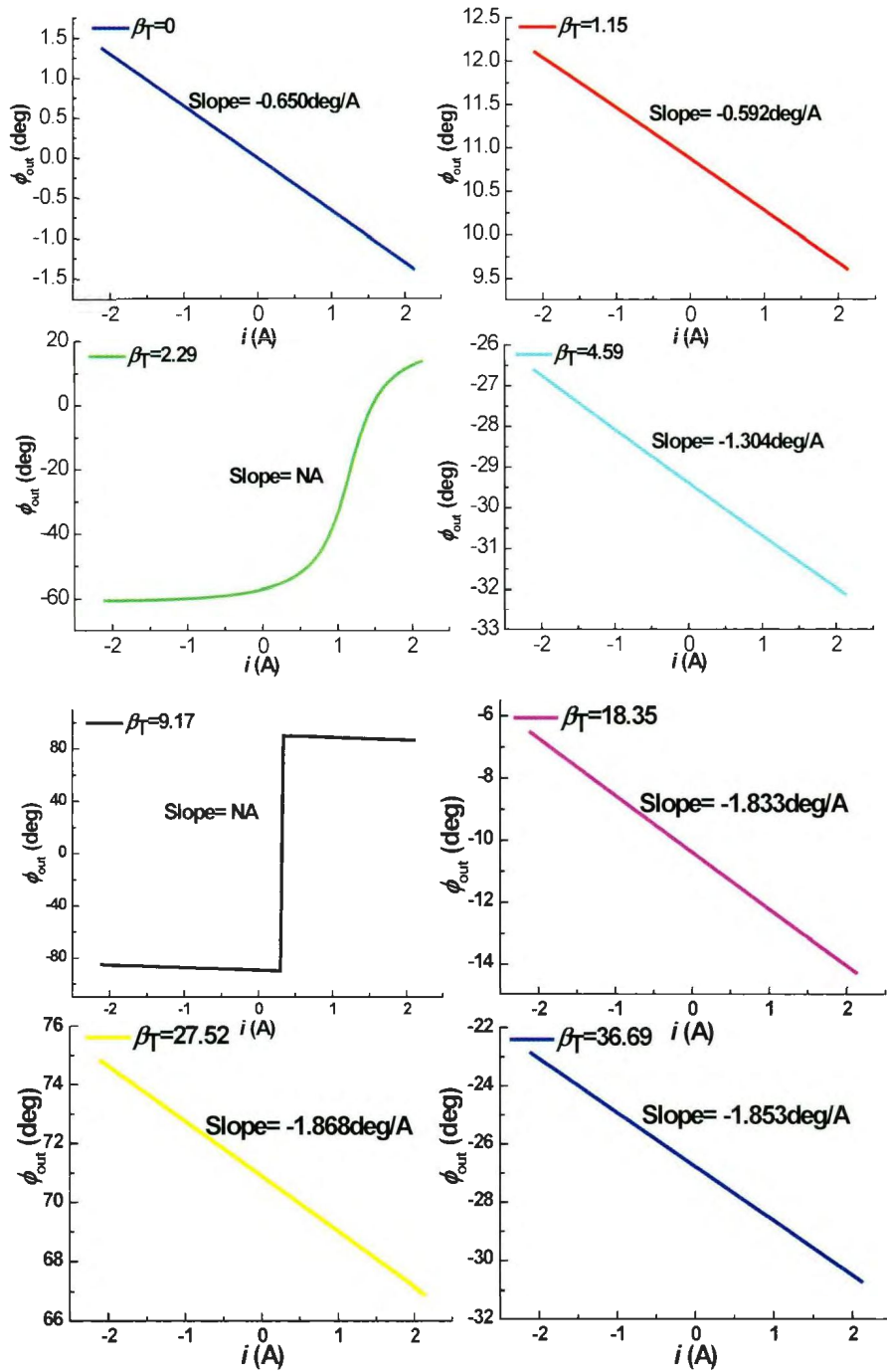


Figure 3-12 Relationship between  $\phi_{out}$  and electrical current  $i$  at  $\beta_i = 0.0168$ ,  $\beta_b = -2.26$ ,  $\phi_i = 0$ ,  $\theta = 0$ ,  $\phi_{in} = 0$

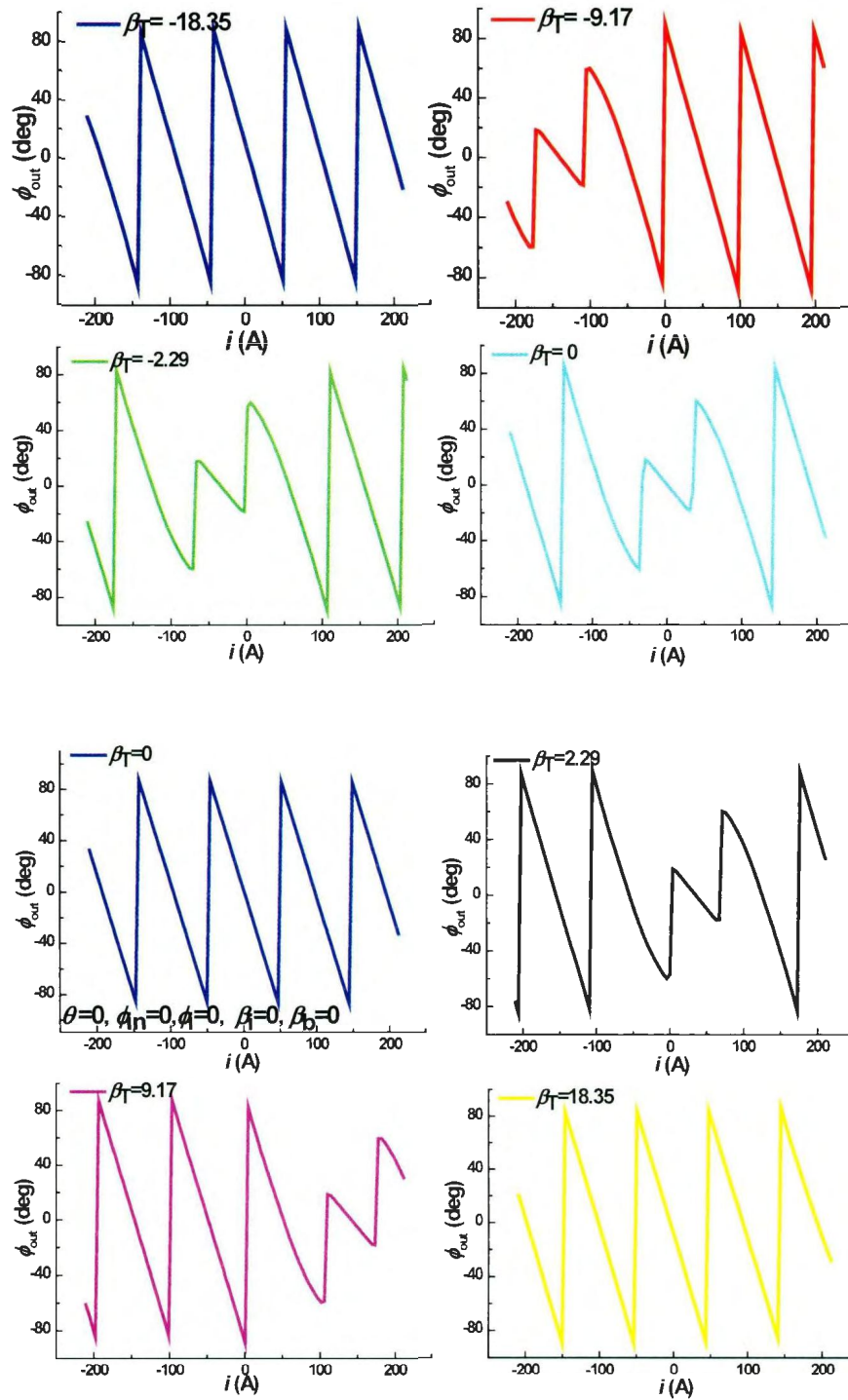


Figure 3-13 Relationship between  $\phi_{out}$  and electrical current  $i$  at a large current range with  $\beta_i = 0.0168, \beta_b = -2.26, \phi_i = 0, \theta = 0, \phi_{in} = 0$

The result in Figure 3-13 illustrates that: (1) there is always a segment of lower sensitive and nonlinear curve in the sensing curve when the total intrinsic and bend-induced birefringence exist by comparing middle curve at  $\beta_T = 0$  with others; (2) an applied twist-induced birefringence shifts the nonlinear sensing curve from around 0 A range to other current range; negative twist-induced birefringence shifts the nonlinear sensing curve towards negative current range (shown in the curve at  $\beta_T = -9.17$  in Figure 3-13), and positive twist-induced birefringence shifts the nonlinear sensing curve towards positive current range (shown in the curve at  $\beta_T = 9.17$  in Figure 3-13); (3) When a larger twist-induced birefringence is applied, the larger shift of the sensing curve will result.

This result indicates that the decreased magnitude of sensitivity and nonlinear sensing curve due to intrinsic and bend-induced birefringence can be compensated and significantly improved to the maximum magnitude of sensitivity with good linearity at small measuring current range by introducing an appropriate amount of twist-induced birefringence [98]. Meanwhile, high sensitivity with good linearity can be achieved without any twist-induced birefringence at large measuring current range.

#### **3.3.4 Dependence on initial input state of polarization**

After the compensation of the intrinsic and bend-induced birefringence with twist-induced birefringence, we study the dependence of the current sensitivity on initial SOP. There are three types of input SOP: linear input SOP, elliptical input SOP, and circular input SOP.

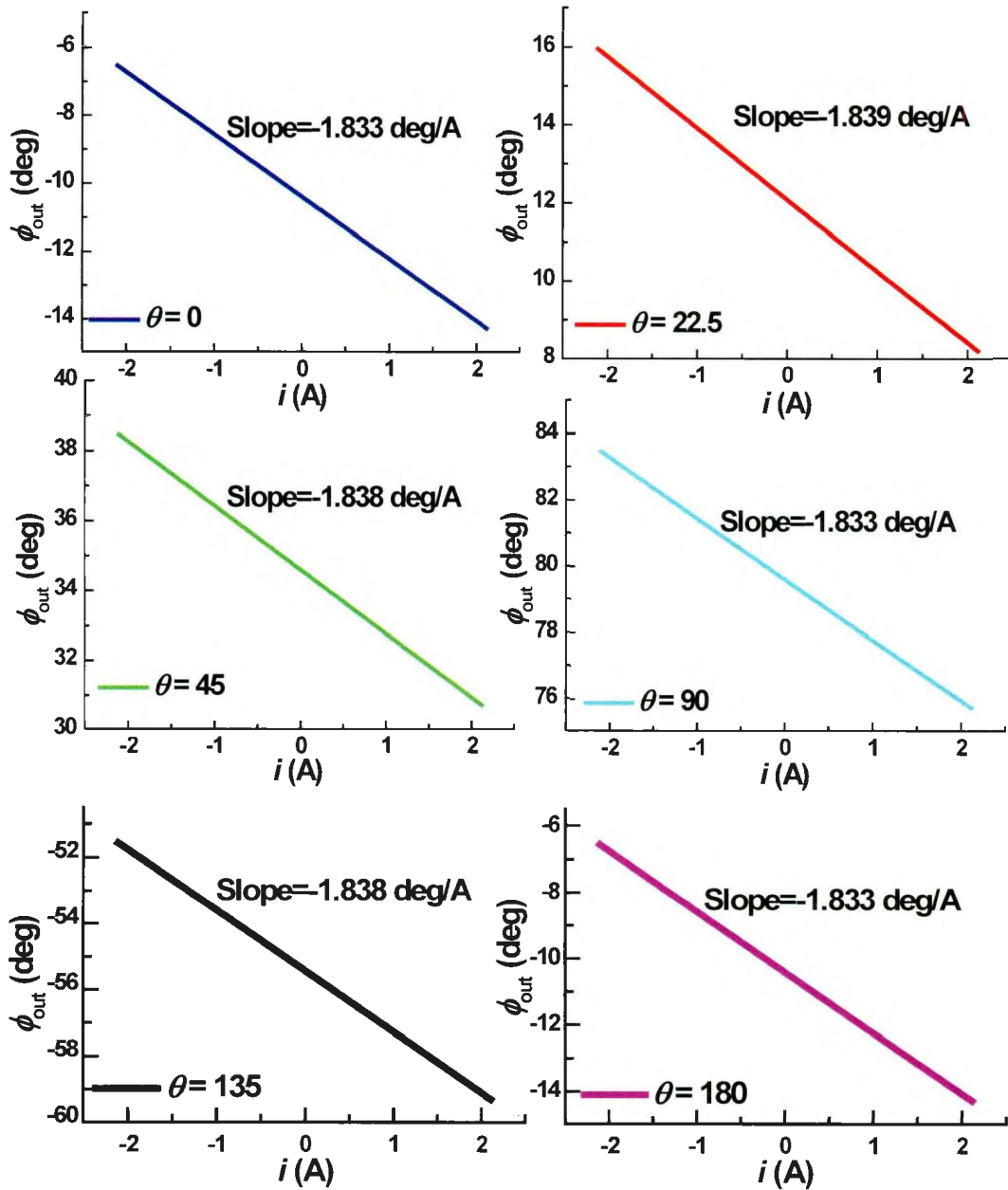


Figure 3-14 Relationship between  $\phi_{out}$  and electrical current  $i$  at different linear input SOPs at  $\beta_i = 0.0168$ ,  $\beta_b = -2.26$ ,  $\beta_T = 9.17$ ,  $\phi_i = 0$ ,  $\phi_{in} = 0$

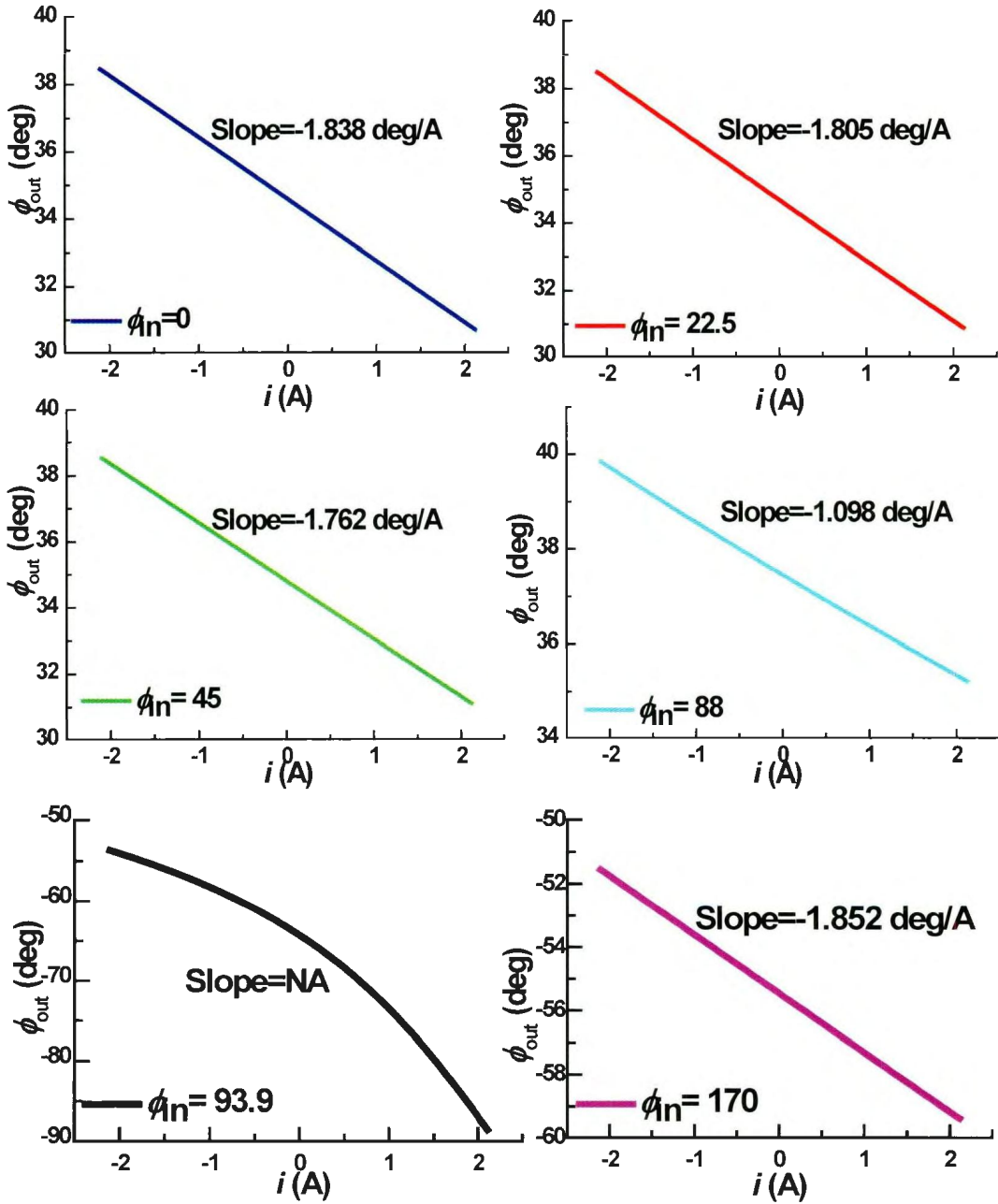


Figure 3-15 Relationship between  $\phi_{out}$  and electrical current  $i$  at different elliptical input SOPs at  $\beta_i = 0.0168$ ,  $\beta_b = -2.26$ ,  $\beta_T = 18.35$ ,  $\phi_i = 0$ ,  $\theta = 45$

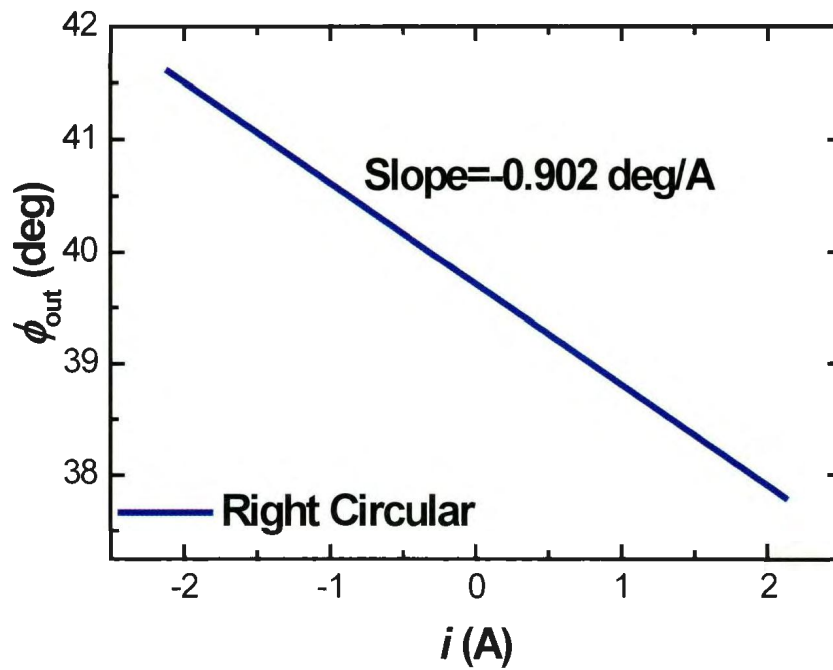
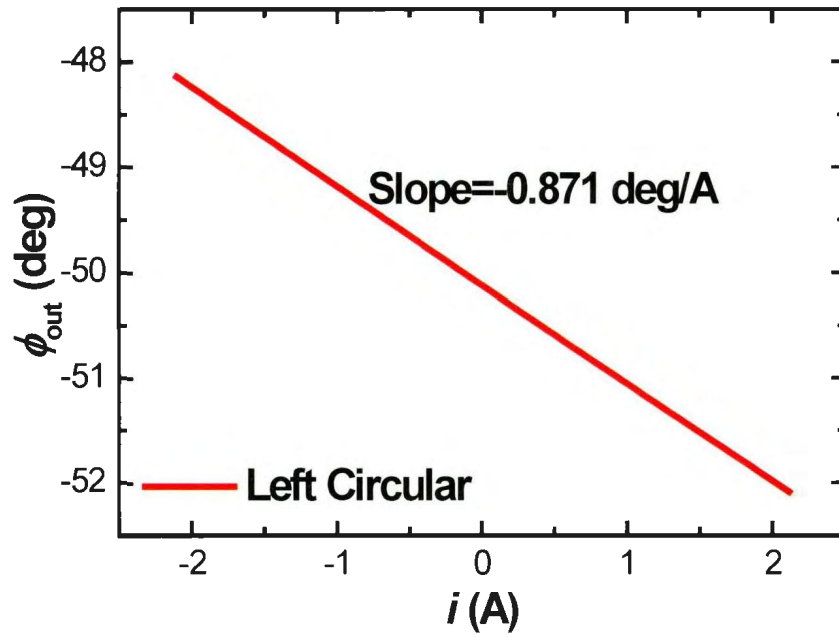


Figure 3-16 Relationship between  $\phi_{out}$  and electrical current  $i$  at circular input SOP at  $\beta_i = 0.0168$ ,  $\beta_b = -2.26$ ,  $\beta_T = 18.35$ ,  $\phi_i = 0$ ,  $\phi_{in} = 90$

From Figure 3-14, the sensitivities remain constant only with a bias in angle in the  $\phi_{out}$  when the initial input SOP is linearly polarized with an arbitrary input orientation. From Figure 3-15, the magnitude of sensitivities reduces or the measurement linearity is destroyed when the input SOP degrades to an elliptical polarization, especially the input SOP approaches to a circular polarization. From Figure 3-16, the magnitude of sensitivities decreases when the initial input SOP evolves into a completely circular SOP. These results demonstrate that neither the elliptical nor circular input SOP is allowable to achieve a higher sensitivity with good linearity.

These conclusions can be further examined at a larger current range.

The results in Figure 3-17 illustrate that: (1) different orientations of linear input SOP only shift the sensing curve along current axis without any influence on the sensitivity or the linearity of the sensing curve by comparing the middle curve at  $\phi_n=0, \theta=0$  and the middle curve at  $\phi_n=0, \theta=45$ ; (2) circular input SOP decreases the sensitivity in whole current range, which is demonstrated by the curve at  $\phi_n=90$ ; (3) elliptical input SOP degrades the sensitivity and the linearity of the sensing curve in the whole current range, illustrated by other five curves. Particularly, this influence will be much more apparent when the elliptical input SOP approaches a circular SOP, shown in the top left and the low left curves in Figure 3-17.

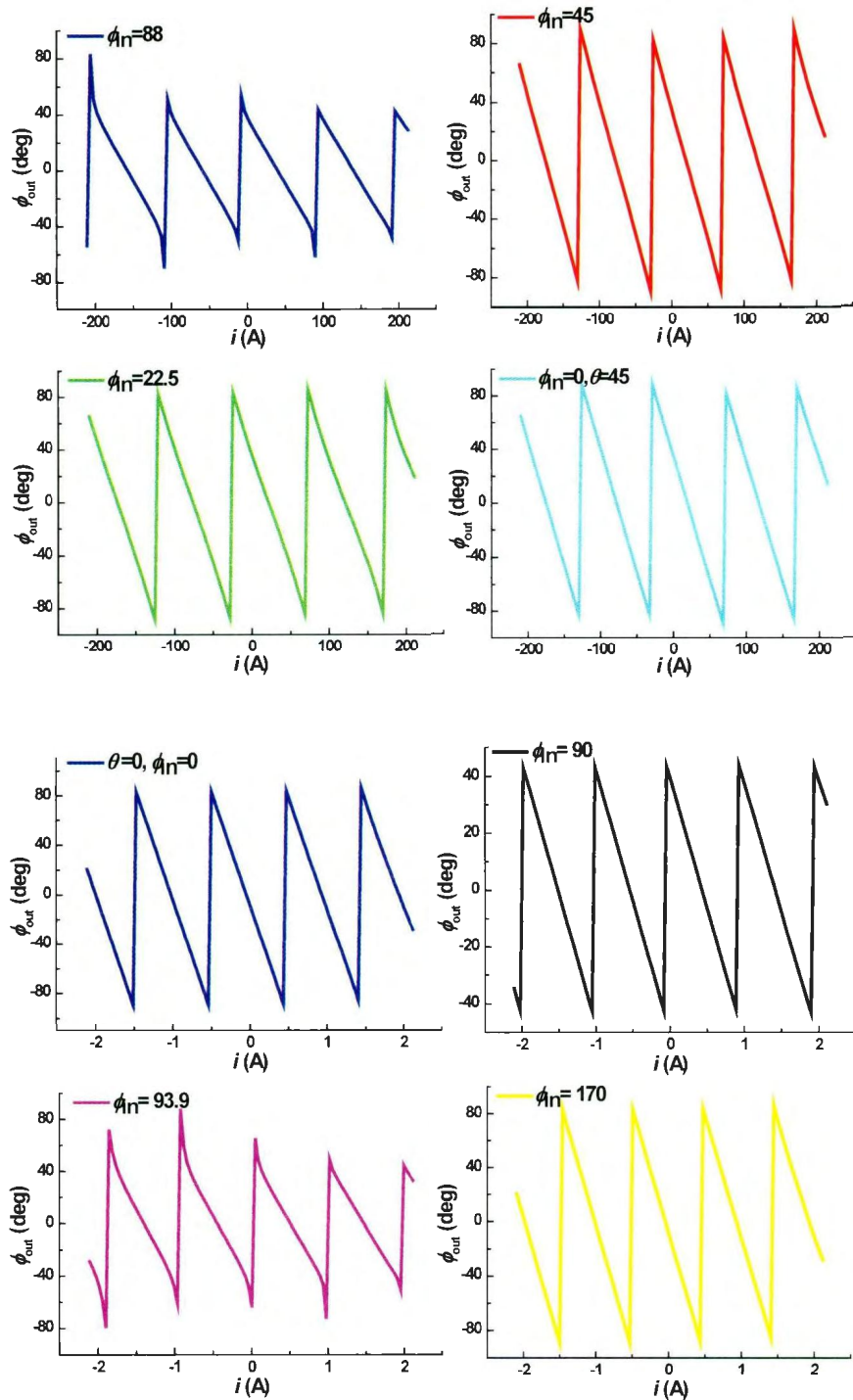
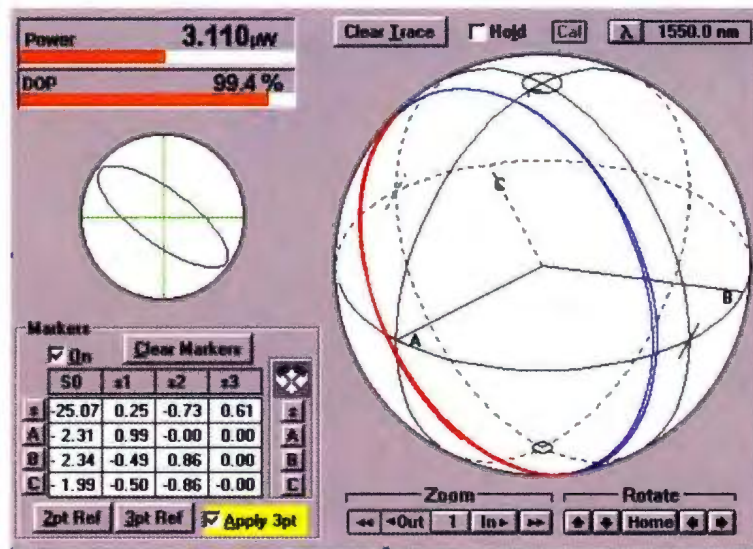


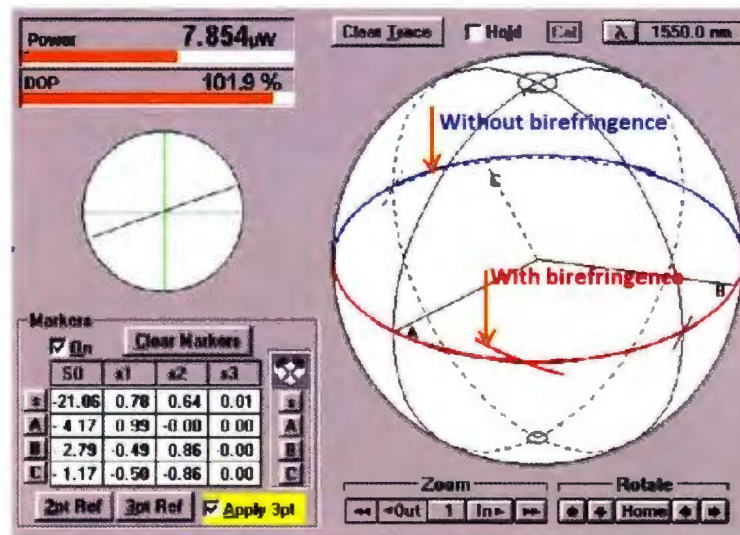
Figure 3-17 Relationship between  $\phi_{out}$  and electrical current  $i$  at large current range with  $\beta_i = 0.0168$ ,  $\beta_b = -2.26$ ,  $\beta_T = 18.35$ .  $\phi_i = 0$ ,  $\theta = 45$

### 3.4 Dependence of sensitivity on parameters: experimental perspective

The following series of experiments investigate the dependence of sensitivity on bend-induced, twist-induced birefringence and the initial input SOP.



(a)



(b)

Figure 3-18 Evidence of existing birefringence: (a) output elliptical polarization; (b) Faraday rotation orbit is out of equatorial plane

From observed output SOP in our experiment, the recorded orbit of elliptical SOP out of the equatorial plane in Figure 3-18(a) demonstrates that there should be existing linear, because the orbit should lie in the equatorial plane for linear input SOP if there is no linear birefringence. Furthermore, Figure 3-18(b) indicates that the existing birefringence has shifted the rotation orbit with a small angle with the equatorial plane, decreasing the sensitivity with a factor of a cosine function according to Eqn. (3-11).

### **3.4.1 Dependence on bend-induced birefringence**

The various amounts of bend-induced birefringence can be realized by alternating the bending diameters of the sensing fiber. The value of  $\beta_b$  was calculated to be -1.14, -1.36, -1.70, -2.26, or -3.40 rad when the bending diameter  $R$  equals 6, 5, 4, 3, or 2 cm, respectively. The experimental result in Figure 3-19 illustrates that the magnitude of sensitivity decreases from 1.90 to 0.24 deg/A when the magnitude of the bend-induced birefringence increases from 1.14 to 3.40 rad, which agrees with the simulation result in Figure 3-11.

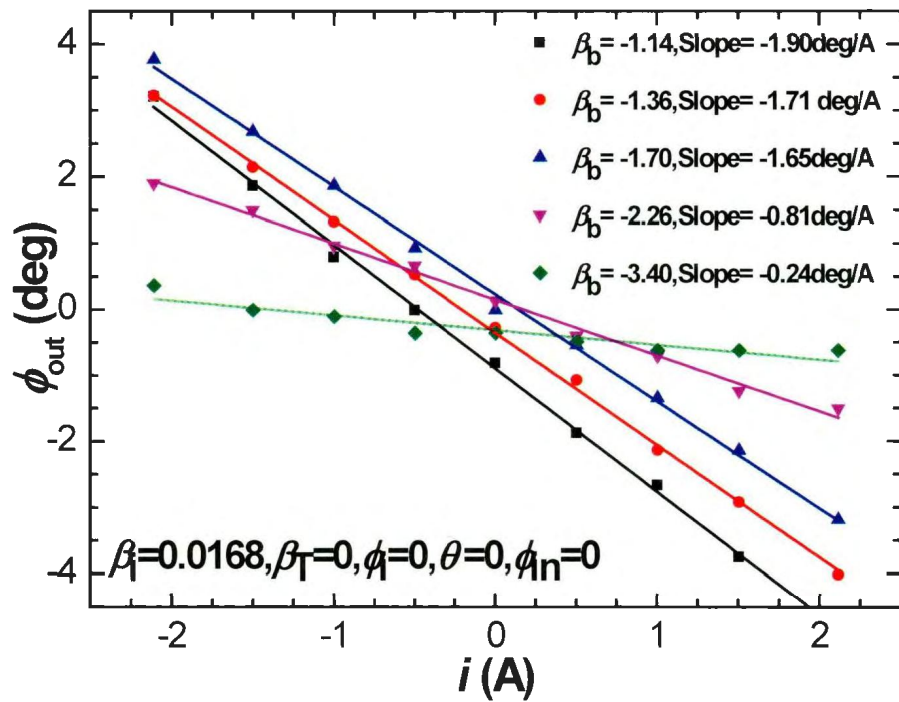


Figure 3-19 Dependence of sensitivity on bend-induced birefringence

### 3.4.2 Dependence on twist-induced birefringence

Twist-induced birefringence is easily achieved by twisting the sensing fiber at certain angle. From the experimental result in Figure 3-20 the magnitude of sensitivity increases from 0.80 to 1.88 deg/A when the twist-induced birefringence increases from 1.83 rad to 18.35 rad. This result is consistent with the conclusion obtained in Figure 3-12.

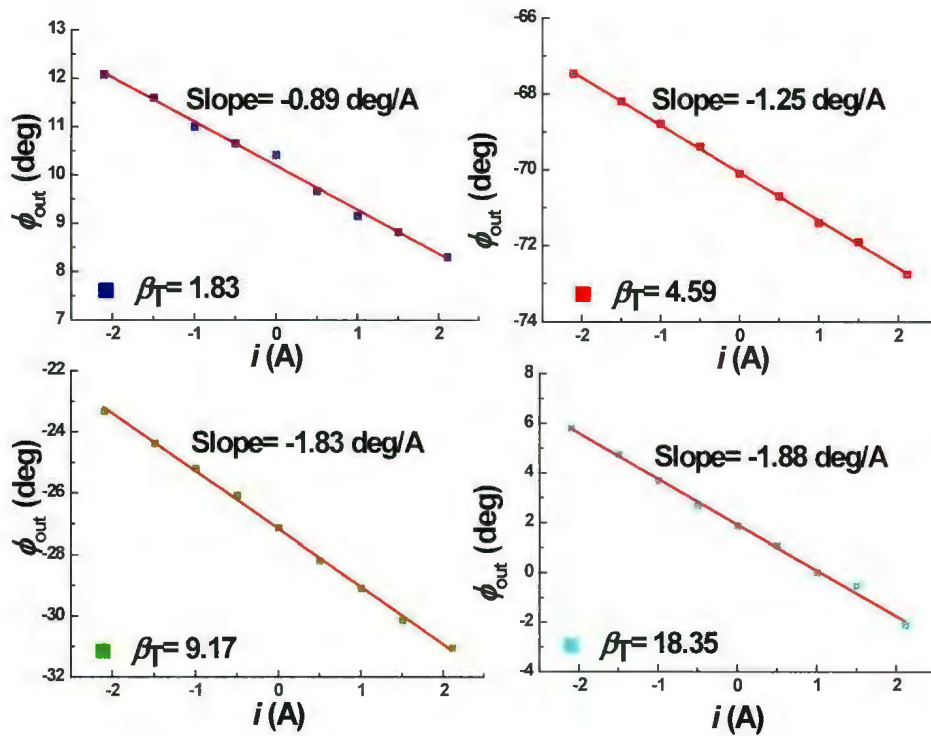


Figure 3-20 Dependence of sensitivity on twist-induced birefringence at  $\beta_i = 0.0168$ ,  $\beta_b = -2.26$ ,  $\theta = 45$ ,  $\phi_i = 0$ ,  $\phi_n = 0$

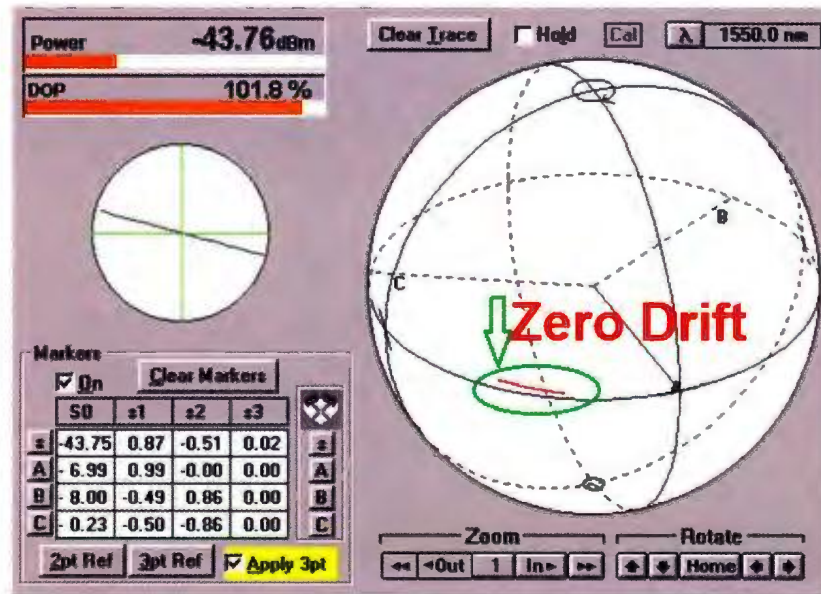


Figure 3-21 Recorded zero drift in FOCS at  $\beta_T = 36.69$  rad

Though sufficient amount of twist-induced birefringence can compensate the lower sensitivity and nonlinearity caused by intrinsic and bend-induced birefringence, excessive amount of twist-induced birefringence could result in zero drift, shown in Figure 3-21. The output SOP has significantly changed during 10 minutes of laboratory observation during the experiment. This zero drift is due to the tension release and slippage between the cladding and coating in sensing fiber [99]. Repeated experiments showed that a maximum sensitivity and an excellent linearity of sensing curve can be maintained when the amount of applied twist-induced birefringence is about 5~10 times larger than the amount of total intrinsic and bend-induced birefringence. In practical application, there is a trade-off between the sensitivity and the flow drift according to the requirements of a FOCS.

### **3.4.3 Dependence on initial input state of polarization**

The initial input SOP can be managed and monitored by a polarization controller (HP HEWLETT 11896A) and the polarization analyzer (Agilent 8509C). Experimental results in Figure 3-22 indicate that the sensitivity remain unchanged under initial linear input SOP while either the sensitivity or the linearity is degraded under elliptical or circular input SOP. The curve labeled with circular input SOP shows a bad linearity because it is not a perfect circular input SOP in experiment. In fact, it is an exact elliptical input SOP with the third Stokes parameter of 0.97~0.98 on Poincare Sphere of the input SOP in this curve. Therefore, the close circular input SOP induces a significant nonlinearity in the sensing curve according the conclusion in Figure 3-17.

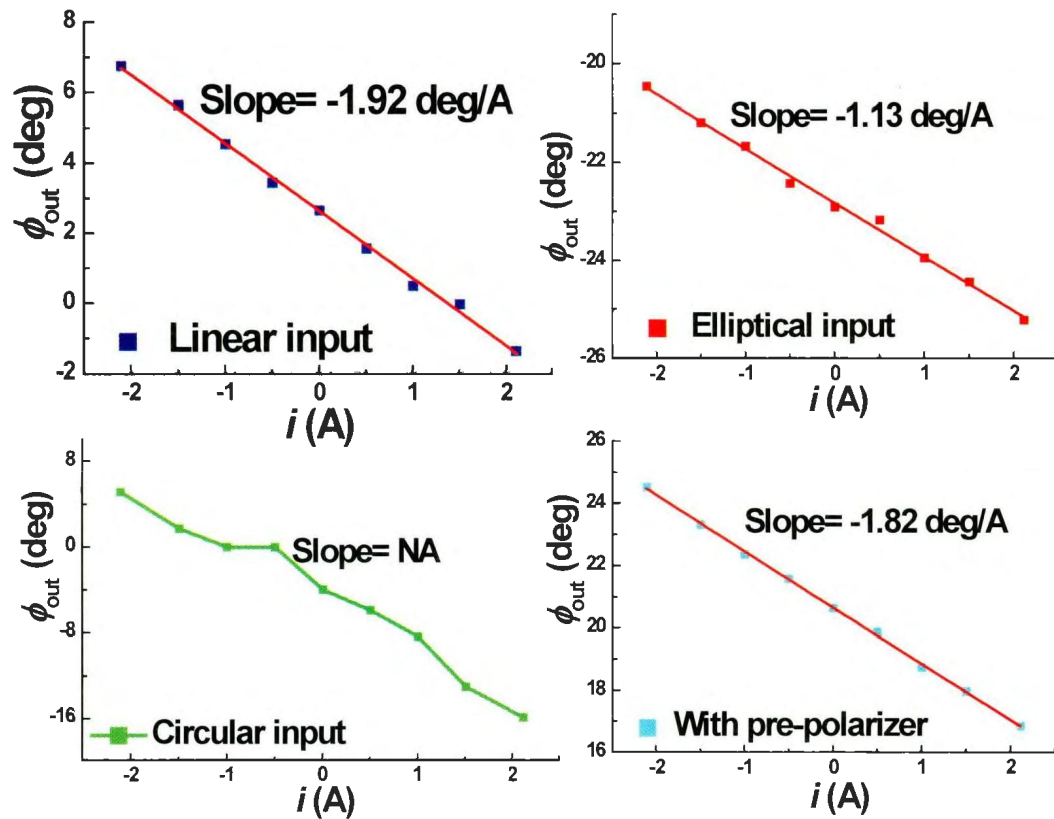


Figure 3-22 Dependence of sensitivity on initial input SOP at  $\beta_1 = 0.0168$ ,  $\beta_0 = -2.26$ ,  $\beta_1 = 9.17$ ,  $\phi_1 = 0$

In order to guarantee an ideal linearly polarized SOP before the light enters the sensing fiber, an inline pre-polarizer (shown in Figure 2-23) is employed to achieve this purpose, preventing degradation of the linear input SOP along the pigtail fiber before light reaches the sensing fiber. The bottom right figure in Figure 3-22 illustrates that the sensitivity and linearity have been greatly recovered from the negative effect of elliptical or circular input SOP.



Figure 3-23 A pre-polarizer is deployed to obtain an ideal initial linear input SOP

### **3.5 Basic experimental setup with intensity measurement**

#### **3.5.1 Experimental setup**

After the analysis of output SOP, the relationship between the intensity of the output light and the measuring current can be further studied by replacing the polarization analyzer in Figure 3-1 with an inline polarizer and a power meter (Newport 2832C), shown in Figure 3-24. This study is worthwhile and essential because the application of a portable power meter is much more convenient and easier than the application of a bulk and expensive polarization analyzer in industry.

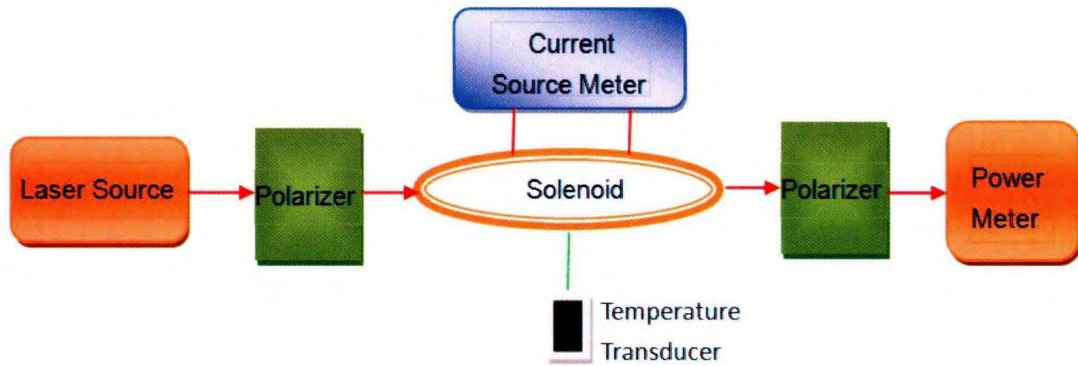


Figure 3-24 Basic scheme of FOCS with intensity measurement

The orientation of the second polarizer is placed at an angle  $\theta_p$  with the axis. Thus, according to the relationship in Eqn. (3-11), the SOP of the detected light and the corresponding intensity are derived as:

$$\begin{pmatrix} E_x \\ E_y \end{pmatrix}_{out} = \begin{pmatrix} \cos \theta_p & -\sin \theta_p \\ \sin \theta_p & \cos \theta_p \end{pmatrix} \begin{pmatrix} 1 & 0 \\ 0 & 0 \end{pmatrix} \begin{pmatrix} \cos \theta_p & \sin \theta_p \\ -\sin \theta_p & \cos \theta_p \end{pmatrix} \begin{pmatrix} A & -B \\ B & A^* \end{pmatrix} \begin{pmatrix} e^{i\phi_m} * \cos \theta \\ \sin \theta \end{pmatrix}_m \quad (3-21)$$

$$I_{out} = E_{out}^T \cdot E_{out}^* = \begin{pmatrix} E_x \\ E_y \end{pmatrix}_{out}^T \cdot \begin{pmatrix} E_x \\ E_y \end{pmatrix}_{out}^* \quad (3-22)$$

The first and the third rotation matrixes are added because the coordinates in the sensing and the second polarizer, also referred as detecting polarizer, form an angle  $\theta_p$  with the  $x$ -axis.  $I_{out}$  in Eqn. (3-22) is the light intensity detected by a power meter.

### 3.5.2 Dependence of sensitivity on parameters: simulation perspective

Having the relationship between  $I_{out}$  and the measuring current  $i$  expressed in Eqns. (3-11), (3-21) and (3-22), the dependence of sensitivity and linearity on the intrinsic,

bend-induced birefringence, the twist-induced birefringence, the orientation of input SOP  $\theta$ , and the orientation of output SOP  $\theta_p$  is further investigated at a large current range from -210.8 to 210.8 amperes which can clearly show several periods of sensing curves.

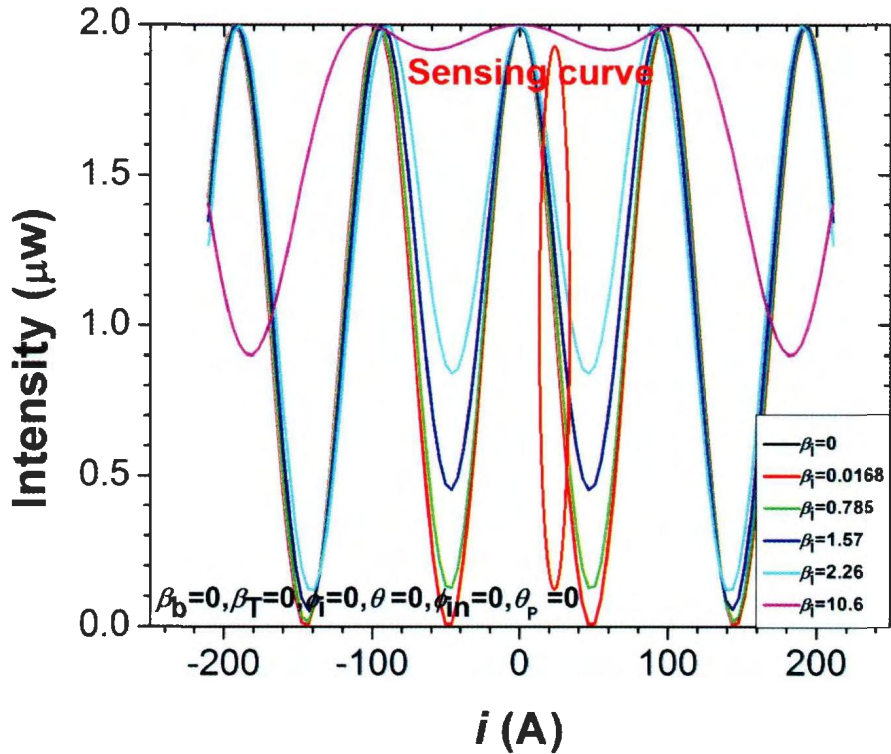


Figure 3-25 Relationship between  $I_{out}$  and current  $i$  at various intrinsic birefringence.

Since the resultant relationship between  $I_{out}$  and current  $i$  obeys a sine or cosine function, the middle segment of the resultant sine or cosine wave curve is generally employed as a sensing curve to achieve high sensitivity and good linearity, shown as the circled region in Figure 3-25 (the curve at  $\beta_i=0$  has been overshadowed by the curve at  $\beta_i=0.0168$ ) and Figure 3-26 (the curve at  $\beta_i=0$  has been overshadowed by the curve at  $\beta_i$

=0.0168). The results in Figure 3-25 and 3-26 demonstrate that the magnitude of sensitivities in lower current range (around  $\pm 25$  A and  $\pm 75$  A) has been significantly reduced by the large intrinsic or bend-induced linear birefringence while these influences are less in larger current range (around  $\pm 125$  A and  $\pm 175$  A). This finding indicates that higher sensitivity could be achieved in a larger current range when intrinsic and bend-induced birefringence exists.

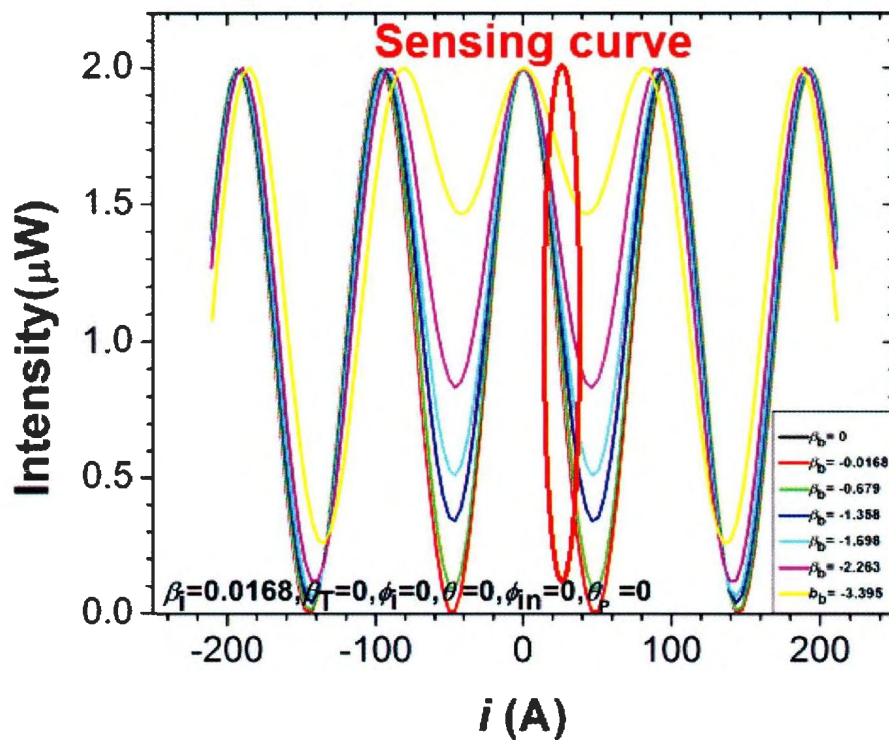


Figure 3-26 Relationship between  $I_{out}$  and current  $i$  at various bend-induced birefringence.

The results in Figure 3-27 illustrate that the twist-induced birefringence does not make significant change in the sensitivity or linearity of the sensing curve, but shifts the sensing curves towards larger current range, which results in a better sensitivity in lower

current range when intrinsic and bend-induced birefringence exists. In our experiment, the highest sensitivity can be achieved around zero ampere range when twist-birefringence approaches 10.90 rad, shown as the curve at  $\beta_T=10.90$  in Figure 3-27.

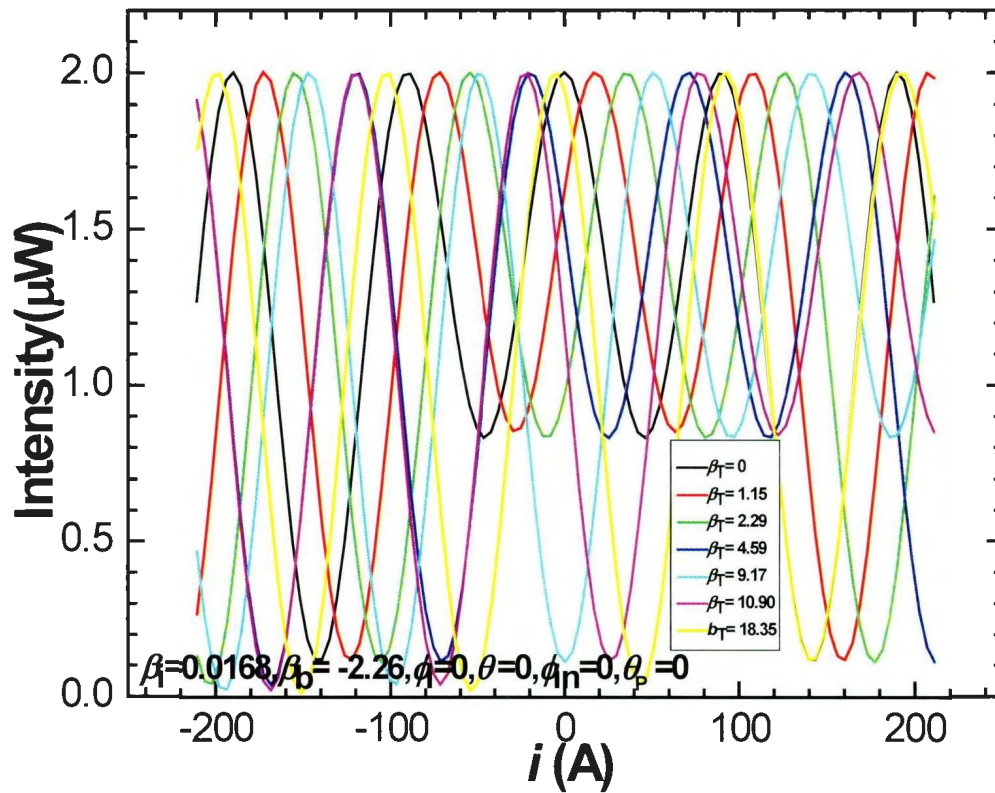


Figure 3-27 Relationship between  $I_{out}$  and current  $i$  at various twist-induced birefringence.

The simulation result in Figure 3-28 (the curve at  $\theta=0$  has been overshadowed by the curve at  $\theta=180$ ) explains that the initial orientation of linear input SOP has no effect on the sensitivity or linearity of the sensing curve. However, it shifts the sensing curves towards positive larger current range. For instance, the low sensitive curves caused by intrinsic and bend-induced birefringences have shifted to high current range, shown in

Figure 3-28. This finding indicates that the whole current range can be covered during the measurement at a high sensitivity by simply adjusting the initial orientation of linear input SOP.

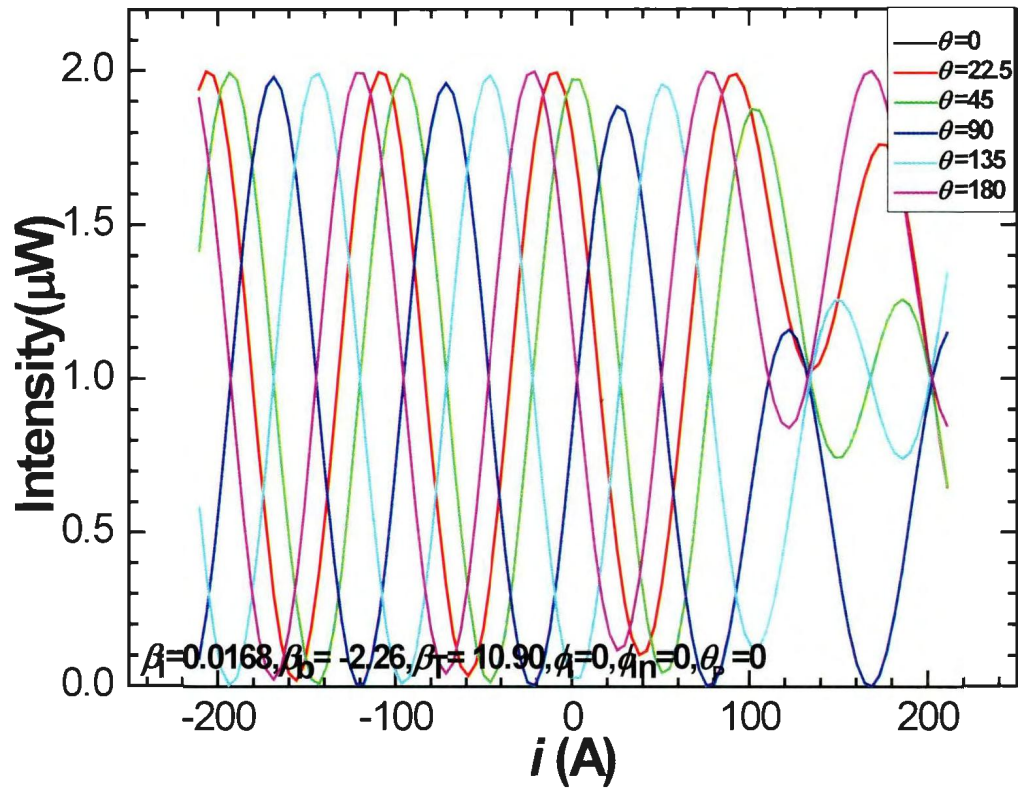


Figure 3-28 Relationship between  $I_{out}$  and current  $i$  at various orientations of initial linear input SOP.

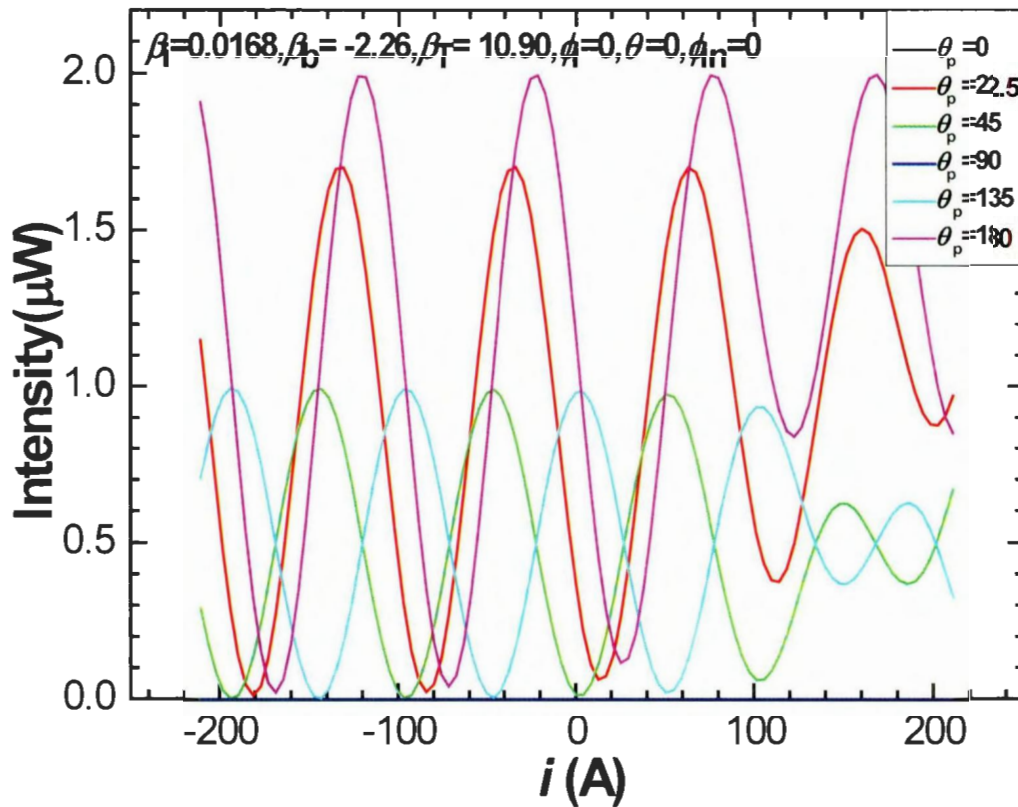


Figure 3-29 Relationship between  $I_{out}$  and current  $i$  at various orientations of detecting polarizer.

The orientation of the detecting polarizer certainly has no effect on the output SOP after the sensing fiber, but it definitely influences the SOP and the intensity that a power meter detects. Figure 3-29 (the curve at  $\theta_p = 0$  has been overshadowed by the curve at  $\theta_p = 180$ ) shows that the increasing orientation of the detecting polarizer not only degrades the sensitivity of the sensing curves but also shifts the sensing curves towards negative larger current range. In Figure 3-29, the maximum sensitivity reaches at zero orientation when other parameters have been set at  $\beta_i = 0.0168$ ,  $\beta_b = -2.26$ ,  $\beta_r = 9.17$ ,  $\phi = 0$ . After

adjusting the orientation of initial input SOP which can shift the curve waist of the sensing curve to the measuring current ranges, other current ranges can also be measured. Meanwhile, the orientation of the detecting polarizer usually needs to be adapted to 45° with the orientation of output SOP.

### **3.5.3 Dependence of sensitivity on parameters: experimental perspective**

The experimental setup established to detect the output light intensity is shown in Figure 3-30, including a detecting polarizer (F-ILP-2-N-SP-FA, Newport) and a power meter (2832-C, Newport). The orientation of the detecting polarizer is set in the horizontal direction marked by tape.

The detected light intensity is expressed as Malus law:

$$I_{out} = I_{in} \cos^2 \theta \quad (3-23)$$

where  $\theta$  is the angle between the orientation of the propagating light before the detecting polarizer and the orientation of the detecting polarizer.

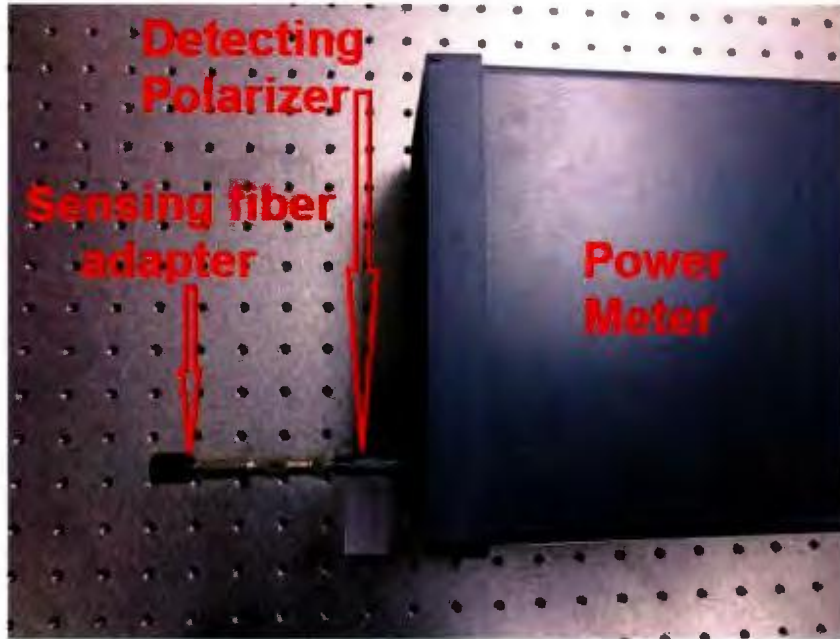


Figure 3-30 Experimental setup established to detect the output light intensity

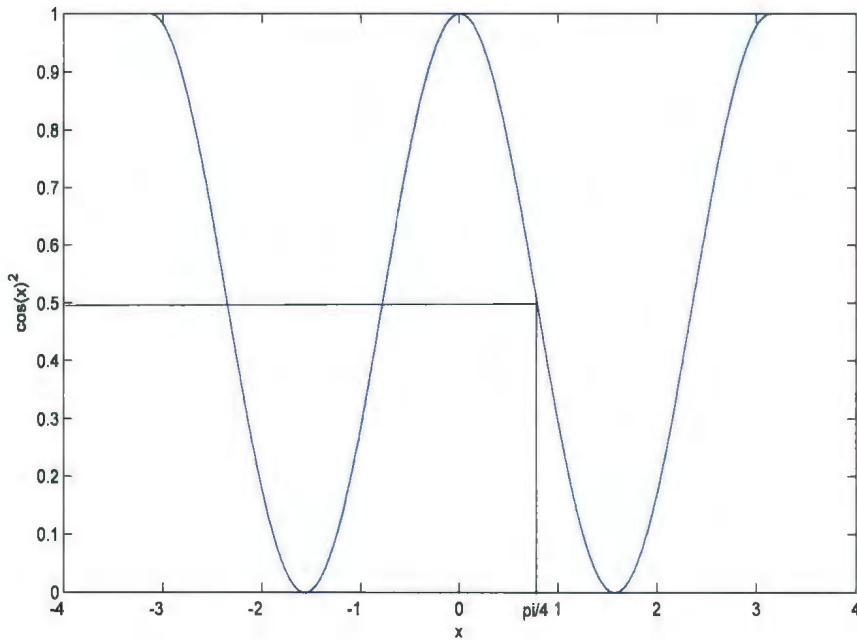


Figure 3-31 Relationship between  $\cos^2 x$  and  $x$

In fact, according to Malus's Law in Eqn. (3-23), the maximum sensitivity should be obtained at  $\theta = \pi/4$ , indicated in Figure 3-31, though we did not discuss it in Figures 3-25 to 3-27. This condition requires that the orientation of the SOP of the output light from the sensing fiber must form an angle of  $\theta$  ( $\theta = \pi/4$ ) with the orientation of the detecting polarizer when the highest sensitivity is achieved, as shown in the curve at  $\beta_T=10.90$  of Figure 3-27. Before the sensing adapter is connected to the detecting polarizer, the linear output SOP after the sensing fiber at  $\pi/4$  with the horizontal direction is measured and monitored by the polarization analyzer (Agilent 8509C), shown in Figure 3-32. If the angle  $\pi/4$  does not appear, it can be achieved by simply adjusting the orientation of the input SOP before the sensing fiber.

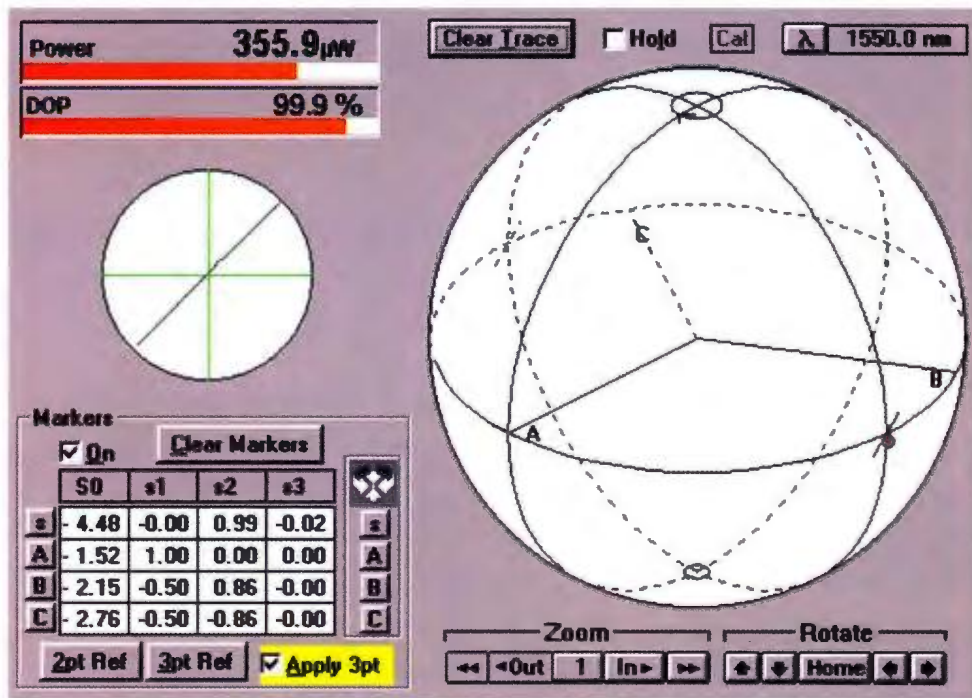


Figure 3-32 Linear output SOP after sensing fiber at  $\pi/4$  with  $x$ -axis.

The various amounts of bend-induced birefringence can be realized by alternating the bending diameters of the sensing fiber. The values of  $\beta_b$  are -1.14, -1.36, -1.70, -2.26, or -3.40 rad when the bending diameters  $R$  equal 6, 5, 4, 3, or 2 cm, respectively. The experimental result in Figure 3-33 indicates that the magnitude of sensitivity decreases from 0.0854 /A to 0.0474 /A when the magnitude of the bend-induced birefringence increases from 1.14 rad to 3.40 rad, which well agrees with the finding in Figure 3-26.

Twist-induced birefringence can be easily achieved by twisting the sensing fiber at certain angles. From the experimental result in Figure 3-34 the magnitude of sensitivity increases from 0.0403 /A to 0.0996 /A when the twist-induced birefringence increases from 0 to 10.90 rad. This result is consistent with the simulation result in Figure 3-27.

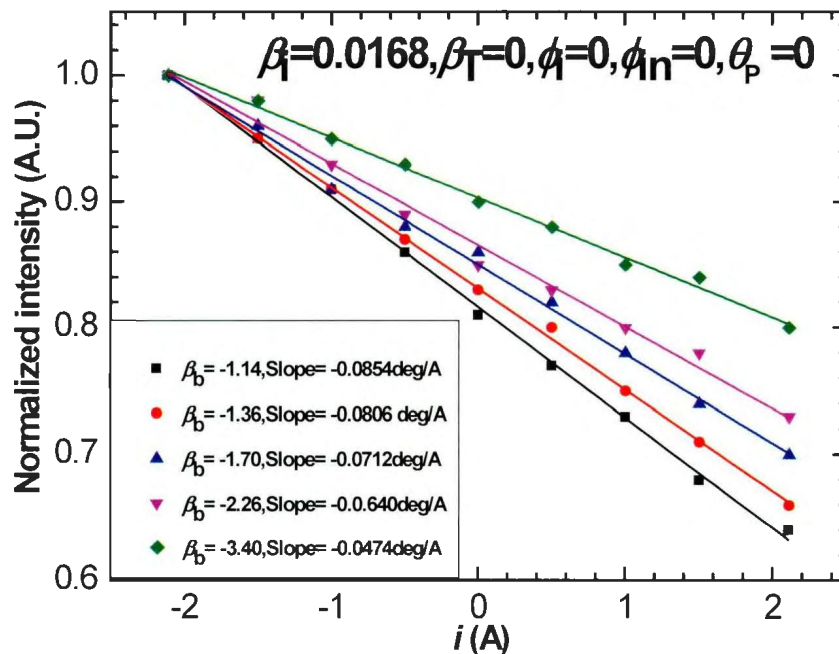


Figure 3-33 Experimental result: relationship between normalized intensity and bend-induced birefringence.

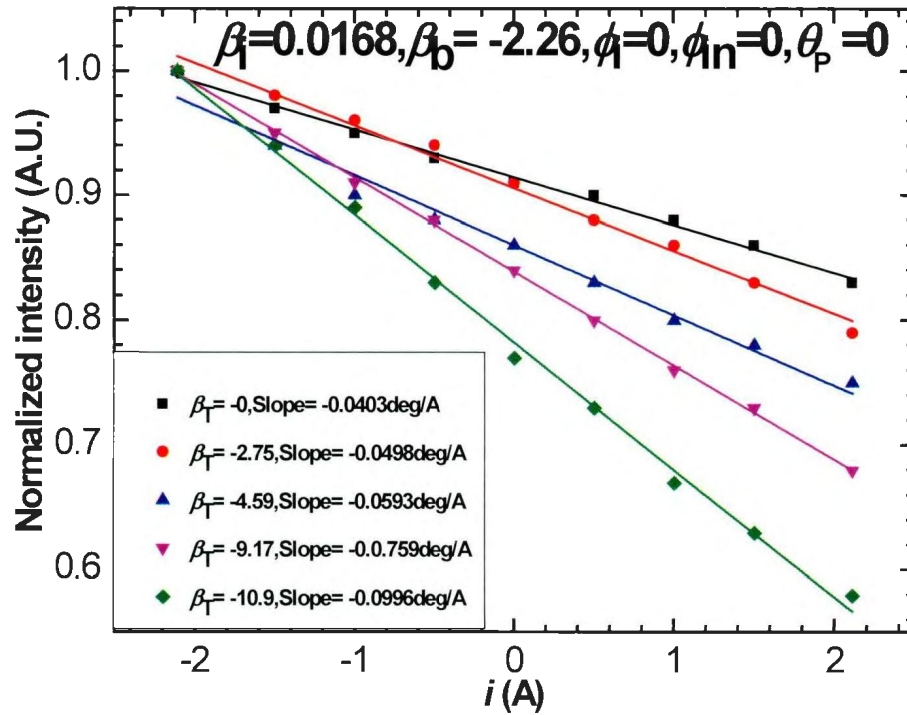


Figure 3-34 Experimental result: relationship between normalized intensity and twist-induced birefringence.

### 3.6 Summary

Through the study carried out in this chapter, the following conclusions can be drawn:

- (1) This study revealed the relationship between the orientation of the output SOP and measuring current, and theoretically and experimentally analyzed the dependence of the sensitivity on different types of birefringence;
- (2) Intrinsic and bend-induced birefringence degrade the sensitivity and linearity of the sensing curve at lower current range while a high sensitivity persists in the larger current range;

(3) Sufficient amount of twist-induced birefringence can help maintain an excellent sensitivity and linearity by shifting the sensing curve;

(4) Elliptical and circular initial input SOP degrade the sensitivity and linearity, in which a pre-polarizer can be employed to stabilize the linear input SOP to improve the sensitivity and linearity of the sensing curve.

(5) The orientation of linear initial input SOP has no effect on the sensitivity and linearity of the sensing curve. However, the different orientation angle shifts the sensing curve, which results in a whole range measurement of current.

## Chapter 4 Reflective Scheme of Fiber Optic Current Sensor

### 4.1 Experimental setup of the reflective scheme

Reflective scheme of FOCS is generally employed and built by engineers to bring a FOCS into practical applications [100-104]. This reflective scheme is widely deployed mainly because: (1) the cost of detecting Faraday rotation in intensity is much lower than the cost of the detecting approach in the basic scheme; (2) the influence of the intrinsic birefringence, bend-induced birefringence and twist-induced birefringence in the sensing fiber can be eliminated by nonreciprocal approach while the effect of Faraday rotation can be doubled, resulting in an enhanced sensitivity, four times of the value in the basic scheme as a result of differential phase delay in the reflective scheme.

Reflective scheme operates by combining a forward optical path and a reflective optical path. As shown in Figure 4-1, the beam of light source from a laser source is firstly linearly polarized in an inline polarizer. Then, the beam of forwarding light is split into a pair of orthogonal linearly polarized light propagating in PM fiber when the beam of light enters the PM fiber forming  $45^\circ$  orientation of polarization with the axes of PM fibers. Next, the pair of orthogonal linearly polarized light evolves into a pair of left and right circular light waves after the effect of a quart-wave retarder when the pair of orthogonal light enters the retarder forming  $45^\circ$  orientation of polarization with the axes of retarder. After that, the pair of left and right circular light waves enters the sensing fiber and is reflected back by an inline reflector connected at the end of the sensing fiber. After going

through the backward path, the intensity of the backward light encoded with current information is detected by a photodetector.

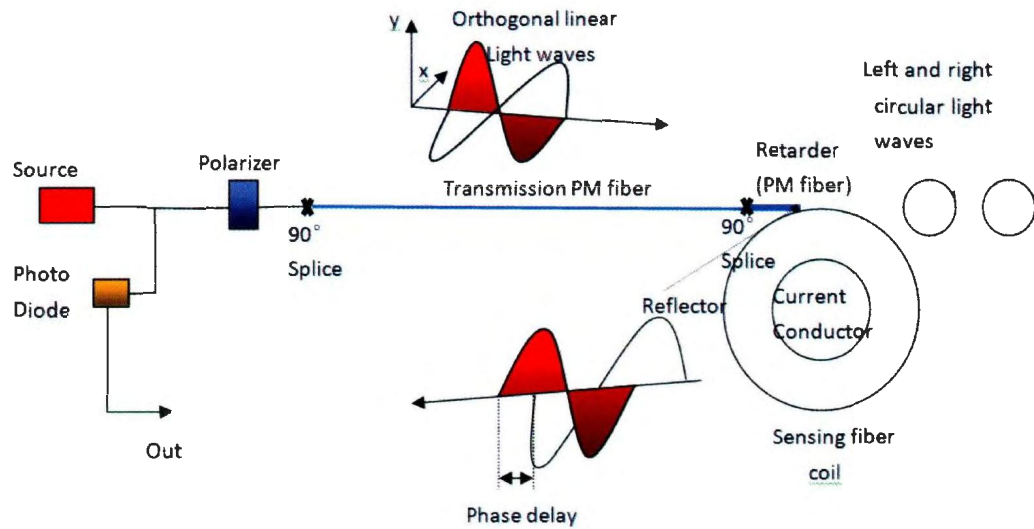


Figure 4-1 Experimental setup of FOCS with a reflective scheme

For an ideal case with a perfect  $90^\circ$  retarder and accurate connecting azimuths, the interfered light intensity can be detected by a power meter, which is expressed as [105-107]:

$$I_{out} = \frac{1}{2} I_m (1 + \cos(4\varphi_F)) = \frac{1}{2} I_m (1 + \cos(4VN_i N_f i)) = I_m \cos^2(2VN_i N_f i) \quad (4-1)$$

where  $\varphi_F = VN_i N_f i$  is the Faraday rotation, and  $I_m$  is the light intensity of the input light.

Thus, Eqn. (4-1) can be rewritten as:

$$\cos^{-1}\left(\sqrt{\frac{I_{out}}{I_m}}\right) = 2VN_i N_f i \quad (4-2)$$

To further analyze the propagation of the forward and backward SOP in the experimental setup, the Jones calculus is employed to describe this process. In the experimental setup, the  $x$  and  $y$  axes are set to be  $45^\circ$  with respect to the input linear polarization. Thus, the input SOP is described as:

$$E_{in} = \frac{1}{\sqrt{2}} \begin{pmatrix} 1 \\ 1 \end{pmatrix} \quad (4-3)$$

The PM fiber is set with its fast and slow axes along the  $x$  and  $y$  axes in which the forward and backward Jones matrices are expressed [105]:

$$J_{PM,f} = J_{PM,b} = \begin{pmatrix} \exp(ik\Delta nL/2) & 0 \\ 0 & \exp(-ik\Delta nL/2) \end{pmatrix} \quad (4-4)$$

where  $k = 2\pi/\lambda$  is the wavenumber,  $\Delta n = 0.00043$  is the birefringence of the PM fiber (PM 15-U40A), and  $L$  is the length of the PM fiber.

The quarter wave retarder has its fast and slow axes orientated at  $45^\circ$  with the  $x$  and  $y$  axes,  $45^\circ$  with the birefringence axes of the PM fiber. Therefore, the forward and backward Jones matrixes are written as [105]:

$$J_{R,f} = \begin{pmatrix} \cos(R/2) & i \sin(R/2) \\ i \sin(R/2) & \cos(R/2) \end{pmatrix} \quad (4-5a)$$

$$J_{R,b} = \begin{pmatrix} \cos(R/2) & -i \sin(R/2) \\ -i \sin(R/2) & \cos(R/2) \end{pmatrix} \quad (4-5b)$$

where  $R = \pi/2$  for an ideal quarter wave retarder, and  $R = \pi/2 + \Delta R$  for a non-ideal retarder.

The forward and backward of Jones matrixes for a Faraday sensing coil can be defined as [105]:

$$J_{F,f} = \begin{pmatrix} \cos(\varphi_F) & \sin(\varphi_F) \\ -\sin(\varphi_F) & \cos(\varphi_F) \end{pmatrix} \quad (4-6a)$$

$$J_{F,b} = \begin{pmatrix} \cos(\varphi_F) & -\sin(\varphi_F) \\ \sin(\varphi_F) & \cos(\varphi_F) \end{pmatrix} \quad (4-6b)$$

The Jones matrix of the ending mirror put at the end of the sensing fiber is represented by [105]

$$J_M = \begin{pmatrix} -1 & 0 \\ 0 & 1 \end{pmatrix} \quad (4-7)$$

The reflected beams of light interfere at the input polarizer that is at  $45^\circ$  with respect with the  $x$  axes, which gives the interference Jones matrix of the polarizer [105]:

$$J_P = \frac{1}{2} \begin{pmatrix} 1 & 1 \\ 1 & 1 \end{pmatrix} \quad (4-8)$$

As a result, the output SOP is:

$$E_{out} = J_P J_M J_{PM,b} J_{R,b} J_{F,b} J_M J_{F,f} J_{R,f} J_{PM,f} E_{in} \quad (4-9)$$

The first  $J_M$  of the Eqn. (4-9) is introduced to distinguish the backward-travelling waves from the forward-travelling waves [108]. As a result, the detected output intensity is:

$$I_{out} = E_{out}^T E_{out}^* \quad (4-10)$$

If assuming the input light intensity  $I_{in} = E_{in}^T E_{in}^* = 1$ , Eqn. (4-2) turns into

$$\cos^{-1}(\sqrt{I_{out}}) = \cos^{-1}(\sqrt{E_{out}^T E_{out}^*}) = 2VN_i N_f i \quad (4-11)$$

In the experiment, we replace the  $I_{out}$  with  $I_{nor} = I_{out}(i)/I_{in}(0)$  to calculate the phase delay defined below.

Define

$$\frac{\phi_R}{2} = \cos^{-1}(\sqrt{I_{nor}}) = 2\phi_F \quad (4-12)$$

as half phase delay in the reflective scheme.

Thus,

$$i = \frac{\phi_R}{4N_i N_f} = \frac{2\cos^{-1}(\sqrt{I_{nor}})}{4N_i N_f} \quad (4-13)$$

From Eqns. (4-11), (4-12) and (4-13), the measuring current can be derived from the linear relationship between the phase delay  $\phi_R$  and the measuring current  $i$ , shown in Figure 4-2. The phase delay  $\phi_R$  can be determined by detecting the output light intensity with calculation according to Eqn. (4-13). At this step, the dependence of the sensitivity and linearity on connecting azimuth which is the angle between the fast axis of a PM fiber and the fast axis of a retarder during connection, retarder deviation and coherence of laser source can be further investigated from both theoretical and experimental perspectives.

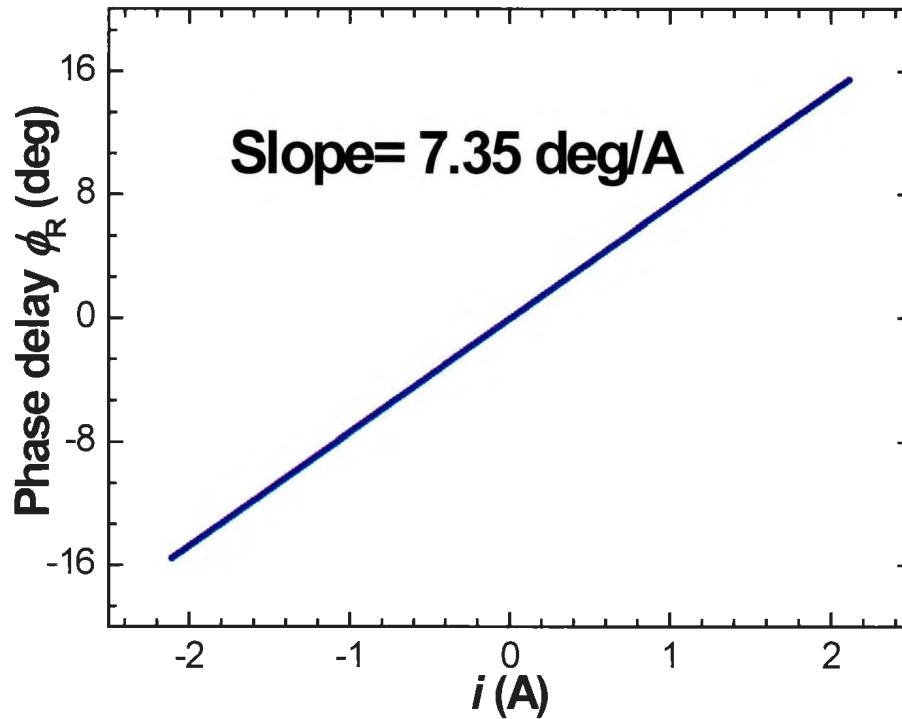


Figure 4-2 Ideal relationship between detected phase delay and current in the reflective scheme

## 4.2 Dependence of sensitivity on parameters: simulation perspective

### 4.2.1 Dependence on deviated amount of retarder

Generally, a perfect  $90^\circ$  retarder cannot be always maintained in practical applications due to either manufacture error or the intended design by designers to compensate measurement bias caused by temperature change [106, 109]. As the expression of Eqn. (4-5),  $R = \pi/2 + \Delta R$  for a non-ideal retarder is employed to describe a non-ideal retarder. The dependence of sensitivity and linearity on  $\Delta R$  is further analyzed in Figure 4-3.

In Figure 4-3, the sensing curves are derived at  $\Delta R = -8^\circ, -4^\circ, 0^\circ, 2^\circ, 5^\circ,$  and  $10^\circ$  separately. From the simulation results based on Eqns. (4-11), (4-12) and (4-13), the sensitivity and the linearity of sensing curves are reduced, especially in small current region (for instance,  $-0.5 \text{ A} \sim +0.5 \text{ A}$ ). When the amount of deviation increases, the nonlinearity will increase and the magnitude of sensitivity of sensing curves will decrease. This result requires a highly perfect retarder when a higher sensitivity is demanded in the reflective FOCS.

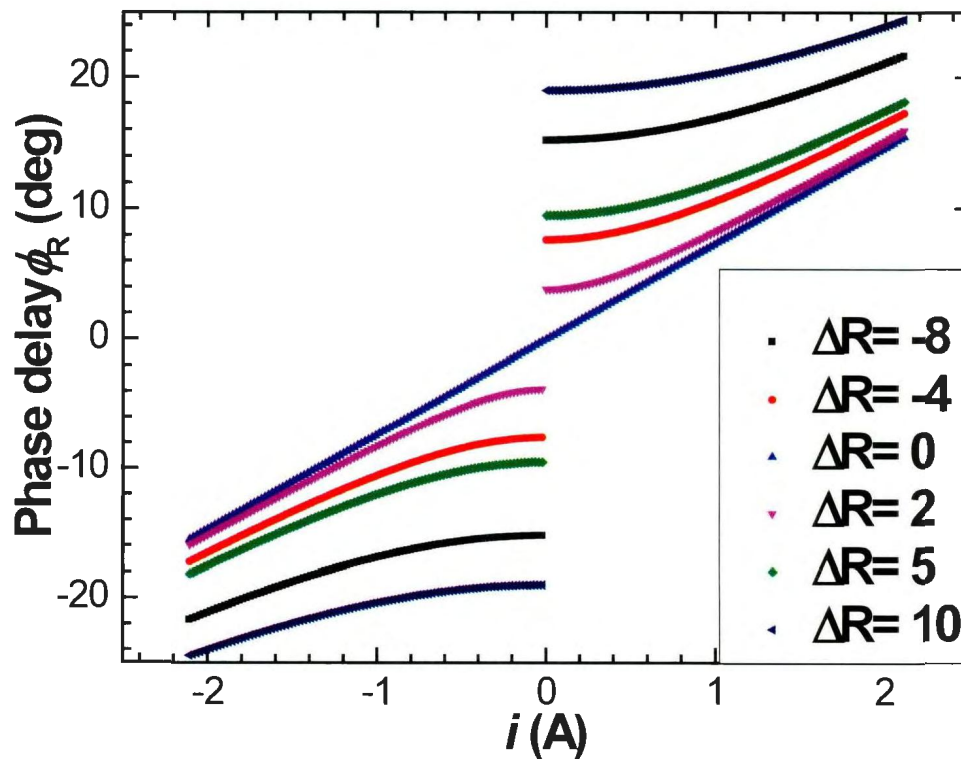


Figure 4-3 Dependence of sensitivity on the deviated amounts of retarder

#### 4.2.2 Dependence on deviated amount of connecting azimuth

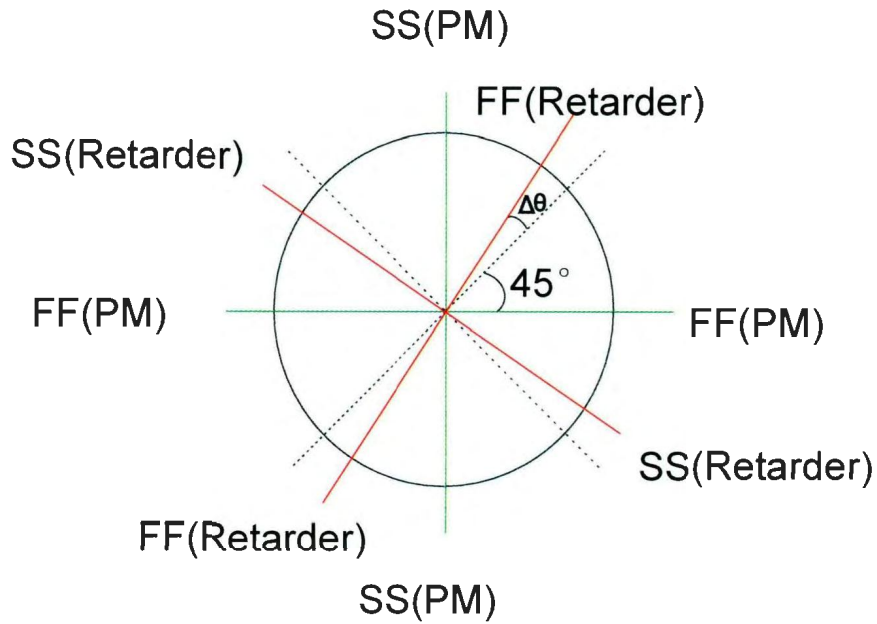


Figure 4-4 Cross section of connecting fiber cores between PM fiber and retarder (SS and FF indicates slow axis and fast axis respectively)

In some practical applications, the connecting azimuths between the birefringent axes of a PM fiber and the birefringent axes of a retarder is possibly not a perfect  $45^\circ$  alignment, shown in Figure 4-4. If the deviation of connection azimuth from the  $45^\circ$  alignment is assumed as  $\Delta\theta$ , the effect of this deviation on the propagation of SOP can be described from the Jones calculus.

Define rotation matrix:

$$R(\Delta\theta) = \begin{pmatrix} \cos(\Delta\theta) & -\sin(\Delta\theta) \\ \sin(\Delta\theta) & \cos(\Delta\theta) \end{pmatrix} \quad (4-14)$$

Therefore, the resultant SOP can be derived by rewriting Eqn. (4-9)

$$E_{out} = J_p J_M J_{PM,b} R(-\Delta\theta) J_{R,b} R(\Delta\theta) J_{F,b} J_M J_{F,f} R(\Delta\theta) J_{R,f} R(-\Delta\theta) J_{PM,f} E_{in} \quad (4-15)$$

With this revised output SOP and Eqns. (4-10), (4-11), (4-12) and (4-13), the dependence of the sensitivity on this deviation is further studied in Figure 4-5.

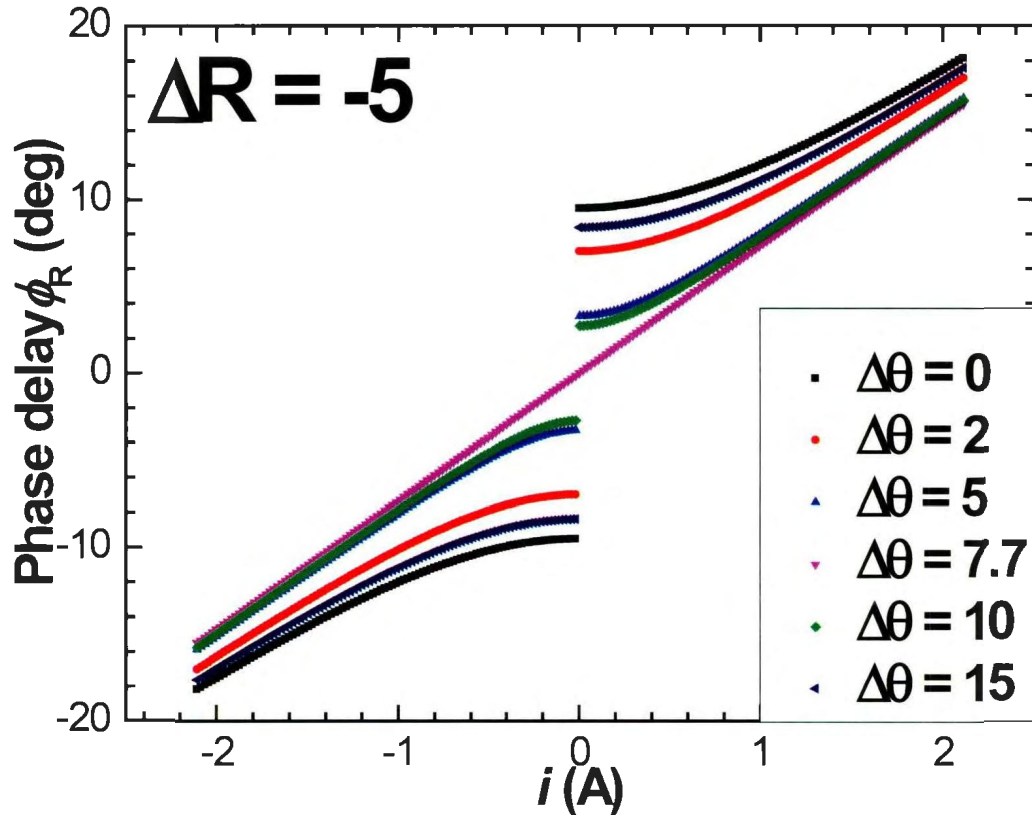


Figure 4-5 Dependence of sensitivity on the connecting azimuths

The simulation results in Figure 4-5 illustrate that the sensitivity and the linearity of the sensing curves have been degraded when the connecting azimuths deviate from an exact  $45^\circ$ , particularly in a small current range (for example,  $-0.5 \text{ A} \sim +0.5 \text{ A}$ ). However, when  $\Delta\theta$  approaches to degrees, the deviation of connecting azimuths compensates the low sensitivity and nonlinearity of the sensing curves caused by the deviation of the

retarder, such as the case shown by the curve at  $\Delta\theta = 7.7$  in Figure 4-5. Some studies appropriately adjust the deviation of the connecting azimuth and the deviation of retarder to achieve a good compensation for the Verdet constant of the sensing fibers, which allows FOCS to have a sensitivity of  $\pm 0.2\%$  within a large temperature range ( $-40^{\circ}\text{C} \sim 85^{\circ}\text{C}$ ) [106, 109].

### 4.3 Dependence of sensitivity on parameters: experimental perspective

#### 4.3.1 Dependence on deviated amount of retarder

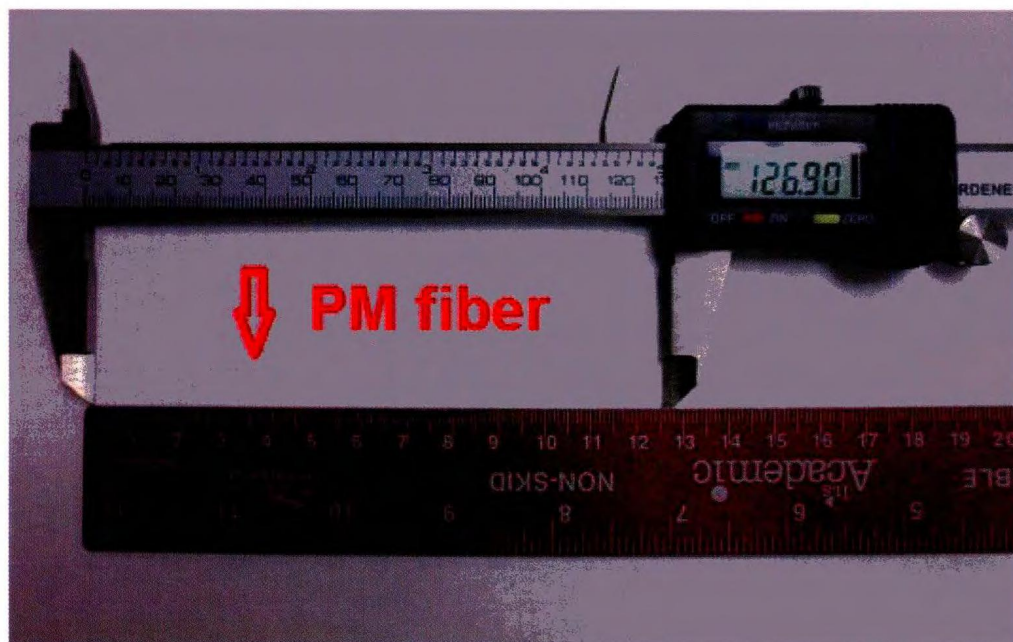


Figure 4-6 Length of the PM fiber (PM-15U40A, retarder)

Beat length is a phenomenon in which the period of interference effects in a birefringent medium. According to the measurement approach of beat length in Ref. [13] and [110], the beat length of the employed PM fiber (PM-15U40A) is measured to be

3.60 mm. Thus, we can make a quarter wavelength retarder from an appropriate length of PM fiber, for instance, a segment of PM fiber with  $126.90 \text{ mm} = 1/4 \times 3.60 \text{ mm} + 3.60 \text{ mm} \times 35$ , shown in Figure 4-6. The deviated retarder of  $-8^\circ, -4^\circ, 0^\circ, 2^\circ, 4^\circ, 10^\circ$  are also achieved making PM fibers at 126.82, 126.86, 126.90, 126.92, 126.94, and 127.00 mm respectively.

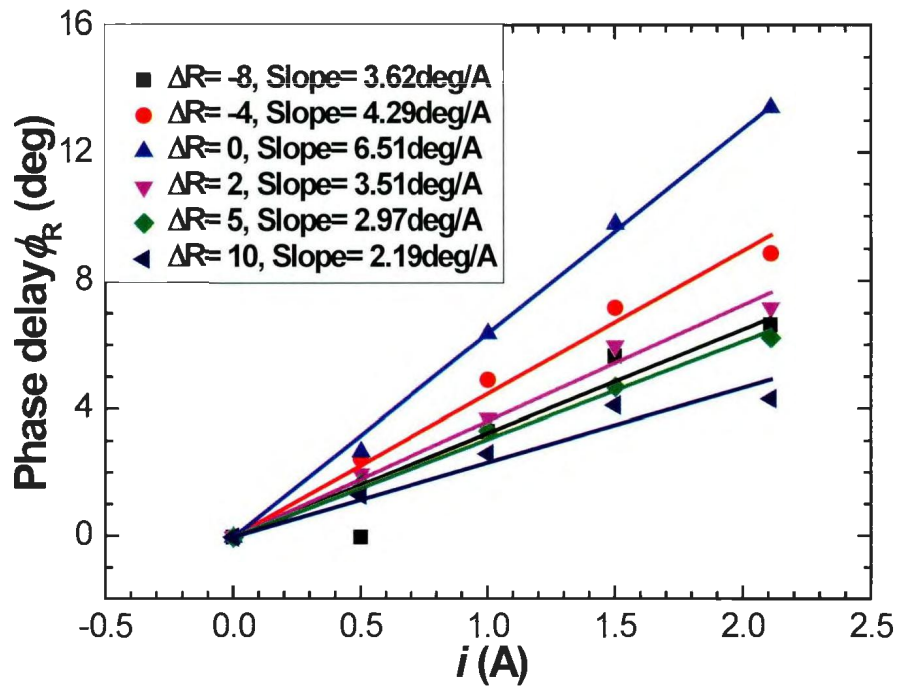


Figure 4-7 Experimental result: dependence of sensitivity on deviation of retarder at perfect connecting azimuth with 90 m PM fiber

From the experimental result in Figure 4-7, the sensitivities of the sensing curves have been degraded when the deviation of the retarder exists. The magnitude of sensitivities will be even lower when the absolute amounts of deviation of the retarder increases from  $2^\circ$  to  $10^\circ$ . The experimental result shows a good agreement with the simulation result in Figure 4-3.

### 4.3.2 Dependence on deviated amount of connecting azimuth

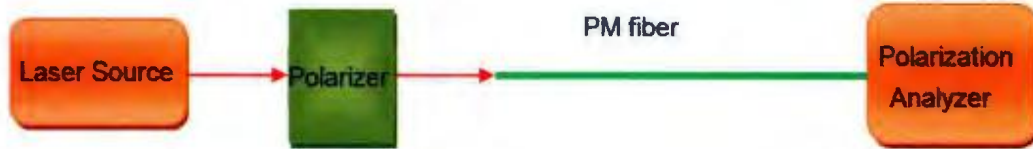
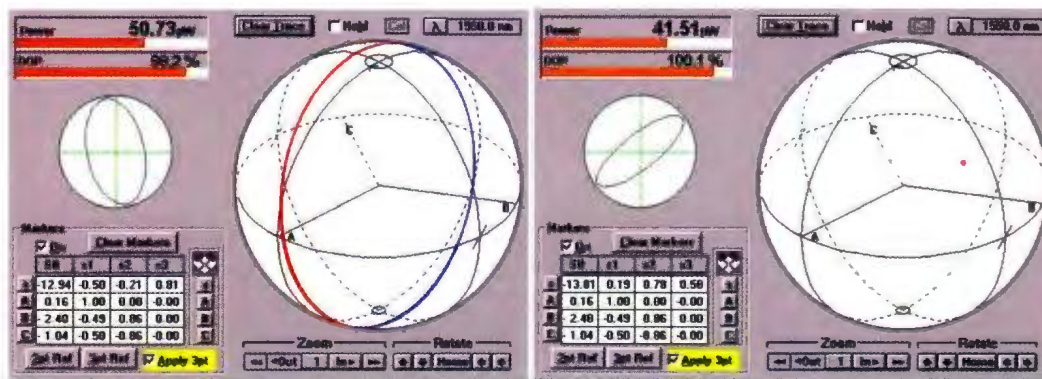


Figure 4-8 Determination of the birefringent axes of PM fiber (PM-15U40A)

Before investigating the dependence of sensitivity on connecting azimuth, the birefringent axes of PM fiber must be firstly determined in a polarization frame reference which defines the reference orientations of SOP with  $0^\circ$ ,  $60^\circ$  and  $120^\circ$  orientations (A, B, and C on Poincare sphere in Figure 4-9 indicate the  $0^\circ$ ,  $60^\circ$  and  $120^\circ$  orientations). Shown in Figure 4-8, with the given orientation of the inline polarizer, the birefringent axes are determined by observing the traces of the output SOP on Poincare sphere from the polarization analyzer (Agilent 8509C) while extruding or heating the PM fiber by hands.



(a)

(b)

Figure 4-9 The alignment of PM fiber: (a)  $45^\circ$  alignment between the linearly polarized SOP and the PM fiber; (b)  $0^\circ$  alignment between the linearly polarized SOP and the PM fiber.

The orientation of inline polarizer is firstly in the established polarization frame reference. Shown in Figure 4-9(a), the trace of output SOP forms a complete circle during extruding the transmission PM fiber, which indicates that the birefringent axes of the PM fiber are  $45^\circ$  with the orientation of the inline polarizer because there are two beams of light equally splitted from the inline polarizer propagating in the PM fiber. Shown in Figure 4-9(b), the trace of the output SOP remains a dot during the extruding process, which indicates that the birefringent axes of the PM fiber are  $0^\circ$  with the orientation of the polarizer because there is only one beam from inline polarizer propagating in the PM fiber. Thus, we can immediately mark the birefringent axes of the PM fiber by a tape.

By several reset of the connecting azimuths of the PM fiber, the dependence of sensitivity can be experimentally studied.

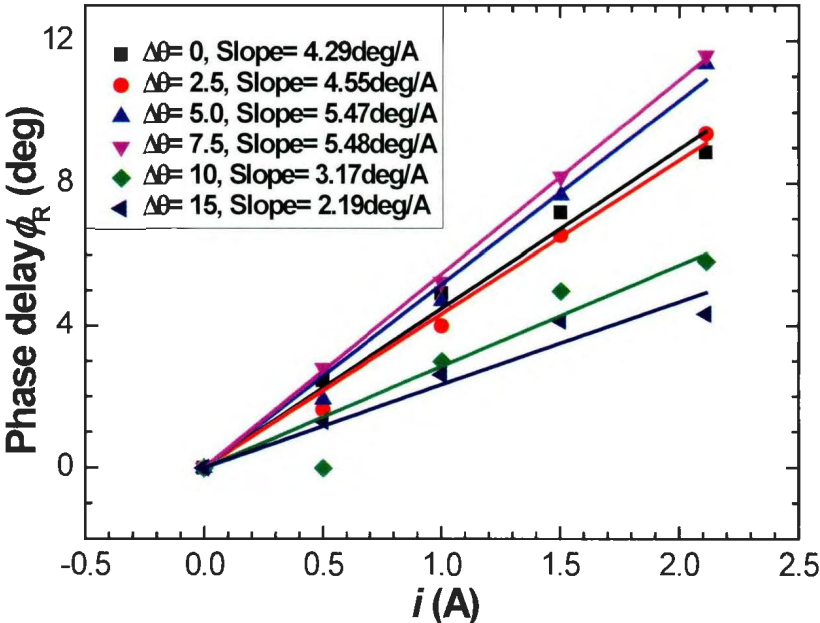


Figure 4-10 Experimental result: dependence of sensitivity on deviation of retarder at  $-4^\circ$  deviation of retarder with 90 m PM fiber

The result in Figure 4-10 shows that various amounts of deviations of connecting azimuths have different effect on the sensitivity when a deviation of retarder exists. Appropriate amount of deviation can experimentally compensate the negative effect of the deviation of the retarder.

#### 4.4 Dependence of light intensity stability on the length of PM fiber

The coherent length of a laser source is defined as [105]:

$$L_c = \lambda^2 / \Delta\lambda \quad (4-16)$$

where,

$\lambda$  is the typical wavelength of a laser source,  $\lambda = 1.55 \mu\text{m}$  in our experiment;

$\Delta\lambda$  is the spectral bandwidth of a laser source,  $\Delta\lambda = 2.0 \text{ nm}$  in our experiment.

Thus, the coherent length of the laser source (tunable laser source 8168F) we used is:

$$L_c = \lambda^2 / \Delta\lambda = 1201 \mu\text{m} \quad (4-17)$$

From Eqn. (4-4), if the round-trip of the optical path going through PM fiber is too small, the output intensity is very likely to suffer from the disturbance resulting from the temporal interference caused by the laser source. The optical path imbalance along the fast axis and slow axis is:

$$2\Delta L = (2 \times L / L_b) \times \lambda \quad (4-18)$$

where,

$L_b$  is the beat length of the PM fiber (PM-15U40A), and  $L_b = 3.60 \text{ mm}$  in our experiment.

Generally, in order to obtain stable output interfering intensity induced by Faraday phase delay, it requires [105]:

$$2\Delta L \geq 20L_c \quad (4-19)$$

We further experimentally studied the dependence of stability of interfered light intensity on the length of the PM fiber at PM fiber lengths of  $L = 0.11, 1.00, 5.00,$  and  $90.00\text{m}$ .

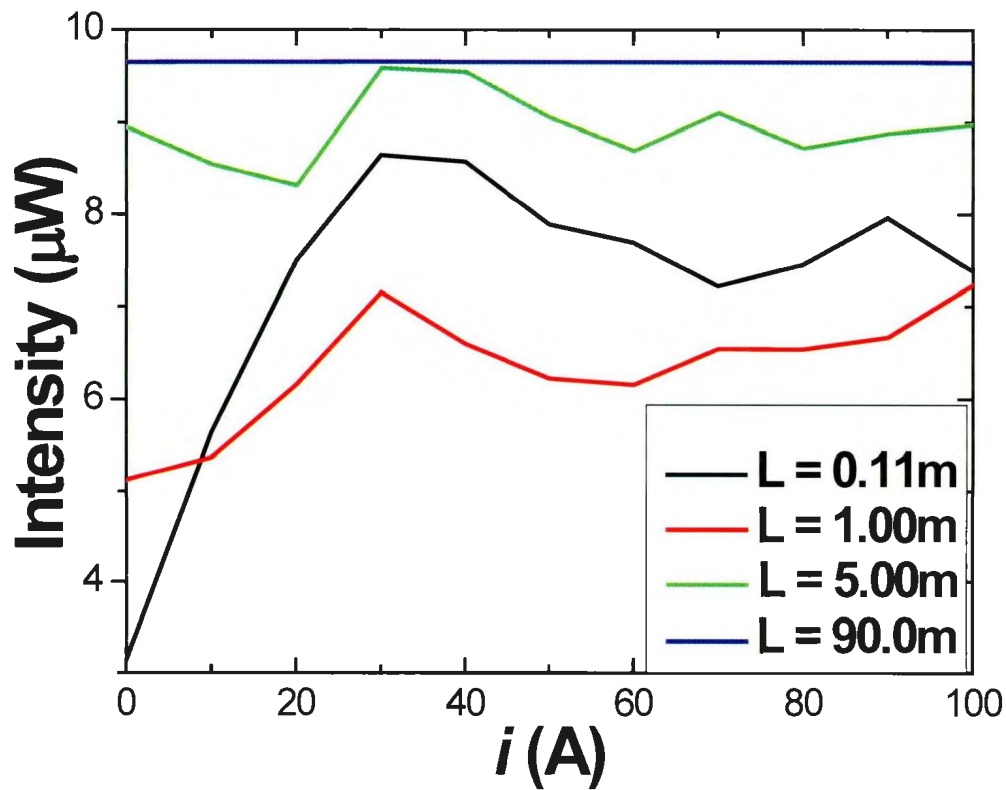


Figure 4-11 Experimental result: Dependence of stability of interfered light intensity on length of PM

The experimental result in Figure 4-11 indicates that, a longer length of PM fiber at  $90.00\text{ m}$  shows a good stable output interfering intensity.

## **4.5 Summary**

Some conclusions can be derived from above investigation:

- (1) Some amount of deviation from a perfect retarder reduces the sensitivity and linearity;
- (2) Some amount of deviation from critical connecting azimuth degrades the sensitivity; however, sufficient amount of connecting azimuth can maintain an excellent sensitivity and linearity;
- (3) A long length of PM fiber helps stabilize the detected light intensity.

# **Chapter 5 Wireless Sensing System for Fiber Optic**

## **Current Sensors**

### **5.1 Realization of wireless communications in fiber-optic sensing**

#### **systems**

Wireless data communication technique has been widely used in various applications to achieve wireless sensing system including wildlife monitoring, habitat monitoring, surveillance and industrial measurements in recent decade [63, 111, 112]. Wireless data communication has also been deployed in fiber-optic sensing systems to achieve different applications in recent years [113-119]. Compared with traditional fiber-optic sensing system based on optical fiber communication, wireless sensing systems based on wireless data communication are much advanced in multiplexing large number of different sensor nodes, forming various types of sensor networks, improving sensing system performance, and reducing installation and maintaining cost [113-116]. Wireless data communications in fiber-optic sensing systems can be realized through a variety of approaches by employing either unlicensed wireless communication channels or commercial services to achieve a wireless communication with a distance ranging from several meters to tens of thousands kilometers [113, 114].

The demonstration of wireless data communication in this thesis will adopt an unlicensed communication channel around 2.4 GHz by deploying Zigbee Xbee Series 2 modules from Digi International company (shown in Figure 5-1) because of the unique

advantages of Zigbee modules including high performance, low power consumption, advanced network capability, and ease-of-use [120, 121]. Zigbee modules can achieve a wireless indoor communication distance of 40 m and a wireless outdoor communication distance of 120 m in any networking type of bus, ring, star, and mesh [122].



Figure 5-1(a) Architecture of wireless network with two Zigbee Xbee series 2 modules; (b) one Zigbee Xbee series 2 module with USB power supply and data communication.

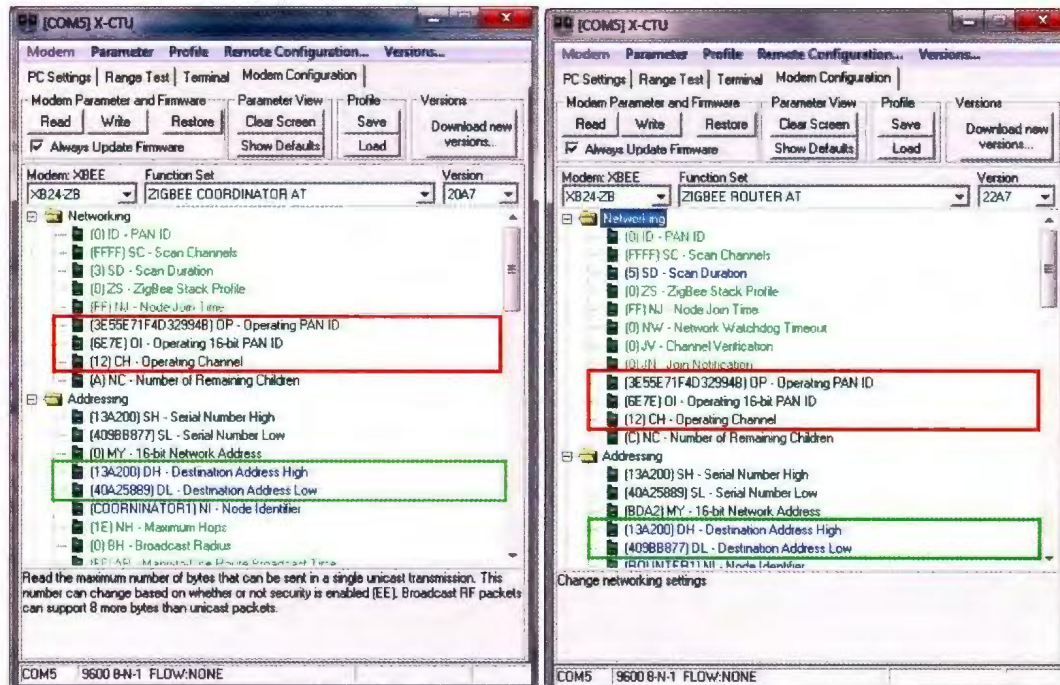
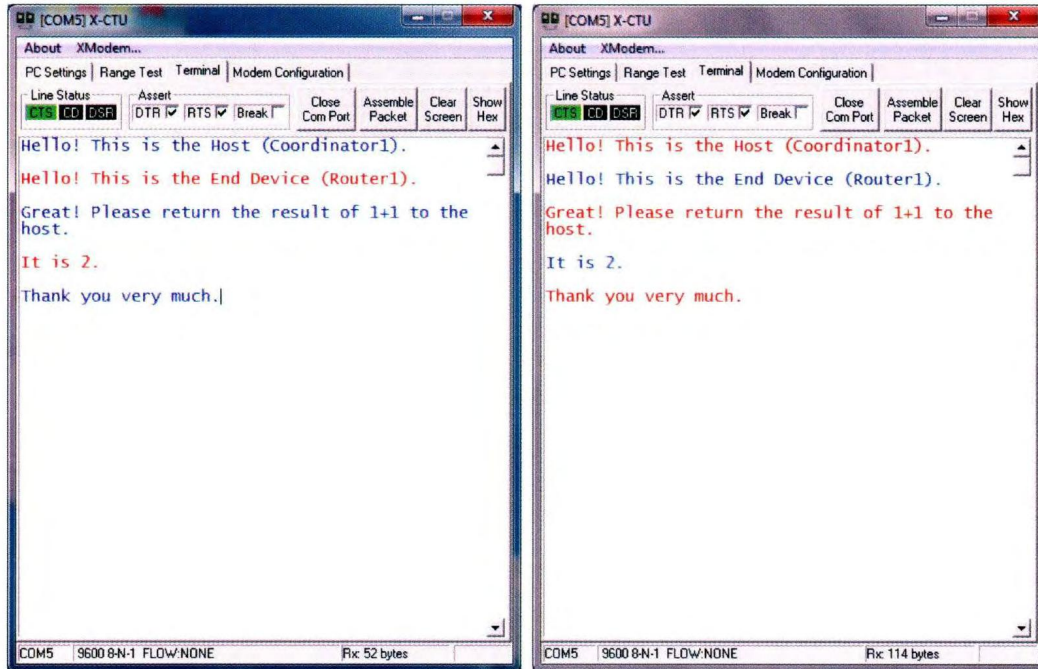


Figure 5-2 Building process of a wireless network with X-CTU software

A Zigbee wireless communication network is commonly formed by a Zigbee coordinator for starting and organizing a Zigbee network, Zigbee router for receiving and transmitting data, and Zigbee end device for acquiring data from sensor node [122]. The simplest Zigbee network is assembled by a Zigbee coordinator and a Zigbee router or a Zigbee end device by completing three steps of parameters settings with X-CTU software from Digi International Company shown in Figure 5-2: (1) building of Zigbee network coordinator by setting PAN (Personal Area Network) ID as 0 (to choose an arbitrary ID) and setting SC (Scan channels) as FFFF (to scan and arbitrarily choose available communication channel); (2) building of Zigbee network router (end device) by setting PAN ID as 0 (to join existing PAN ID) and setting SC (scan channels) as FFFF (to scan and choose existing communication channel); (3) setting of communication destination addresses: write the router's series number in coordinator's Destination Address (DH and DL); write the coordinator's series number in router's Destination Address (DH and DL).

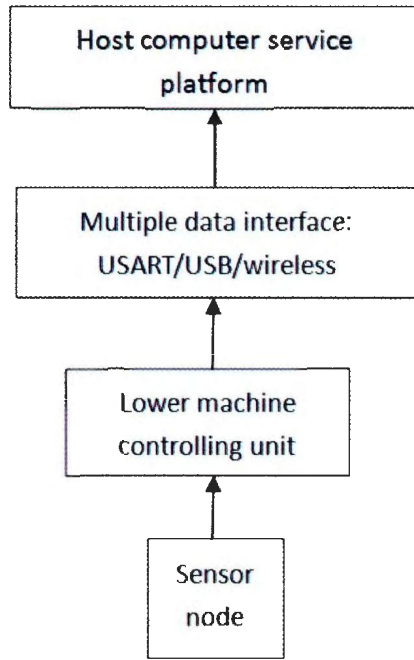
After successful building of Zigbee wireless communication network with necessary configurations of communication parameters, communication test can be completed from the coordinator X-CTU terminal and router (end device) X-CTU terminal within X-CTU software. As show in Figure 5-3, the sent data is in blue and the received data is in red.



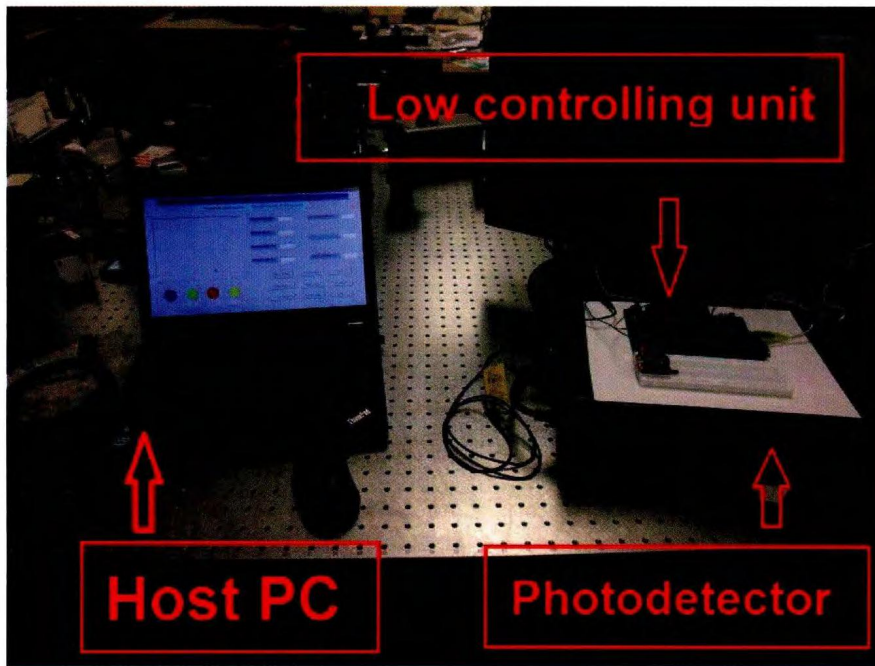
(a) Coordinator X-CTU (b) Router (End Device) X-CTU  
 Figure 5-3 Successful communication between the coordinator and the router

## 5.2 Design of hardware

The hardware design of wireless sensing system for FOCSs can be divided into sensor node, lower machine controlling units, multiple data interfaces, and host computer service platform shown in Figure 5-4. The multiple data interfaces include Universal Synchronous/Asynchronous Receiver/Transmitter (USART), Universal Serial Bus (USB), and wireless data communication.

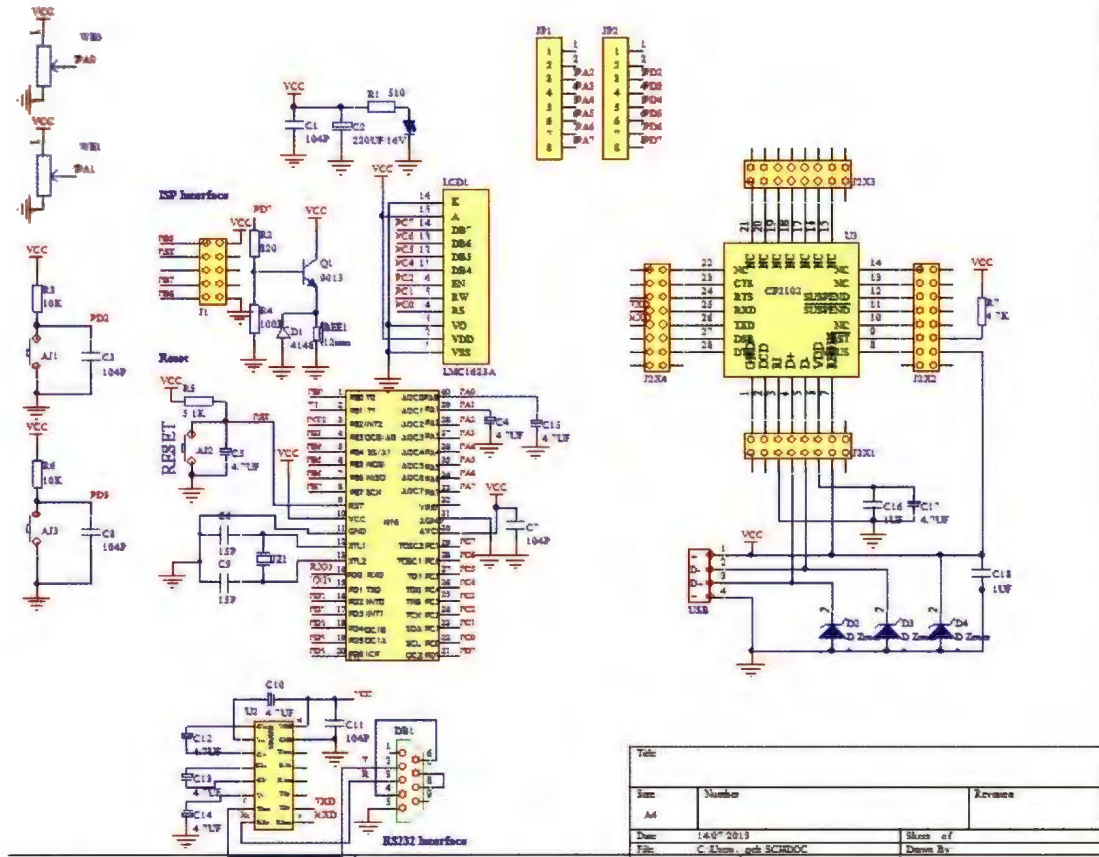


(a)

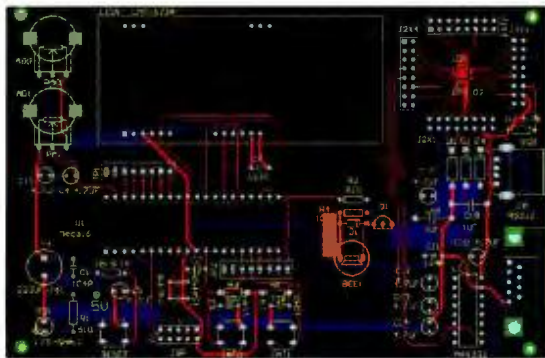


(b)

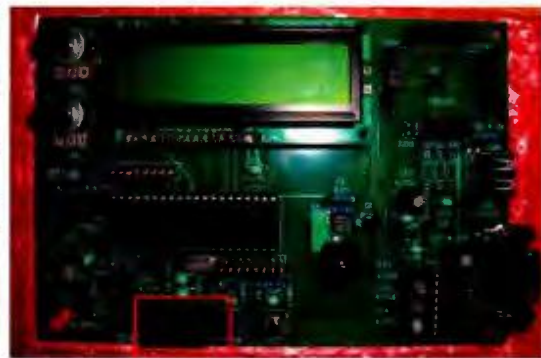
Figure 5-4 Architecture of wireless sensing system for FOCS: (a) principle of the FOCS wireless sensing system; (b) experimental layout of the FOCS wireless sensing system



(a)



(b)



(c)

Figure 5-5 Hardware design of lower machine controlling unit based on Altium Designer 10: (a) schematic design of electronic circuitry; (b) design of printed circuit board; (c) a complete printed circuit board with electronic components

The lower machine controlling unit which works under the control of a microprocessor (Atmel Mega 16L) comprises of the microprocessor and its power supply, LCD display, In-System Programming (ISP) interface, RS232 interface, and USB interface, shown in Figure 5-5 (a). The microprocessor, the core component of this unit, takes the task of receiving, processing, displaying, and transmitting the analog signal input from the PA2 port, shown in Figure 5-6. LCD display monitors and displays the real time data in transmission. ISP interface provides a communication channel between the microprocessor and a PC to download compiled controlling program into the microprocessor. RS232 interface and USB interface allows for multiple data interface between the lower machine controlling unit and the host computer service platform. Wireless communication channel can be achieved by connecting RXD and TXD ports of J2X4 with the data ports in Zigbee module, shown in Figure 5-6.

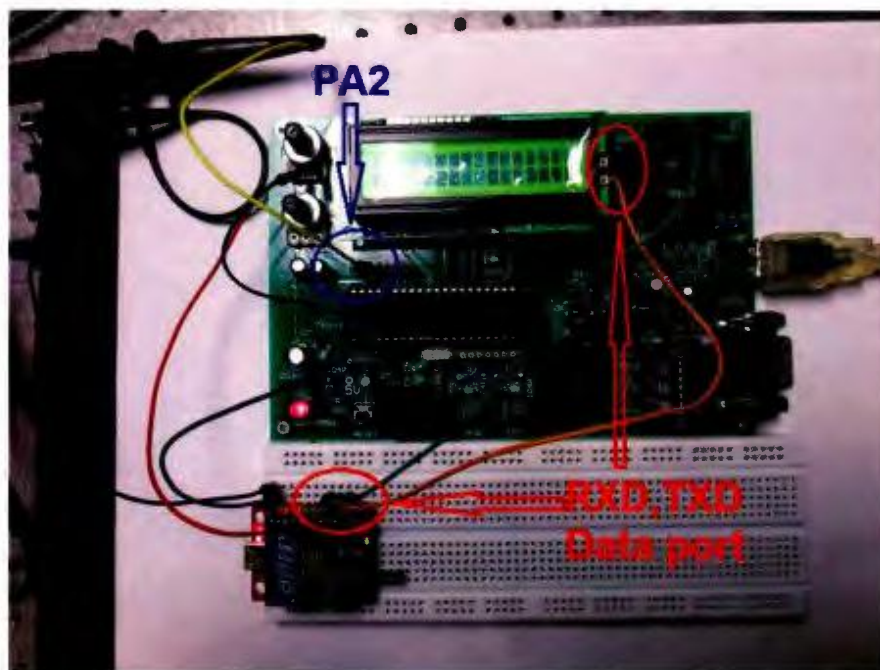
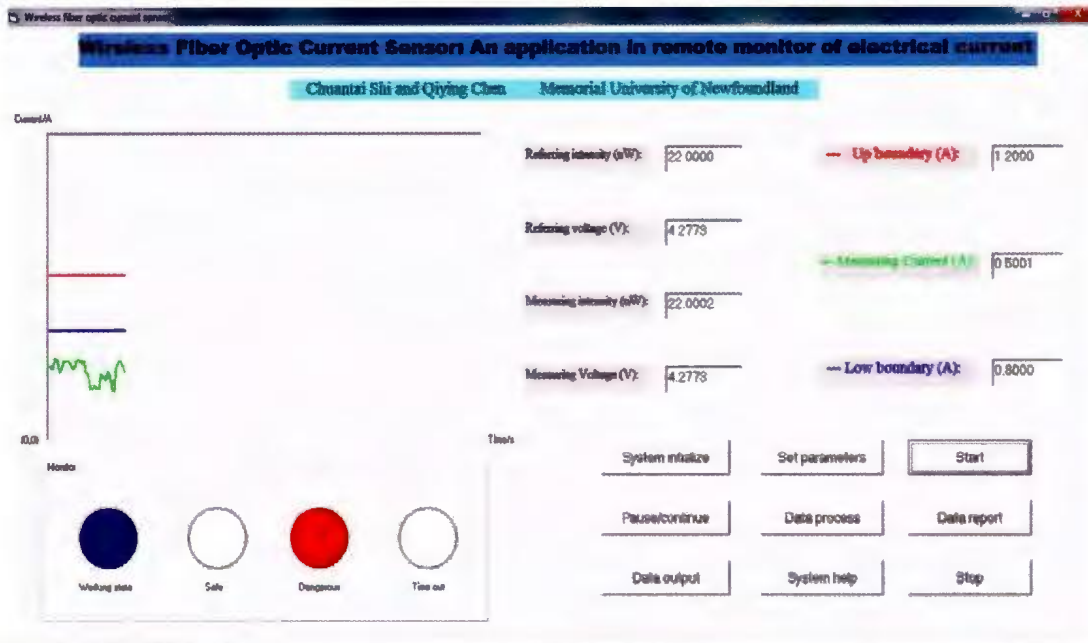
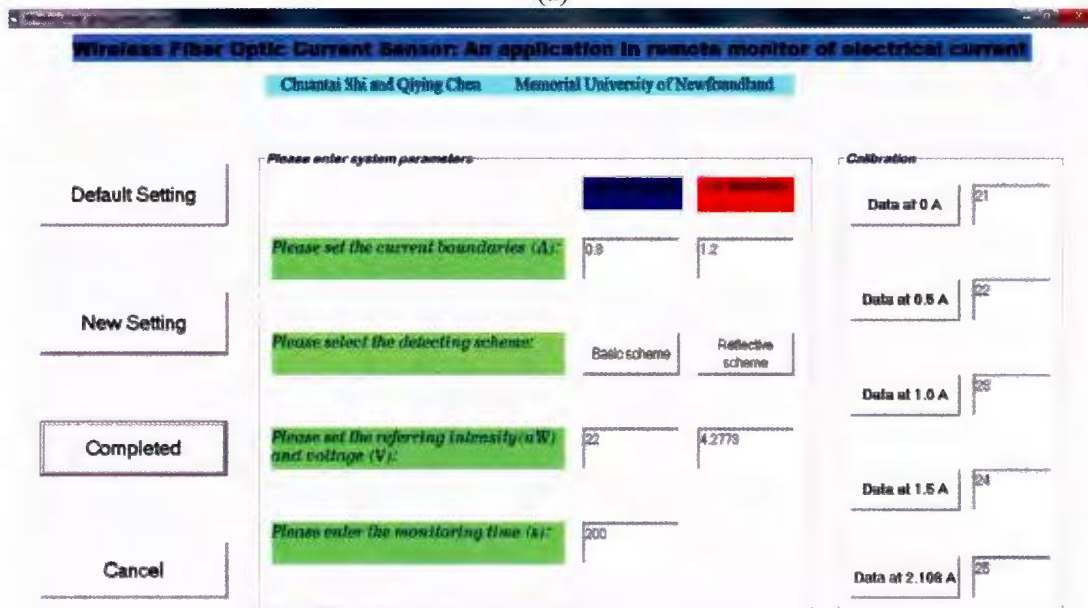


Figure 5-6 Hardware assembly of a power meter (under the circuit board), lower machine controlling unit, and Zigbee module

### 5.3 Design of software

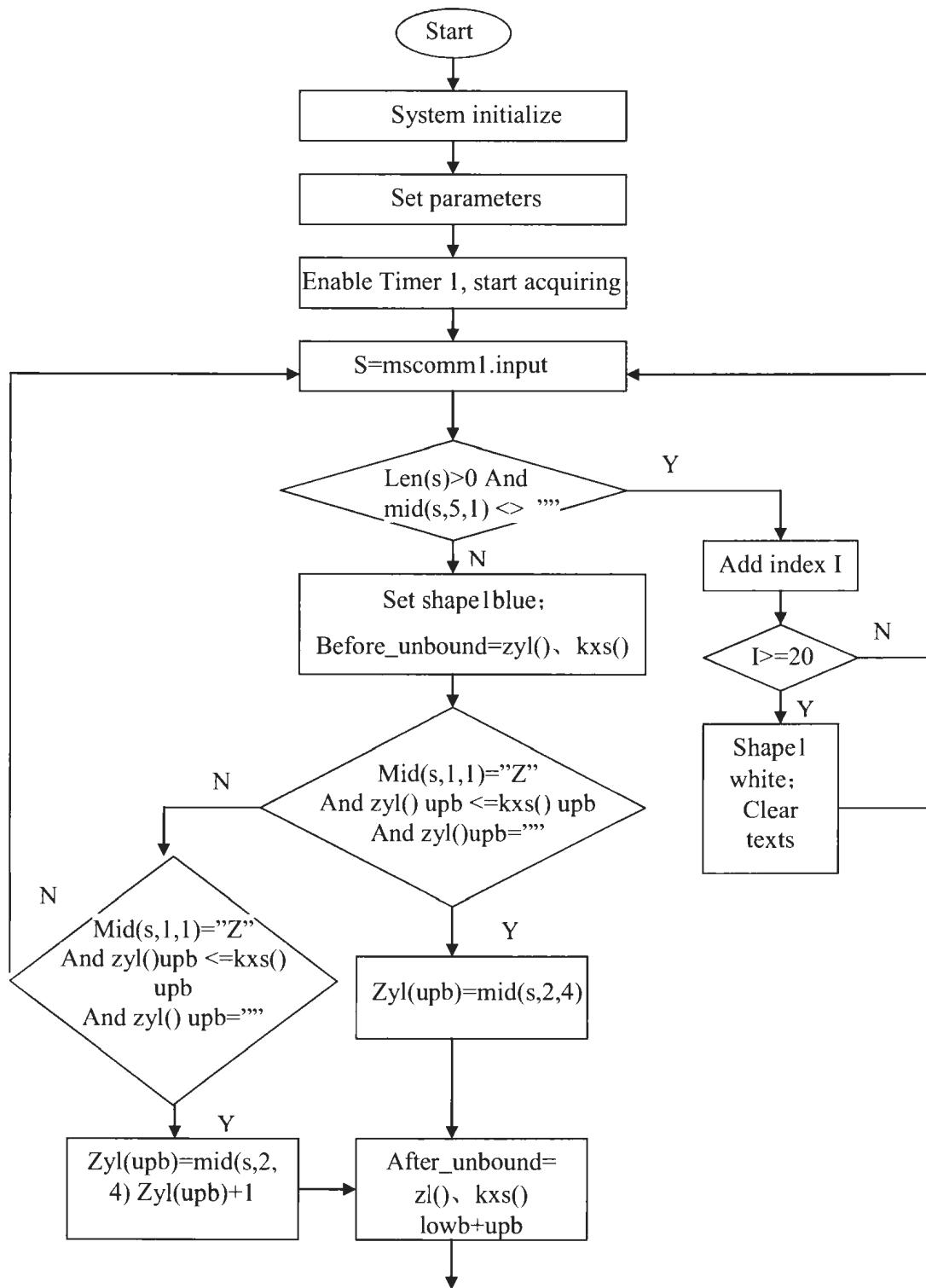


(a)



(b)

Figure 5-7 Design of host computer service platform on Microsoft Visual Basic 6.0: (a) main interface; (b) setting parameters interface



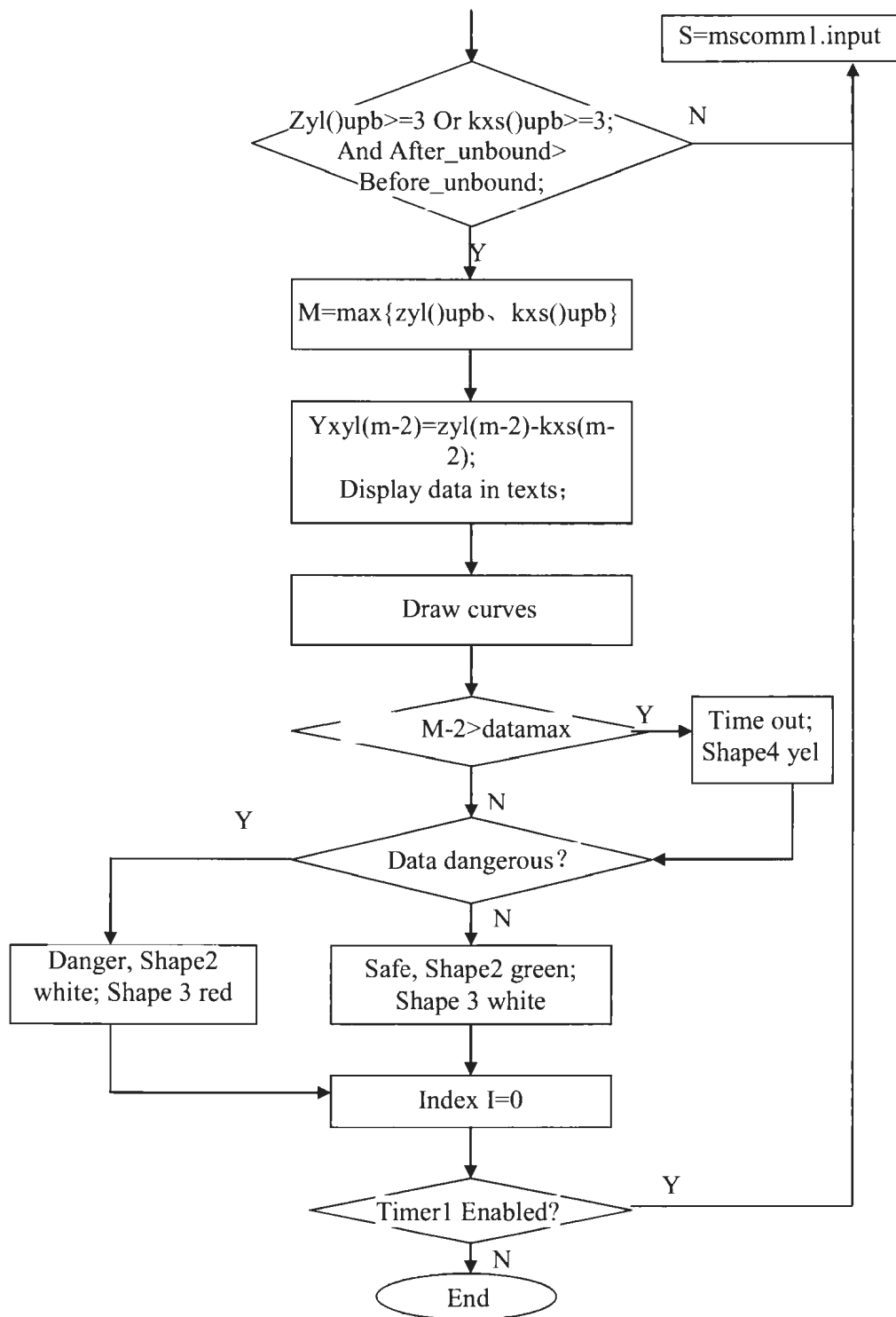


Figure 5-8 Program flow chart of host computer service platform

The software design includes the design of host computer service platform and the design of microprocessor controlling program.

Shown in Figure 5-7 (a), the main interface of the host computer service platform can display monitoring curves of sensing current, monitor the system working conditions and real time sensing data, and provide data processing commands. Before each monitoring, the second frame provides an interface to set system parameters and calibrate sensing curve, shown in Figure 5-7 (b). The program flow chart is illustrated in Figure 5-8.

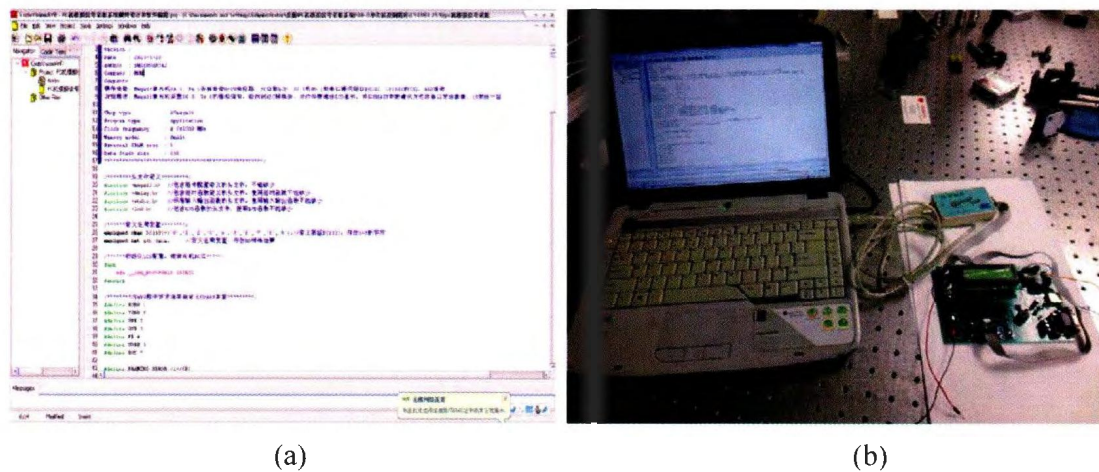


Figure 5-9 Compiled controlling program was downloaded into the microprocessor: (a) program writing environment; (b) downloading program through ISP communication

The design of microprocessor controlling program was firstly written in C programming language based on Code Vision AVR software platform and then compiled in HEX file which contained executing codes for the microprocessor. Finally, the executing codes were downloaded into the flash programming memory of the microprocessor for executing through an ISP communication port (marked red in Figure 5-5 (c)). The controlling program process is organized in Figure 5-10.

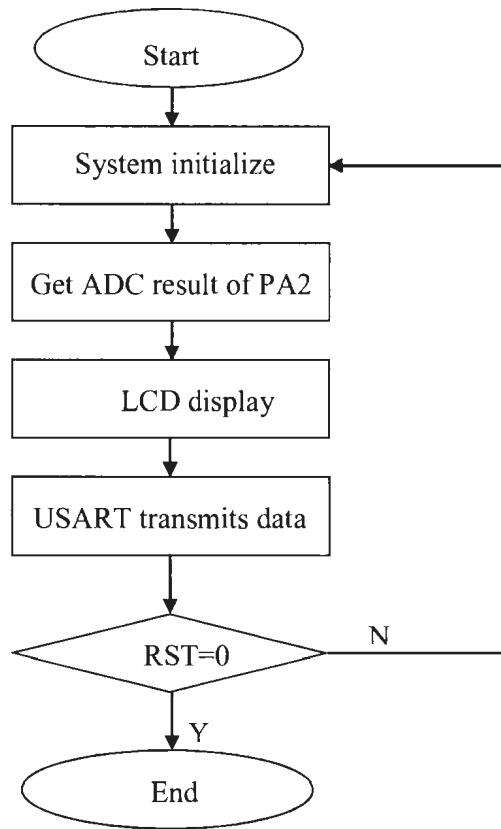
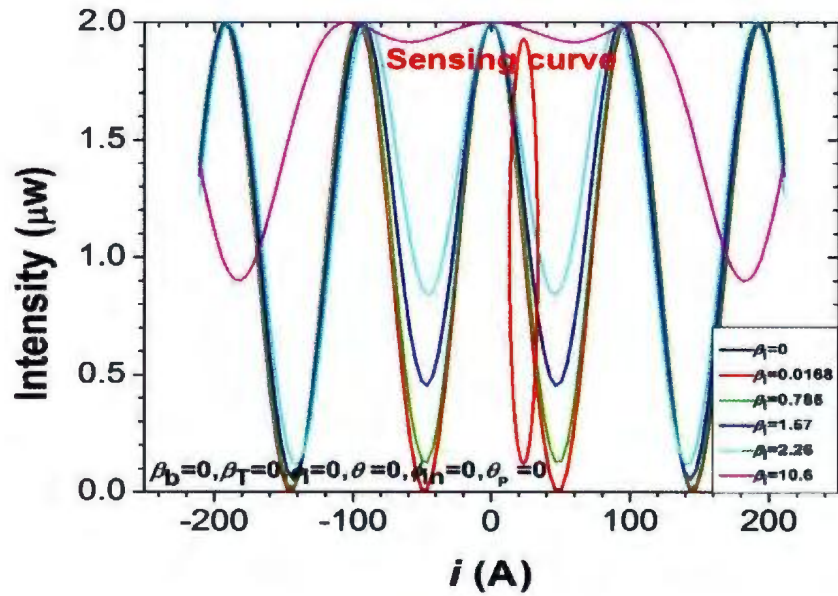
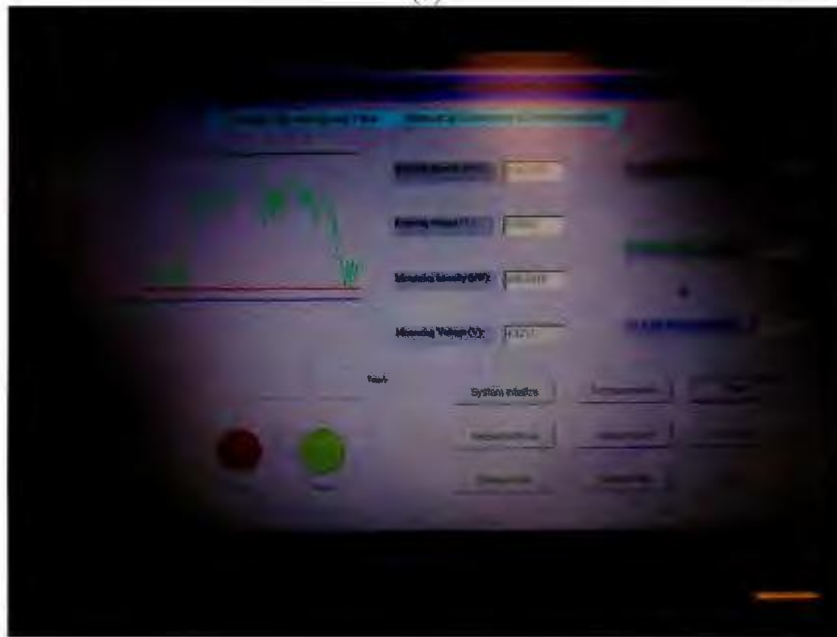


Figure 5-10 Program flow chart of lower machine controlling unit

## 5.4 Performance of a wireless FOCS sensing system



(a)



(b)

Figure 5-11 In-situ test of a wireless FOCS sensing system: (a) sensing curve of basic scheme; (b) an application in remote monitoring of electrical current

A practical test result of wireless FOCS sensing system is shown in Figure 5-11 with an application in remote monitoring of electrical current by employing the sensing curve of the basic scheme.

## Chapter 6 Conclusions

### 6.1 Conclusions

Fiber-optic current sensors have potential applications in metering, electro-chemistry, circuit breakers or bushings, railways, and control and protection in high voltage substations as a result of its exponentially reduced size and weight, ease of installation and low cost, wide sensing range, and immune to electromagnetic interference. Incorporation of wireless data communication with fiber-optic current sensor system will significantly enhance the capability of the sensing system with remote monitoring. Starting with a review on the research on FOCS in this thesis, an in-depth study of FOCS in basic scheme and reflective scheme to measure direct current and the dependences of sensitivity and linearity on experimental parameters have been carried out. We succeeded in the design and testing of a wireless FOCS sensing system with Zigbee modules.

The investigation in the basic scheme in Chapter 3 shows that: (1) The intrinsic and bend-induced birefringence degrades the sensitivity and linearity of the sensing curve at lower current range while a high sensitivity exists in the larger current range, demonstrated in sections 3.3.1, 3.3.2, and 3.4.1. (2) Sufficient amount of twist-induced birefringence can help maintain an excellent sensitivity and linearity by shifting the sensing curve, concluded from sections 3.3.3 and 3.4.2. (3) Elliptical and circular initial input SOPs degrade the sensitivity and linearity while a pre-polarizer can be employed to stabilize the linear input SOP to improve the sensitivity and linearity of sensing curve, derived from sections 3.3.4 and 3.4.3. (4) The orientation of linear initial input SOP has

no effect on the sensitivity and linearity of the sensing curve, however, the different orientation angle shifts the sensing curve which results the measurement in a large range of electrical current, demonstrated in sections 3.3.4, 3.5.2, and 3.5.3.

The research on FOCS in the reflective scheme in Chapter 4 demonstrates the following results: (1) Certain amount of deviation from a perfect retarder reduces the sensitivity and linearity. (2) Certain amount of deviation from critical connecting azimuth degrades the sensitivity. (3) Sufficient amount of connecting azimuth can maintain an excellent sensitivity and linearity. (4) A long PM fiber helps to stabilize the detected light intensity.

The design of wireless FOCS sensing system in Chapter 5 is divided into hardware design comprising of sensor node, lower machine controlling unit, multiple data interfaces, and host computer service platform and software design including the host computer service platform and the microprocessor controlling program. A demonstration system has been built with a Zigbee coordinator and a Zigbee router (end device). In-situ performance of the wireless FOCS sensing system has verified the design and demonstrated a good reliability and repeatability in monitoring DC in real time.

## **6.2 Future work**

Additional work could be carried out in the investigation of FOCS in the following aspects:

(1) Further study on the improvement of SNR could be conducted to enhance the sensing signal, especially, when the sensing signal is detected in optical intensity. The

SNR is mainly degraded by Rayleigh scattering and the end reflections in optical paths [1, 123, 124].

(2) Investigation of wireless FOCS sensing system to measure AC could be carried out to improve measuring accuracy and SNR. The sensing signal of alternating current can be modulated and demodulated by a phase-modulation system [125, 126].

(3) Design and achieve wireless FOCS sensor network by employing the wireless sensor network (WSN) technique, shown in Figure 6-1. This wireless FOCS sensor network enables the practical applications of FOCS in industrial monitoring and measurement of AC and DC from in a remote approach [127].

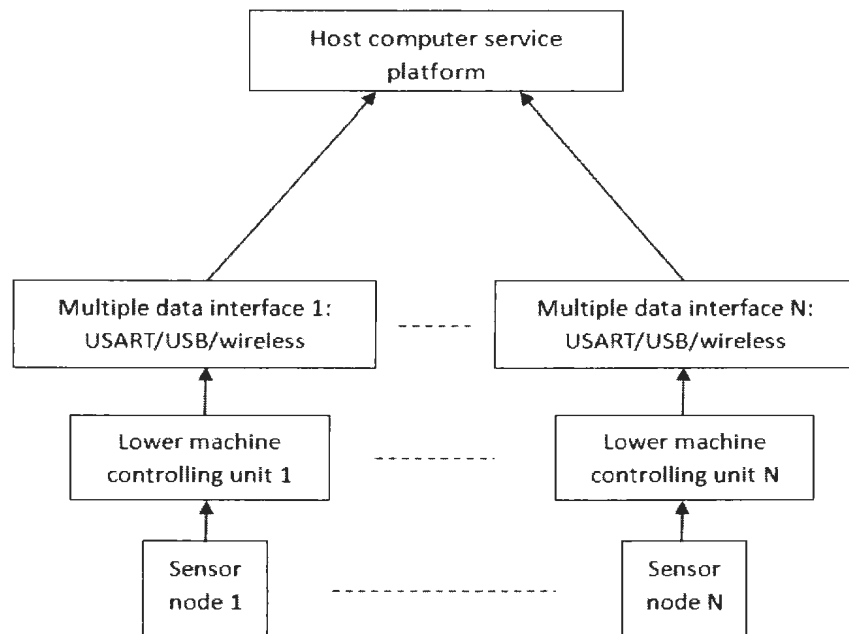


Figure 6-1 Wireless fiber-optic current sensor network

## Publication List

Part of this thesis work has been given in three conference presentations. Some manuscripts for journal submissions based on the results obtained in this thesis will be prepared.

[1] Chuantai Shi and Qiyong Chen, Fiber optic sensors for measurement of electrical current, Photonics North 2013, Ottawa, Canada (June 2013).

[2] Liqiu Men, Xiaojian Zhu, Chuantai Shi, and Qiyong Chen, Tapered optical fibers with surface Plasmon resonance effects, Photonics North 2013, Ottawa, Canada (June 2013).

[3] Chuantai Shi and Qiyong Chen, Faraday magneto-optic effect in an optical fiber and its applications, IEEE Newfoundland Electrical and Computer Engineering Conference (NECEC) 2012, St. John's, Canada (November, 2012).

## References

- [1] Jia-Ming Liu, *Photonic Devices*, Cambridge University Press, 2005.
- [2] S. Ziegler, R. C. Woodward, and H. H. Lu, "Current Sensing Techniques: A Review, *IEEE Sensors Journal*", Vol. 9, No. 4, April 2009, pp.354-376.
- [3] C. M. Johnson and P. R. Palmer, "Current measurement using compensated coaxial shunts," *Proc. IEE Sci., Measure. Technol.*, vol. 141, 1994, pp.471-480.
- [4] J. A. Ferreira, W. A. Cronje, and W. A. Relihan, "Integration of high frequency current shunts in power electronic circuits", *IEEE Trans. Power Electron.*, Vol. 10, 1995, pp. 32-37.
- [5] R. Malewski, "New device for current measurement in exploding wire circuits", *Rev. Scient. Instruments*, Vol. 39, 1968, pp. 90-94.
- [6] R. Malewski, C. T. Nguyen, K. Feser, and N. Hylten-Cavallius, "Elimination of the skin effect error in heavy-current shunts", *IEEE Trans. Power Apparatus and Systems*, Vol. Pas-100, 1981, pp. 1333-1340.
- [7] F. Castelli, "The flat strap sandwich shunt", *IEEE Trans. Instrument. Measure.*, Vol. 48, 1999, pp. 894-898.
- [8] E. Dallago, M. Passoni, and G. Sassone, "Lossless current sensing in low-voltage high-current DC/DC modular supplies", *IEEE Trans. Ind. Electron.*, Vol. 47, 2000, pp. 1249-1252.
- [9] W. F. Ray and C. R. Hewson, "RCTrms Rogowski coil datasheet Power Electronic Measurements Ltd.", 2005, [Online]. Available: <http://www.pemuk.com>
- [10] W. F. Ray and C. R. Hewson, "High performance Rogowski current transducers", in *Proc. IEEE Ind. Appl. Conf.*, Rome, Italy, 2000, pp. 3083-3090.
- [11] D. A. Ward and J. L. T. Exon, "Using Rogowski coils for transient current measurements," *Eng. Sci. Education J.*, vol. 2, 1993, pp. 105-113.
- [12] E. Udd, and W. B. Spillman, "An Introduction for Engineers and Scientists", *J. Fiber Optic Sensors*, 2nd edition, John Wiley & Sons, Inc. 2011.
- [13] Optical Society of America, 2011, [Online]. Available: <http://velma.library.mun.ca/uhtbin/cgiisirs/cWbCMAgIhh/QEII/44260114/9>

- [14] P. A. Tipler, "An introduction to the Hall effect", Bell Technologies, Inc., 2005, [Online]. Available: <http://www.fwbell.com>
- [15] P. A. Tipler, "Understanding Hall effect devices", Bell Technologies, Inc., 2005, [Online]. Available: <http://www.fwbell.com>
- [16] R. S. Popovic, Z. Randjelovic, and D. Manic, "Integrated Hall-effect magnetic sensors," *Sens. Actuators A: Physical*, Vol. 91, 2001, pp. 46–50.
- [17] J. Lenz and A. S. Edelstein, "Magnetic sensors and their applications," *IEEE Sensors J.*, vol. 6, 2006, pp. 631–649.
- [18] Y.N. Ning, Z.P. Wang, A.W. Palmer, K.T.V. Grattan and D.A.Jackson, "Recent progress in optical current sensing techniques", *Rev. Sci. Instrum.* 66, 1995, pp. 3097-3111.
- [19] G.W. Day, "Recent advances in Faraday Effect sensors", in H.J. Arditty, J.P. Dakin and K.Th. Kersten (eds.), *Springer Proceedillgs in Physics*, Vol. 44, *Optical Fiber Sensors*, Springer, Berlin, 1989, pp. 250-254.
- [20] A.J. Rogers, "Optical technique for measurement of current at high voltage", *Proc. IEE*, 120, 1973, pp.261-267.
- [21] K. Bohnert, P. Gabus, J. Nehring, H. Brändle, and M. G. Brunzel, "Fiber-optic current sensor for electrowinning of metals," *J. Lightwave Technol.*, Vol. 25, 2007, pp. 1–8.
- [22] S. B. Berger et al., "Faraday rotation of rare-earth (III) phosphate glasses", *Phys. Rev.*, 133(3A), 1964, pp. 723–A727.
- [23] R. Ulrich and A. Simon, "Polarisation optics of twisted single-mode fibres", *Appl. Opt.*, 18, 1979, pp. 2241-2251.
- [24] R.I. Laming and D.N. Payne, "Electric current sensors employing spun highly birefringent optical fibers", *IEEE J. Lightwave Technol.*, LWT-7, 1989, pp. 2084-2094.
- [25] G.W. Day and S.M. Etzel, "Annealing of bend induced birefringence in fiber current sensors", *Integrated Optics Optical Fiber Commun.-European Optical Commun.*, Vellice, 1985, pp. 871-874.
- [26] Z.B. Ren and Ph. Robert, "Input polarization coding in fiber current sensors", *Springer Proceedings in Physics*, Vol. 44, *Optical Fiber Sensors*, Springer, Berlin, 1989, pp. 261.

- [27] A. Ben-Kish, M. Tur and E. Shafir, "Geometrical separation between the birefringence components in Faraday-rotation fiber optic current sensors", *Opt. Lett.*, Vol. 16, 1991, pp. 687-689.
- [28] H. Ahlers and Th. Bosselmann, "Complete polarization analysis of a magneto-optic current transformer with a new polarimeter", *Proc. 7th Optical Fiber Sensors Conf.*, Sydney, Australia, 1990, pp. 81-84.
- [29] W. Chu, D. McStay and A.J. Rogers, "Current sensing by mode coupling in fiber via the Faraday effect", *Electron. Lett.*, 27, 1991, pp. 207.
- [30] A.D. Kersey and M.A. Davis, "AU-fiber Faraday rotation current sensor with remote laser-FM based heterodyne detection", *Springer Proceedings in Physics*, Vol. 44, *Optical Fiber Sensors*, Springer, Berlin, 1989, pp. 285-290.
- [31] P.A. Leilabady, A. P. Wayte, M. Berwick, J.D. Jones and D.A. Jackson, "A pseudo-reciprocal fiber-optic Faraday rotation sensor: current measurement and data communication applications", *Opt. Commun.*, 59, 1986, pp. 173.
- [32] N.C. Pistoni and M. Martinelli, "Vibration-insensitive fiber-optic current sensor", *Opt. Lett.*, 18, 1993, pp.314-316.
- [33] K. Kurosawa, S. Yoshida, K. Sakamoto, I. Masuda and T. Yamashita, "Optical fiber-type current sensor utilizing the Faraday effect of the flint glass fibre". *IE Proc.*, Vol. 2360, 1994, pp. 24-27.
- [34] X. Ma, C. Luo, "A Method to Eliminate Birefringence of A Magneto-optic AC Current Transducer With Glass Ring Sensor Head", *IEEE Transactions on Power Delivery*, Vol. 13, No. 4, October 1998, pp.1015-1019.
- [35] L. Sun, S. Jiang and J. R. Marciante, "All-fiber optical magnetic-field sensor based on Faraday rotation in highly terbium-doped fiber", *Optics Express*, Vol. 18, No. 6, 15 March 2010, pp. 5407-5412.
- [36] H. J. El-Khozondar<sup>1</sup>, M. S. Müller, R. J. El-Khozondar and A. W. Koch, "Influence of Magnetic Field Inhomogeneity on a Magneto-Optical Current Sensor", *Journal of Sensor Technology*, 2012, pp. 19-22.
- [37] T. Sato et al., *Eur. Patent*, App. No. 83 102 210 B, 1983.
- [38] M. Kanoi, G. Takahashi, T. Sato, M. Higaki, E. Mori, K. Okumura, "Optical voltage and current measuring system for electric power system", *IEEE Trans. Power Delivery*, PWRD-1, 1986, pp.91-97.

- [39] B.C.B. Chu, Y.N. Ning and D.A. Jackson, "Faraday current sensor that uses a triangular-shaped bulk-optical sensing element", *Opt. Lett.*, 17, 1992, pp.1167-1169.
- [40] Y.N. Ning and D.A. Jackson, "Faraday Effect optical current clamp using a bulk-glass sensing element", *Opt. Lett.*, 18, 1993, pp. 835-837.
- [41] Y.N. Ning, B.C.B Chu and D.A. Jackson, Miniature Faraday current sensor.
- [42] Montserrat Fernandez-Vallejo and Manuel Lopez-Amo, "Optical Fiber Networks for Remote Fiber Optic Sensors", *Sensors*, doi:10.3390/s120403929, 2012, pp. 3929-3951.
- [43] J. Hu; Z. Chen; C. Yu, "150-km long distance FBG temperature and vibration sensor system based on stimulated Raman amplification". *IEEE J. Lightw. Technol.* 2011, doi: 10.1109/JLT, 2011, pp. 1237 -1243.
- [44] M. Bravo, M. V. Fernández, and M. Lopez-Amo, "Hybrid OTDR-fiber laser system for remote sensor multiplexing", *IEEE Sens. J.* 2012, 12, pp. 174–178.
- [45] Y.G. Han, "A long-distance remote sensing technique using a multiwavelength Raman fiber laser based on fiber Bragg gratings embedded in a quartz tube". *IEEE Sens. J.*, 2011, 11, pp. 1152–1156.
- [46] M. Bravo, J.M. Baptista, J.L. Santos, M. Lopez-Amo, and O. Frazão, "Ultralong 250 km remote sensor system based on a fiber loop mirror interrogated by an optical time-domain reflectometer". *Opt. Lett.* Vol. 36, 2011, pp. 4059–4061.
- [47] M. Fernandez-Vallejo, S. Rota-Rodrigo, M. Lopez-Amo, "Remote (250 km) fiber Bragg grating multiplexing system". *Sensors*, 2011, 11, pp. 8711–8720.
- [48] D. Leandro, A. Ullan, M. Lopez-Amo, J.M. Lopez-Higuera, and Loayssa, A. "Remote (155 km) fiber Bragg grating interrogation technique combining Raman, brillouin and erbium gain in a fiber laser". *IEEE Photonics Technol. Lett.*, Vol 23, 2011, pp. 621–623.
- [49] M. Fernandez-Vallejo, D. Leandro, A. Loayssa, and M. Lopez-Amo, "Fiber Bragg grating interrogation technique for remote sensing (100 km) using a hybrid brillouin-Raman fiber laser". *Proc. SPIE 2011*, 2011, doi: 10.1117/12.882556, 7753.
- [50] J. Hu, Z. Chen, X. Yang, J. Ng, and C. Yu, "100-km Long distance fiber Bragg grating sensor system based on erbium-doped fiber and Raman amplification". *IEEE Photonics Technol. Lett.* Vol. 22, 2010, pp. 1422–1424.

- [51] M. Fernandez-Vallejo, S. Díaz, R. A. Perez-Herrera, D. Passaro, S. Selleri, M. A. Quintela, J. M. López Higuera and M. Lopez-Amo, "Resilient long-distance sensor system using a multiwavelength Raman laser". *Meas. Sci. Technol.* Vol. 21, 2010, 094017:1–094017:5.
- [52] M. Fernandez-Vallejo, R. A. Perez-Herrera, D. Passaro, M. A. Quintela, J. M. López Higuera, M. Lopez-Amo, "Resilient long-distance sensor system using a multiwavelength Raman laser". *Proc. SPIE* 2009, 2009, doi: 10.1117/12.833524, 7503.
- [53] Y. Han, "Long-distance Remote sensors for simultaneous measurement of strain and temperature based on multiwavelength fiber lasers". *Proc. SPIE* 2009, 2009, 7503 doi: 10.1117/12.83, 7631.
- [54] R.A. Perez-Herrera, R.A. Perez-Herrera, S. Diaz, M. Fernández-Vallejo, M. López-Amo, M.A. Quintela, J.M. Lopez-Higuera, "Switchable multi-wavelength erbium-doped fiber laser for remote sensing". *Proc. SPIE* 2009, 7503, doi: 10.1117/12.835134.
- [55] T. Saitoh, K. Nakamura, Y. Takahashi, H. Iida, Y. Iki, and K. Miyagi, "Ultra-long-distance (230 km) FBG sensor system". *Proc. SPIE* 2008, 7004, 70046C-4.
- [56] C. Daru, S. Chester, and S. He, "Multiple fiber Bragg grating interrogation based on a spectrumlimited fourier domain mode-locking fiber laser". *Opt. Lett.* 2008, 33, 1395–1397.
- [57] T. Saitoh, K. Nakamura, Y. Takahashi, H. Iida, Y. Iki, and K. Miyagi, "Ultra-long-distance fiber Bragg grating sensor system". *IEEE Photonics Technol. Lett.* 2007, 19, 1616–1618.
- [58] Y. Rao, Z. Ran, and R. Chen, "Long-distance fiber bragg grating sensor system with a high optical signal-to-noise ratio based on a tunable fiber ring laser configuration". *Opt. Lett.* 2006, 31, pp. 2684–2686.
- [59] S. Diaz, and M. Lopez-Amo, "Comparison of wavelength-division-multiplexed distributed fiber Raman amplifier networks for sensors". *Opt. Express* 2006, 14, pp. 1401–1407.
- [60] P. Peng, K. Feng, W. Peng, H. Chiou, C. Chang, S. Chi, "Long-distance fiber grating sensor system using a fiber ring laser with EDWA and SOA". *Opt. Commun.* 2005, 252, pp. 127–131.
- [61] Y. Han, T.V.A. Tran, S. Kim, and S. B. Lee, "Multiwavelength Raman-fiber-laser-based long-distance remote sensor for simultaneous measurement of strain and temperature". *Opt. Lett.* 2005, 30, pp. 1282–1284.

- [62] Y. Han, T.V.A. Tran, S. Kim, and S. B. Lep, "Development of a multiwavelength Raman fiber laser based on phase-shifted fiber bragg gratings for long-distance remote-sensing applications". *Opt. Lett.* 2005, 30, pp. 1114–1116.
- [63] S. Diaz, G. Lasheras, and M. Lopez-Amo, "WDM bi-directional transmission over 35 km amplified fiber-optic bus network using Raman amplification for optical sensors". *Opt. Express* 2005, 13, 9666–9671.
- [64] S. Díaz, G. Lasheras, M. Lopez-Amo, P. Urquhart, C. Jauregui, J. M. Lopez-Higuera, "Wavelength-division-multiplexed distributed fiber Raman amplifier bus network for sensors". *Proc. SPIE* 2006, 5855, pp. 242–245.
- [65] J.H. Lee, Y.m. Chang, Y. Han, H. Chung, S.H. Kim, and S.B. Lee, "Raman amplifier-based long-distance remote, strain and temperature sensing system using an erbium-doped fiber and a fiber Bragg grating". *Opt. Express* 2004, 12, pp. 3515–3520.
- [66] P. Peng, H. Tseng, and S. Chi, "Long-distance FBG sensor system using a linear-cavity fiber Raman laser scheme". *IEEE Photonics Technol. Lett.* 2004, 16, pp. 575–577.
- [67] Y. Nakajima, Y. Shindo, Y. and T. Yoshikawa, "Novel concept as long-distance transmission FBG sensor system using distributed Raman amplifier". *Proc. SPIE* 2003, pp. 530–533.
- [68] E.L. Esteban, M.S. Alejandro, V.A. Javier, G.H. Joan, and M. S. Josemaria, "Wireless communications deployment in industry: a review of issues, options and technologies", *Computers in Industry* 56, 2005, pp. 29–53
- [69] S. Redl, M.K. Weber, and M. Oliphant, "An Introduction to GSM", The Artech House Mobile Communications, 1995.
- [70] ETSI publications download area 2013, [Online], available: <http://pda.etsi.org/pda/queryform.asp>.
- [71] E.A. Lee, and D.G. Messerschmitt, "Digital Communication", second ed. Kluwer Academic Publishers, 1993.
- [72] H. Holma, and A. Toskala, "WCDMA for UMTS", second ed. Wiley, 2002
- [73] IEEE 802.11, "Wireless LAN Medium Access Control and Physical Layer Specifications", 1999.
- [74] ETS 300652 V1.2.1, "Broadband Radio Access Networks (BRAN); High Performance Radio Local Area Network (HIPERLAN) Type I", Functional Specification, July 1998.

- [75] Extronics iWAP 100 Homepage, 2013, [Online], available:  
<http://www.extronics.com/Product.asp?ProductID=792>.
- [76] IR Data Association Specifications, 2013, [Online], available:  
<http://www.irda.org/standards/specifications.asp>.
- [77] A. Karnik, A. Kumar, "Performance Analysis of the Bluetooth Physical Layer", IEEE International Conference on Personal Wireless Communications, 2000, pp. 70–74.
- [78] C. Yeh. "Handbook of fiber optics", Academic Press Inc., 1988
- [79] Jun Song, "Development of Magneto-optical Current Transducers for Power Systems", Ph.D Thesis, University of Manitoba, January 1996.
- [80] R.C. Jones. "A New Calculus for the Treatment of Optical Systems". J. Opt. Soc. Am.. vol. 31. July 1941. pp. 488-493.
- [81] D. Clarke and J.F. Grainger. "Polarized Light and Optical Measurement", Pergamum Press, 1971.
- [82] W. A. Shurcliff and S.S. Ballard. "Polarized Light", D. Van Nostrand Company. inc., 1964.
- [83] Peng-Gang Zhang, "Faraday Effect Optical Current Sensor". Master's Thesis, University of Calgary, August 1993.
- [84] J. L. Cruz, M. V. Andres, and M. A. Hernandez, "Faraday effect in standard optical fibers: dispersion of the effective Verdet constant", Applied Optics, Vol. 35, No. 6, 20 February 1996, pp. 922-927.
- [85] K. Bohnert, P. Gabus, J. Nehring, H. Brändle, and M.G. Brunzel, "Fiber-Optic Current Sensor for Electrowinning of Metals", IEEE J. Lightw. Technol Vol. 25, No. 11, November 2007, pp. 3602-3609.
- [86] S. C. Rashleigh, "Origins and Control of Polarization Effects in Single-Mode Fibers", J. Lightw. Technol., Vol. LT-1, NO.2, June 1983, pp. 312-330.
- [87] D. N. Payne, A. J. Barlow, and J. J. Hansen, "Development of low and high birefringence optical fibers", IEEE J. Quantun Electron., vol. 18, 1982, pp.477-488.
- [88] S. C. Rashleigh and R. Ulrich, "Magneto optic current sensing with birefringent fibers", Appl. Phys. Lett., Vol. 34, No.11, June 1979, pp. 372-382.

- [89] W. J. Tabor and F. S. Chen, "Electromagnetic Propagation through Materials Possessing both Faraday rotation and Birefringence: Experiments with Ytterbium Orthoferrite", *J. Appl. Phys.* 40, 1969, pp.2760-2765.
- [90] L.G. Chandler, P. R. Forman, F. C. Jahoda, and K. A. Klare, "Fiber-optic heterodyne phase-shift measurement of plasma current", *Appl. Opt.*, Vol. 25, No.11, 1 June 1986, pp.1364.
- [91] P. R. Forman and F. C. Jahoda, "Linear birefringence effects on fiber-optic current sensors", *Appl. Opt.*, Vol. 27, No. 15, 1 August 1988, pp. 3088-3096.
- [92] S. P. Bush and D. A. Jackson, "Numerical investigation of the effects of birefringence and total internal reflection on Faraday effect current sensors", *Appl. Opt.*, Vol. 31, No. 25, 1 September 1992, pp. 5366-5374.
- [93] F. Wen, B.J. Wu, C.Z. Li, S.J Wu, and S. Perumal, "Magnetic field response of erbium-doped magneto-opticfiber Bragg grating", *Optical Engineering* 51(6), 064402, June 2012, pp. 1117.
- [94] G.652.D : Characteristics of a single-mode optical fibre and cable, 2008, retrieved from: <http://www.itu.int/rec/T-REC-G.652/en>.
- [95] Corning fiber, SMF28E optical fiber product information, 2005, retrieved from: [http://www.tlc.unipr.it/cucinotta/cfa/datasheet\\_SMF28e.pdf](http://www.tlc.unipr.it/cucinotta/cfa/datasheet_SMF28e.pdf).
- [96] M. Yasi, "Recent Progress in Optical Fiber Research", InTech, ISBN 978-953-307-823-6, January 2012.
- [97] P. R. Forman and F. C. Jahoda, "Linear birefringence effects on fiber-optic current sensors", *Appl. Opt.*, Vol. 27, No. 15, 1 August 1988, pp. 3088-3096.
- [98] R. M. Silva, H. Martins, I. Nascimento, J. M. Baptista, A.L. Ribeiro, J. L. Santos, P. Jorge and O. Frazão, "Optical Current Sensors for High Power Systems: A Review", *Appl. Sci.* 2012, pp.602-628.
- [99] T.G. Giallorenzi, J.A. Bucaro, A. Dandridge, G.H. Sigel, J.H. Cole, S.C. Rashleigh, R.G. Priest, "Optical Fiber Sensor Technology", *IEEE Transaction on Microwave Theory and Techniques*, Vol.30, No. 4, April 1982, pp. 626-665.
- [100] G. A. Sanders, J. N. Blake, A. H. Rose, F. Rahmatian, and C. Herdman, "Commercialization of Fiber-Optic Current and Voltage Sensors at NxtPhase," 15th Optical Fiber Sensors Conference, Portland, OR, May 2002, pp. 31-34.
- [101] J. Blake, P. Tantaswadi, R. T. de Carvalho, "In-line Sagnac interferometer current sensor," *IEEE Trans. Power Delivery*, vol. 11, Jan. 1996, pp. 116-121.

- [102] J. N. Blake and A. H. Rose, "Fiber-Optic Current Transducer Optimized for Power Metering Applications," Proceedings of the IEEE T&D meeting, Dallas, TX, Sept. 2003, pp. 1-4.
- [103] E. So, R. Arseneau, and D. Bennett, "A current-comparator-based system for calibration of optical instrument transformers with analog and digital outputs," in Dig. CPEM 2002, Ottawa, ON, Canada, Jun. 2002, Dig. No. 02CH37279, pp. 252.
- [104] E. So, "The application of the current comparator technique in instrumentation and measurement equipment for the calibration of nonconventional instrument transformers with non standard rated outputs," IEEE Trans. Power Del., Vol. 7, No. 1, Jan. 1992, pp. 46-52.
- [105] G. Frosio and R. Dandliker, "Reciprocal reflection interferometer for a fiber-optic Faraday current sensor", Appl. Opt., Vol. 33, No. 25, 1 September 1994, pp. 1364.
- [106] K. Bohnert, Member, OSA, P. Gabus, J. Nehring, and H. Brändle, "Temperature and Vibration Insensitive Fiber-Optic Current Sensor", J. Lightwave Technol., Vol. 20, No. 2, Feb. 2002, pp. 267-276.
- [107] R. M. Silva, H. Martins, I. Nascimento, J.M. Baptista, A.L. Ribeiro, J. L. Santos, P. Jorge, and O. Frazão, "Optical Current Sensors for High Power Systems: A Review", Appl. Sci. 2, doi:10.3390, app2030602, July 2 2012, pp.602-628.
- [108] R. Dandliker, "Rotational effects of polarization in optical fibers," in Anisotropic and Nonlinear Optical Waveguides, G. Stegeman and C. Someda, eds. (Elsevier, Amsterdam, 1992), pp. 39-76.
- [109] K. Bohnert, P. Gabus, J. Nehring, H. Brändle, and M. Georg Brunzel, "Fiber-Optic Current Sensor for Electrowinning of Metals", J. Lightwave Technol., Vol. 25, No. 11, November 2007, pp. 3602-3609.
- [110] M. Wegmuller, M. Legre, and N. Gisin, "Distributed Beatlength Measurement in Single-Mode Fibers with Optical Frequency-Domain Reflectometry", J. Lightwave Technol., Vol.20, No.5, May 2002, pp. 828-835.
- [111] M.S. Ab-Rahman, M.K. Mat, and K. Jumari, "Wireless Optical Sensor Network (Wosn) for Optical Line Monitoring and Restoration in FttH", Journal of Applied Sciences Research, 7(4), 2011, pp. 400-408.
- [112] V.M. Akyildiz, "Wireless Sensor Networks, First ed.", John Wiley and Sons, Ltd, 2010.
- [113] R. Iniguez and R. Green, "Indoor Optical Wireless Communications," presented at the Optical Wireless Communications, IEE Savoy Place, London, U.K., 1999.

- [114] C.K Chan, F. Tong, L.K Chen, K.P Ho, D. Lim, "Fiber-fault identification for branched access networks using a wavelength sweeping monitoring source". IEEE Photon Technol. Lett., 11(5), 1999, pp. 614-616.
- [115] J. Prat, "Optical networks: towards bandwidth manageability and cost efficiency". 2008. [Online] Available: [http://cordis.europa.eu/fetch?CALLER=FP6\\_PROJ&ACTION=D&DOC=4780&CAT=PROJ&QUERY=1170700839507&RCN=74614](http://cordis.europa.eu/fetch?CALLER=FP6_PROJ&ACTION=D&DOC=4780&CAT=PROJ&QUERY=1170700839507&RCN=74614)
- [116] T. Koonen, "Fiber to the home/fiber to the premise: what, where, and when?" Proceedings IEEE, 2006, pp. 911-934
- [117] K.L. Lee, S.B. Kang, D.S. Lim, H.K. Lee, and W.V. Sorin, "Fiber link loss monitoring scheme in bidirectional WDM transmission using ASE-injected FP-LD". IEEE Photon Technol. Lett., 18(3), 2006, pp. 523-525.
- [118] M.S.A. Rahman, B.C. Ng, A. Premadi, and K. Jumari, "Transmission surveillance and self-restoration against fibre fault for time division multiplexing using passive optical network". IET Journals, 3(12), 2009b, pp. 1896-1906.
- [119] A. Tan, "FTTH in Malaysia", 2012, [Online] Available: <http://thedaneshproject.com/posts/ftth-in-malaysia>.
- [120] Meshnetics, "Zigbee Faq: What Topologies are supported by ZigBee?", 2009, [Online] Available: <http://www.meshnetics.com/zigbee-faq/>.
- [121] "ZigBit™ 2.4 GHz Wireless Modules ATZB-24-A2/B0 Datasheet", 2009, [Online]. Available: [http://www.atmel.com/dyn/resources/prod\\_documents/doc8226.pdf](http://www.atmel.com/dyn/resources/prod_documents/doc8226.pdf)
- [122] "ZigBit™ Development Kit 2.3 User's Guide". 2012, [Online]. Available: [http://www.meshnetics.com/netcat\\_files/Image/S-ZDK451\(ZigBit%20Development%20Kit%20Users%20Guide\).pdf](http://www.meshnetics.com/netcat_files/Image/S-ZDK451(ZigBit%20Development%20Kit%20Users%20Guide).pdf)
- [123] D. A Jackson, "An optical system with potential for remote health monitoring of subsea machinery". Meas. Sci. Technol. 2009, 20, pp. 1-8.
- [124] C. D. Perciante, and J.A. Ferrari, "Magnetic crosstalk minimization in optical current sensors". IEEE Trans. Instrum. Meas. 2008, 57, pp. 2304-2308.
- [125] P. Ripka, "Electric current sensors: A review". Meas. Sci. Technol. 2010, 21, pp. 1-23.
- [126] X. Y. Deng, Z. Li, P. Qixian, J. Liu, and J. Tian, "Research on the magneto-optic current sensor for high current pulses". Rev. Sci. Instru. 2008, 79, pp. 1-4.

[127] R. M. Silva, H. Martins, I. Nascimento, J. M. Baptista, A.L. Ribeiro, J. L. Santos, P. Jorge and O. Frazão, "Optical Current Sensors for High Power Systems: A Review", *Appl. Sci.* doi:10.3390, app2030602, 2012, 2, pp. 602-628.

## Appendix A Service program of host computer

The follow text is the Service program of host computer based on Microsoft Visual Basic 6.0.

### 1. Program code of main interface (Form1)

\*\*\*\*\* Define public variables to transfer values between form1 and form2 \*\*\*\*\*

```
Public intensity_ref As Single, voltage_ref As Single, current_up As Single, current_low  
As Single, zyl_high As Integer, zyl_low As Integer, kxs_high As Integer, kxs_low As  
Integer, yxyl_high As Integer, yxyl_low As Integer, datamax As Integer
```

\*\*\*\*\* Define variables in form1 \*\*\*\*\*

```
Dim intensity_mes As Single, voltage_mes As Single, current_mes As Single, zyl() As  
String, kxs() As String, yxyl() As String, s As String, zyl_i As Integer, kxs_i As Integer, i  
As Integer, m As Integer, n As Integer, max As Integer, before_ubound As Integer,  
after_ubound As Integer, picx As Single, picy_zyl As Single, picy_kxs As Single,  
picy_yxyl As Single
```

\*\*\*\*\* System initializes command subroutine Command1 \*\*\*\*\*

```
Private Sub Command1_Click()
```

```
If Timer1.Enabled = True Then Timer1.Enabled = False 'diableTimer1
```

```
s = "": i = 0 ' clear s , set i=0
```

```

m = 0: n = 0: max = 0          ' set initial values m, n, and max=0

before_ubound = 0: after_ubound = 0    ' set initial values

Picture1.Cls: picx = 0: picy_zyl = 0: picy_kxs = 0: picy_yxyl = 0 ' set initial values

Text1 = "": Text2 = "": Text3 = "": Text4 = "": Text5 = "": Text6 = "": Text7 = ""    '

clear Text

ReDim zyl(1): ReDim kxs(1): ReDim yxyl(1)          ' set initial values

zyl_low = 100          ' set initial values

zyl_high = 1000

kxs_low = 100

kxs_high = 1000

yxyl_low = 100

yxyl_high = 1000

datamax = 100

intensity_ref = 5

voltage_ref = 1

current_up = 1.5

current_low = 0.5

exp_scheme = "b"

fitting_k = -1

```

```

fitting_b = 5

Shape1.FillColor = RGB(255, 255, 255) ' set initial while color for "working state",
"safe", "dangerous", "timeout"

Shape2.FillColor = RGB(255, 255, 255)

Shape3.FillColor = RGB(255, 255, 255)

Shape4.FillColor = RGB(255, 255, 255)

End Sub

"""""""""" Go to set parameters command subroutine Command2 """"""""""

Private Sub Command2_Click()

Form1.Hide      'Hide Form1

Form2.Show      'Show Form2

End Sub

"""""""""" Start command subroutine Command3 """"""""""

Private Sub Command3_Click()

Timer1.Enabled = True 'Enable Timer1

End Sub

```

\*\*\*\*\* Pause/Continue command subroutine Command4 \*\*\*\*\*

Private Sub Command4\_Click()

Timer1.Enabled = Not Timer1.Enabled 'Timer1 initialize

End Sub

\*\*\*\*\* End command subroutine Command9 \*\*\*\*\*

Private Sub Command9\_Click()

MSComm1.PortOpen = False 'Close MSComm port

End ' End process

End Sub

\*\*\*\*\* Load form command subroutine \*\*\*\*\*

Private Sub Form\_Load()

MSComm1.CommPort = Val(Trim(InputBox("Please set COM port:"))) ' Input Com port  
for MSComm1series data communication

MSComm1.PortOpen = True 'open MSComm port

End Sub

\*\*\*\*\* Timer1 process subroutine \*\*\*\*\*

```

Private Sub Timer1_Timer()

start:          'start mark, process can go back here

s = Trim(MSComm1.Input)  's gets data from SComm1.Input

If Len(s) > 0 And Mid(s, 5, 1) <> "" Then 'verify if the fifth byte is num

    Shape1.FillColor = RGB(0, 0, 255)    'blue light of "working state"

    before_ubound = UBound(kxs) + UBound(zyl) 'sum data number

    If Mid(s, 1, 1) = "Z" And UBound(zyl) <= UBound(kxs) And zyl(UBound(zyl)) = ""
Then 'verify if time is out

        zyl_i = UBound(zyl)                'get data

        zyl(zyl_i) = Mid(s, 2, 4)

        ReDim Preserve zyl(zyl_i + 1)

    ElseIf Mid(s, 1, 1) = "K" And UBound(zyl) >= UBound(kxs) And kxs(UBound(kxs)) =
"" Then ' verify if time is out

        kxs_i = UBound(kxs)                'get data

        kxs(kxs_i) = Mid(s, 2, 4)

        ReDim Preserve kxs(kxs_i + 1)

    Else

        If Timer1.Enabled = True Then GoTo start 'if time is not out go to start mark and
continue to acquire data

```

```

End If

after_ubound = UBound(kxs) + UBound(zyl) ' sum total data number

If (UBound(zyl) >= 3 Or UBound(kxs) >= 3) And after_ubound > before_ubound And
(after_ubound Mod 2 <> 0) Then ' verify if time is out

    m = UBound(zyl)

    n = UBound(kxs)

    If m >= n Then

        max = m

    Else

        max = n

    End If

    yxyl(max - 2) = Val(zyl(max - 2)) - Val(kxs(max - 2)) ' calculate light intensity

    voltage_mes = Val(kxs(max - 2)) / 1024 * 5

    intensity_mes = voltage_mes / voltage_ref * intensity_ref

    If exp_scheme = "b" Then

        current_mes = intensity_mes * fitting_k + fitting_b

    ElseIf exp_scheme = "r" Then

        current_mes = (2 * Arccos(Sqr(intensity_mes / intensity_ref))) * fitting_k +
fitting_b

```

End If

Text1.Text = Format(current\_up, "###0.0000") ' display values

Text2.Text = Format(current\_mes, "###0.0000")

Text3.Text = Format(current\_low, "###0.0000")

Text4.Text = Format(intensity\_ref, "###0.0000")

Text5.Text = Format(voltage\_ref, "###0.0000")

Text6.Text = Format(intensity\_mes, "###0.0000")

Text7.Text = Format(voltage\_mes, "###0.0000")

ReDim Preserve yxyl(max - 1)

Call PIC\_LINE(Val(zyl(max - 2)), Val(kxs(max - 2))) ' call draw subroutine

If (max - 2) >= datamax Then Shape4.FillColor = RGB(255, 255, 0) 'if time is out  
"time out" light yellow

If current\_low <= current\_mes And current\_mes <= current\_up Then ' verify if  
monitoring current is safe

Shape2.FillColor = RGB(0, 255, 0) ' "safe" light lights green

Shape3.FillColor = RGB(255, 255, 255) ' "dangerous" light turns off

Else

```

Shape3.FillColor = RGB(255, 0, 0)    "dangerous" lights red

Shape2.FillColor = RGB(255, 255, 255) ' "safe" light turns off

End If

End If

i = 0                                'if data is received, pointer clears

Else

    i = i + 1                          'if data is not received, pointer adds 1

End If

If i >= 20 Then Shape1.FillColor = RGB(255, 255, 255): Text1 = "": Text2 = "": Text3 =
"": Text6 = "": Text7 = "" ' if data is not received for 20 times, "working data" light turns
off

End Sub

```

\*\*\*\*\* Draw line process subroutine \*\*\*\*\*

```

Private Sub PIC_LINE(ByVal X As Long, ByVal Y As Long) ' transfer values

Static y1 As Single, y2 As Single, y3 As Single    ' define static variables

Picture1.DrawWidth = 2                            'set line width 2

If (max - 2) = 1 Then                              'verify if it is the first data, if so draw dot

    picx = 0                                       'set value of x-axis 0

```

```

picy_zyl = 5535 - current_up / 2.2 * 5535      'calculate values of y-axis

picy_kxs = 5535 - current_mes / 2.2 * 5535

picy_yxyl = 5535 - current_low / 2.2 * 5535

Picture1.PSet (picx, picy_zyl), RGB(255, 0, 0)

Picture1.PSet (picx, picy_kxs), RGB(0, 255, 0)

Picture1.PSet (picx, picy_yxyl), RGB(0, 0, 255)

Else                                          'if it is not the first data, draw line

picx = picx + 8175 / datamax      'calculate axes values

y1 = 5535 - current_up / 2.2 * 5535

y2 = picy_kxs

y3 = 5535 - current_low / 2.2 * 5535

picy_zyl = 5535 - current_up / 2.2 * 5535

picy_kxs = 5535 - current_mes / 2.2 * 5535

picy_yxyl = 5535 - current_low / 2.2 * 5535

Picture1.Line (picx - 8175 / datamax, y1)-(picx, picy_zyl), RGB(255, 0, 0) 'draw line

Picture1.Line (picx - 8175 / datamax, y2)-(picx, picy_kxs), RGB(0, 255, 0) ' draw line

Picture1.Line (picx - 8175 / datamax, y3)-(picx, picy_yxyl), RGB(0, 0, 255) ' draw line

End If

End Sub

```

## 2. Program code of “set parameters” interface (Form2)

```
***** Define variables *****
```

```
Dim s2 As String, s3 As String, X(4) As Single, Y(4) As Single, k As Single, b As  
Single, c As Single, d As Single, e As Single, f As Single, n As Integer
```

```
***** Set default values command subroutine Command1 *****
```

```
Private Sub Command1_Click()
```

```
Text1.Text = 0.5
```

```
Text2.Text = 1.5
```

```
Text3.Text = 5
```

```
Text4.Text = 1
```

```
Text5.Text = 100
```

```
Text6.Text = 5
```

```
Text7.Text = 4.5
```

```
Text8.Text = 4
```

```
Text9.Text = 3.5
```

```
Text10.Text = 2.892
```

```
exp_scheme = "b"
```

```
fitting_k = -1
```

```
fitting_b = 5
```

```
End Sub
```

```
***** Get fourth calibrating data command subroutine Command10*****
```

```
Private Sub Command10_Click()
```

```
GetVol4:
```

```
s2 = Trim(Form1.MSComm1.Input)
```

```
If Len(s2) > 0 And Mid(s2, 5, 1) <> "" And Mid(s2, 1, 1) = "K" Then
```

```
    s3 = Mid(s2, 2, 4)                'read data
```

```
Else
```

```
    GoTo GetVol4
```

```
End If
```

```
Text9.Text = Format(Val((Val(Trim(s3)) / 1024 * 5) / (Val(Trim(Text4.Text)) *
```

```
Val(Trim(Text3.Text))), "###0.0000")
```

```
End Sub
```

```
***** Get fifth calibrating data command subroutine Command11*****
```

```
Private Sub Command11_Click()
```

GetVol5:

s2 = Trim(Form1.MSComm1.Input)

If Len(s2) > 0 And Mid(s2, 5, 1) <> "" And Mid(s2, 1, 1) = "K" Then

    s3 = Mid(s2, 2, 4)

    Else

    GoTo GetVol5

End If

Text10.Text = Format(Val((Val(Trim(s3)) / 1024 \* 5) / (Val(Trim(Text4.Text))) \*

Val(Trim(Text3.Text))), "###0.0000")

End Sub

\*\*\*\*\* Reset parameters command subroutine Command2\*\*\*\*\*

Private Sub Command2\_Click()

Text1.Text = ""

Text2.Text = ""

Text3.Text = ""

Text4.Text = ""

Text5.Text = ""

Text6.Text = ""

```
Text7.Text = ""
```

```
Text8.Text = ""
```

```
Text9.Text = ""
```

```
Text10.Text = ""
```

```
GetVol:
```

```
s2 = Trim(Form1.MSComm1.Input)
```

```
If Len(s2) > 0 And Mid(s2, 5, 1) <> "" And Mid(s2, 1, 1) = "K" Then
```

```
    s3 = Mid(s2, 2, 4)           'get reference voltage
```

```
Else
```

```
    GoTo GetVol
```

```
End If
```

```
Text4.Text = Format(Val(s3) / 1024 * 5, "###0.0000")
```

```
End Sub
```

```
***** Set and complete parameters command subroutine Command3*****
```

```
Private Sub Command3_Click()
```

```
Form1.current_low = Val(Trim(Text1.Text))
```

```
Form1.current_up = Val(Trim(Text2.Text))
```

```
Form1.intensity_ref = Val(Trim(Text3.Text))
```

```

Form1.voltage_ref = Val(Trim(Text4.Text))

Form1.datamax = Val(Trim(Text5.Text))

If exp_scheme = "b" Then          'select experimental scheme

    X(0) = Val(Text6.Text)

    X(1) = Val(Text7.Text)

    X(2) = Val(Text8.Text)

    X(3) = Val(Text9.Text)

    X(4) = Val(Text10.Text)

ElseIf exp_scheme = "r" Then

    X(0) = 2 * Arccos(Sqr(Val(Text6.Text) / Form1.intensity_ref))

    X(1) = 2 * Arccos(Sqr(Val(Text7.Text) / Form1.intensity_ref))

    X(2) = 2 * Arccos(Sqr(Val(Text8.Text) / Form1.intensity_ref))

    X(3) = 2 * Arccos(Sqr(Val(Text8.Text) / Form1.intensity_ref))

    X(4) = 2 * Arccos(Sqr(Val(Text9.Text) / Form1.intensity_ref))

End If

Y(0) = 0: Y(1) = 0.5: Y(2) = 1: Y(3) = 1.5: Y(4) = 2.108

For n = 0 To 4                    'Linear fitting

    c = X(n) + c

```

d = X(n) \* X(n) + d

e = X(n) \* Y(n) + e

f = Y(n) + f

Next

fitting\_b = (e \* c - f \* d) / (c \* c - 5 \* d)

fitting\_k = (c \* f - 5 \* e) / (c \* c - 5 \* d)

c = 0: d = 0: e = 0: f = 0

Form2.Hide            'Hide Form2

Form1.Show            'Show Form1

End Sub

"""""""""" Cancel setting parameters command subroutine Command4""""""""""

Private Sub Command4\_Click()

Form2.Hide

Form1.Show

End Sub

"""""""""" Select basic scheme command subroutine Command5""""""""""

```
Private Sub Command5_Click()
```

```
exp_scheme = "b"
```

```
End Sub
```

```
"""""""""" Select reflective scheme command subroutine Command5""""""""""
```

```
Private Sub Command6_Click()
```

```
exp_scheme = "r"
```

```
End Sub
```

```
"""""""""" Get first calibrating data command subroutine Command7""""""""""
```

```
Private Sub Command7_Click()
```

```
GetVol1:
```

```
s2 = Trim(Form1.MSComm1.Input)
```

```
If Len(s2) > 0 And Mid(s2, 5, 1) <> "" And Mid(s2, 1, 1) = "K" Then
```

```
    s3 = Mid(s2, 2, 4)
```

```
Else
```

```
    GoTo GetVol1
```

```
End If
```

```
Text6.Text = Format(Val((Val(Trim(s3)) / 1024 * 5) / (Val(Trim(Text4.Text))) *  
Val(Trim(Text3.Text))), "###0.0000")
```

```
End Sub
```

```
***** Get second calibrating data command subroutine Command8*****
```

```
Private Sub Command8_Click()
```

```
GetVol2:
```

```
s2 = Trim(Form1.MSComm1.Input)
```

```
If Len(s2) > 0 And Mid(s2, 5, 1) <> "" And Mid(s2, 1, 1) = "K" Then
```

```
    s3 = Mid(s2, 2, 4)
```

```
Else
```

```
    GoTo GetVol2
```

```
End If
```

```
Text7.Text = Format(Val((Val(Trim(s3)) / 1024 * 5) / (Val(Trim(Text4.Text))) *  
Val(Trim(Text3.Text))), "###0.0000")
```

```
End Sub
```

```
***** Get third calibrating data command subroutine Command9*****
```

```
Private Sub Command9_Click()
```

GetVol3:

s2 = Trim(Form1.MSComm1.Input)

If Len(s2) > 0 And Mid(s2, 5, 1) <> "" And Mid(s2, 1, 1) = "K" Then

    s3 = Mid(s2, 2, 4)

    Else

    GoTo GetVol3

End If

Text8.Text = Format(Val((Val(Trim(s3)) / 1024 \* 5) / (Val(Trim(Text4.Text))) \*

Val(Trim(Text3.Text))), "###0.0000")

End Sub

"""""""""" Load form subroutine """"""""""

Private Sub Form\_Load()

End Sub

### 3. Public module

"""""""""" Define public function to transfer fitted sensing curves""""""""""

Public fitting\_k As Single, fitting\_b As Single, exp\_scheme As String

Public Function Arccos(ByVal X As Double) As Double

If X = 1 Then

Arccos = 0

ElseIf X < 1 And X > -1 Then

Arccos = Atn(-X / Sqr(-X \* X + 1)) + 2 \* Atn(1)

Else

X = 1 / X

Arccos = Atn(-X / Sqr(-X \* X + 1)) + 2 \* Atn(1)

End If

End Function

## Appendix B Controlling program of low machine unit machine

The following text is the controlling program of the microprocessor based on  
CVAVR1.25.9.

/\*\*\*\*\*\*Project claim\*\*\*\*\*

Project : Fiber Optic Current Sensor and Its Wireless Sensing System

Version :

Date : 2013-6-20

Author : Chuantai Shi and Qiying Chen

Company : Memorial University of Newfoundland

Comments:

Chip type: ATmega16

Program type: Application

Clock frequency: 4.096000 MHz

Memory model: Small

External SRAM size: 0

Data Stack size: 256

\*\*\*\*\*/

```

/*****Define head file*****/

#include <mega16.h> //include the head file of the microprocessor

#include <delay.h> // include the head file of delay function

#include <stdio.h> // include the head file of input and output

#include <lcd.h> // include the head file of LCD

/*****Define global variables*****/

unsigned char DC[10]={'0','1','2','3','4','5','6','7','8','9'};

unsigned int adc_data;

/***** Initialize settings of LCD and connection to Mega 16*****/

#asm

.equ __lcd_port=0x15 ;PORTC

#endasm

/*****CVAVR process defines USART constants*****/

#define RXB8 1

#define TXB8 0

#define UPE 2

#define OVR 3

```

```

#define FE 4

#define UDRE 5

#define RXC 7

#define FRAMING_ERROR (1<<FE)

#define PARITY_ERROR (1<<UPE)

#define DATA_OVERRUN (1<<OVR)

#define DATA_REGISTER_EMPTY (1<<UDRE)

#define RX_COMPLETE (1<<RXC)

/*****USART sending buffer definition*****/

#define TX_BUFFER_SIZE 8           // set sending buffer 8 bytes and initialize

char tx_buffer[TX_BUFFER_SIZE];

#if TX_BUFFER_SIZE<256

unsigned char tx_wr_index,tx_rd_index,tx_counter;

#else

unsigned int tx_wr_index,tx_rd_index,tx_counter;

#endif

```

```

/*****USART sending interruption subroutine*****/

interrupt [USART_TXC] void usart_tx_isr(void)    //usart sending input

{

if (tx_counter)

{

--tx_counter;

UDR=tx_buffer[tx_rd_index];

if (++tx_rd_index == TX_BUFFER_SIZE) tx_rd_index=0;

};

}

```

```

/*****write a byte to sending buffer subroutine*****/

#ifndef _DEBUG_TERMINAL_IO_

#define _ALTERNATE_PUTCHAR_

#pragma used+

void putchar(char c)    //write a byte

{

while (tx_counter == TX_BUFFER_SIZE); //wait if there is no data

asm("cli")    //close interruption

```

```

if (tx_counter || ((UCSRA & DATA_REGISTER_EMPTY)==0)) {

    tx_buffer[tx_wr_index]=c; // add a byte

    if (++tx_wr_index == TX_BUFFER_SIZE) tx_wr_index=0; // if data is full pointer
clears

    ++tx_counter;

}

else

    UDR=c;

    #asm("sei")                //open interruption

};

#pragma used-

#endif

/*****ADC converter subroutine *****/

#define ADC_VREF_TYPE 0x40 // define reference voltage

interrupt [ADC_INT] void adc_isr(void)//ADC interruption

{

// Read the AD conversion result

adc_data=ADCW;                // read ADC result

```

```

};

unsigned int read_adc(unsigned char adc_input)    // get rid of noise

{

    ADMUX=adc_input | (ADC_VREF_TYPE & 0xff);    // set AVcc reference
voltage

    // Delay needed for the stabilization of the ADC input voltage

    delay_us(10);                                // delay to wait for stable input voltage

    #asm

        in  r30,mcucr

        cbr r30,__sm_mask

        sbr r30,__se_bit | __sm_adc_noise_red

        out mcucr,r30

        sleep

        cbr r30,__se_bit

        out mcucr,r30

    #endasm

    return adc_data;                             // return result after removing noise

};

```

```
/****** LCD display subroutine******/
```

```
void zyl_lcd(unsigned int D3,unsigned int D2,unsigned int D1,unsigned int D0)
```

```
{
```

```
    lcd_clear();          //LCD clears
```

```
    lcd_putsf("ZYL--KXS Press:");
```

```
    delay_ms(10);
```

```
    lcd_gotoxy(0,1);
```

```
    lcd_putchar(DC[D3]);
```

```
    lcd_gotoxy(1,1);
```

```
    lcd_putchar(DC[D2]);
```

```
    lcd_gotoxy(2,1);
```

```
    lcd_putchar(DC[D1]);
```

```
    lcd_gotoxy(3,1);
```

```
    lcd_putchar(DC[D0]);
```

```
    lcd_gotoxy(4,1);
```

```
    lcd_putsf("V");
```

```
    delay_ms(30);
```

```
};
```

```
/****** LCD Initialization display******/
```

```
void system_init()
```

```
{
```

```
    lcd_clear();
```

```
    lcd_putsf("Hello Everyone!");
```

```
    delay_ms(100);
```

```
    lcd_gotoxy(0,1);
```

```
    lcd_putsf("System initing.");
```

```
    delay_ms(1500);
```

```
    lcd_clear();
```

```
    lcd_gotoxy(2,0);
```

```
    lcd_putsf("FOCS");
```

```
    delay_ms(100);
```

```
    lcd_gotoxy(5,1);
```

```
    lcd_putsf("System");
```

```
    delay_ms(1500);
```

```
    lcd_clear();
```

```
    lcd_putsf("By SHICHUANTAI");
```

```
    delay_ms(100);
```

```
    lcd_gotoxy(0,1);

    lcd_putsf("MUN");

    delay_ms(1500);

    lcd_clear();

}
```

```
/******Main process******/
```

```
void main(void)
```

```
{
```

```
//Define variables
```

```
unsigned int DA=0,D0=0,D1=0,D2=0,D3=0;
```

```
unsigned char p;
```

```
PORTA=0x03;    // PA port initializes
```

```
DDRA=0x00;    // define input PA.0、 PA.2
```

```
PORTC=0x00;    // PC port initializes
```

```
DDRC=0xFF;    // set PC port as output to drive LCD
```

```

// USART initializes 8N1, 9600

UCSRA=0x00;

UCSRB=0x48;

UCSRC=0x86;

UBRRH=0x00;

UBRRL=0x1A;

ADMUX=ADC_VREF_TYPE & 0xff; //set AVcc reference

ADCSRA=0x8D; // enable ADC

lcd_init(16); //LCD initialize

system_init();

asm("sei") // open global interruption service

while (1)
{

p=0x00; //choose ADC port

DA=read_adc(p); //read ADC result

```

```

{D3=DA/1000;DA=DA%1000;D2=DA/100;DA=DA%100;D1=DA/10;DA=DA%10;D0
=DA;}

    // process ADC result

    zyl_lcd(D3,D2,D1,D0);

{putchar('Z');putchar(DC[D3]);putchar(DC[D2]);putchar(DC[D1]);putchar(DC[D0]);}

    delay_ms(30);

    p=0x01;

    DA=read_adc(p);

    {D3=DA/1000;DA=DA%1000;D2=DA/100;DA=DA%100;D1=DA/10;DA=DA%1
0;D0=DA;}

    kxs_lcd(D3,D2,D1,D0);

{putchar('K');putchar(DC[D3]);putchar(DC[D2]);putchar(DC[D1]);putchar(DC[D0]);} //
send ADC result to buffer

    delay_ms(460);

    };

}

```





